Gamma-ray Spectroscopy of Superdeformed Bands in ^{150}Gd and ^{151}Gd

Thesis submitted in accordance with the requirements of the
University of Liverpool for the degree of Doctor in Philosophy

by

Sefa ERTÜRK

Oliver Lodge Laboratory
June 1998

TO MY MOTHER, BROTHER AND SISTERS.

AND TO THE MEMORY OF MY FATHER
WHO WILL NEVER BE FORGOTTEN.

THIS THESIS IS DEDICATED TO THEM.

Acknowledgements

This present research is the product not only of the writer's interest in this area of specialisation but also the result of the ongoing help received from various people who have been most generous with their time and patience.

It would be difficult to mention all their names, but I would like to take this opportunity to thank those who have perhaps contributed in no small degree to the successful completion of the present work.

To the nuclear structure group (both past and present) for their enthusiasm and assistance over the years, and particularly to Dr. Duncan Appelbe, to Roger Allat, to Kevin Cann, and Dr. David Joss, four fellow finalists in this great postgraduate marathon.

To Prof. P.J Twin, for allowing me the opportunity to undertake research in the Department of Physics at the University of Liverpool.

To Dr. P.J Nolan, for his administrative help in the latter stage of my study.

To Dr. D. Appelbe, for his willingness to give invaluable help and advice whenever he was asked to, as well as for his readiness to do proof-reading in the stages of this preparation.

To Dr. D. Cullen, for his attentiveness in reading the first three chapters at precisely the right moment.

To Dr. D. Joss, for offering his assistance in the proof-reading of content and subject-matter.

To Stephen King, for offering his assistance in the proof-reading of the last three chapters.

To the computer staff, namely Dr. J. Cresswell. Ms. J. Sampson and recently to Dr. I. Hibbert for their help and continued assistance.

To Dr. M. Smith, for allowing me invaluable access to some of his figures as a basis for my own theory chapter.

To Dr. E. Paul, for his continued availability whenever he was required for urgent consultation on any number of matters.

To Dr. C. Beausang, I feel a particular debt of gratitude for being there at the most crucial times and for offering me his invaluable advice and expertise when he obviously had many more things of greater importance that demanded his immediate attention.

To Dr. Lewis Hall, a special vote of thanks for his unsparing time and patience in dealing with the more difficult aspects of English language.

To Dr. Ibrahim Tuğlu, to Atila Akça, to Ibrahim Demirkan and Maggie Mulgrew for their continuing moral support.

My sincerest thanks go to the Turkish government for their financial support in enabling me to pursue this course of study.

My final debt of gratitude is owing to my family, who have demonstrated great patience and fortitude during my prolonged absence from home.

Abstract

High-spin states have been studied in ^{150,151}Gd using the heavy-ion fusion evaporation reaction ^{130}Te(^{26}Mg, 6n)^{156}Gd at a beam energy of 149 MeV. The resultant γ-rays were detected using the GAMMASPHERE γ-ray spectrometer based at LBL, Berkeley. Twenty rotational bands have been observed in these data: six of them were previously known in ^{150}Gd, eight have been assigned to the nucleus ^{150}Gd while the remaining six have been assigned to the nucleus ^{151}Gd. Prior to this experiment being performed, no evidence of superdeformed (SD) structures was known in ^{151}Gd.

The previously-observed SD bands 1, 2 and 4a in ^{150}Gd have been extended to higher rotational frequencies. The two lowest transitions of band 4b have been found not to be in coincidence with the remaining members of this band. Band 5 in ^{150}Gd has been extended to both lower and higher rotational frequencies, indicating a backbend at the highest rotational frequencies. In addition, band 10a and 10b showed discontinuity at lower frequencies.

Details of the decay scheme around the backbend for band 2 have been established. Additionally, a series of seven transitions has been observed linking the yrast SD band and band 2, which have been identified as electric quadrupole (E2) transitions with a value of B(E2) $\approx$ 30 W.u. This is the first observation of linking transitions between SD bands in the mass 150 region. Furthermore, previously-predicted cross-band transitions between bands 3 and 4a have been identified and the interaction strength of interacting orbits has been deduced to be $|V| = 11 \pm 1$ keV, in good agreement with previous data.

On the basis on the discovery of six SD bands in ^{151}Gd and eight new SD bands in ^{150}Gd , it was suggested that there are more missing bands in these nuclei. In future experiments, an investigation to search for these missing bands would provide important information about the properties of high-N intruder orbitals in the mass 150 region.

Contents

Introduction

The work described in this thesis is concerned with high-spin nuclear physics: namely, superdeformation. The main mass regions that exhibit superdeformation lie around $A \approx 80$, 130, 150, 190 and a newly-discovered superdeformed mass region associated with $A \approx 60$ nuclei. However, this thesis describes the superdeformed nature of ^{150}Gd and ^{151}Gd.

A study has been made of these nuclei and each chapter is reviewed respectively as follows:

1. A brief review of nuclear properties and the theoretical models are given. Following the introduction of the Shell Model, the different nuclear potentials are discussed within the framework of both spherical and deformed nuclear shapes. Nuclear rotation is described in terms of single-particle and collective rotation. Finally, the Cranked Shell Model, pairing correlations and the Strutinsky Shell correction procedure are introduced.

2. The experimental techniques and the analysis methods employed throughout the course of this work are discussed along with the method used for populating high-spin nuclear states. This chapter is concluded with a description of the GAMMASPHERE γ-ray spectrometer.

3. This chapter introduces superdeformation in the $A \approx 150$ mass region and explains the properties of superdeformed bands. Previous studies of ^{150}Gd and ^{151}Gd are discussed followed by the motivations behind this study and concluding with experimental details.

4. The results obtained from this experiment are presented and discussed for the nucleus ^{150}Gd by introducing the new superdeformed bands in this nuclei with an explanation behind the assigned nuclear configurations. This is followed by details of the observed linking transitions between bands 1 and 2, and between bands 3 and 4a.

5. The first observation of superdeformed bands in ^{151}Gd is presented by giving the results obtained from the experiment. These results are discussed in the same manner as the previous chapter.

6. General conclusions and future investigative research are presented in this chapter.

Some of the results presented in this thesis have been reported by Twin *et al.*, [Tw96] and Beausang *et al.*, [Bea98].

Chapter 1

Nuclear Properties and Models

1.1 Nuclear Properties

The most fundamental properties of the nucleus are its mass and spin. The former can be measured using a mass spectrometer [He94]. Such measurements were first performed in the early thirties. From these measurements it was concluded that the binding energy per nucleon was almost invariably constant for all nuclei [Je90], suggesting a constant distribution of nuclear matter within the nucleus.

Electron [Eh59] and Rutherford [Ch73] scattering experiments, along with the measurements of nuclear matter distributions, have shown that the number of nucleons per unit volume is roughly constant i.e :

$$\frac{A}{4\pi R^3} \approx \text{constant} \tag{1.1}$$

where A is the mass number and R is the mean radius of the nucleus given by

$$R = r_0 A^{1/3} \tag{1.2}$$

where r_0 is a constant. From these scattering measurements it was concluded that $r_0 \approx 1.2$ fm (1 fm $= 10^{-15}$ m) for the charge radius while $r_0 \approx 1.4$ fm for the matter radius [He94]. The nuclear volume is proportional to the number of nucleons, and, as a result, the density of the nucleus remains constant for all nuclei [Tu79]. The density of nuclear matter is given by:

$$\begin{aligned} \rho &= \frac{\text{NuclearMass}}{\text{NuclearVolume}}, \\ &= \frac{A}{\frac{4}{3}\pi R^3} = constant. \end{aligned}$$

The properties of the nucleus can be characterised in a way similar to those of a liquid drop, where the interaction between molecules consists of a short-range attractive force coupled with a repulsive core [Je90]. Although the liquid drop model has proved to be very useful, particularly in the description of the fission of heavy nuclei, it does not give any information on the excitation energy of the nucleus or the quantum properties of nuclear states.

A semi-empirical approach for determining the nuclear mass was first proposed by Weizsäcker in 1935 [We35]. One year later, Bethe and Bacher simplified Weizsäcker's formula. The Bethe-Weizsäcker semi-empirical mass formula is stated as:

$$M(A,Z) = Zm_p + (A-Z)m_n - B(N,Z), \tag{1.3}$$

where m_p and m_n are the rest mass of protons and neutrons respectively and $B(N,Z)$ is the binding energy of the nucleus given by:

$$B(N,Z) = a_v A - a_s A^{2/3} - a_c \frac{Z^2}{A^{1/3}} - a_a \frac{(N-Z)^2}{A} + \delta(A). \tag{1.4}$$

Each term in the equation (1.4) provides a different contribution to the nuclear binding energy; these individual effects are shown in Figure 1.1.

The principal contribution to binding energy arises from the volume term ($a_v A$); other contributions are the surface term ($a_s A^{2/3}$), the Coulomb term ($a_c \frac{Z^2}{A^{1/3}}$), the symmetry term ($a_a \frac{(N-Z)^2}{A}$), and the pairing term ($\delta(A)$). This accounts for the fact that the most stable nuclei have even numbers of protons and neutrons. The semi-empirical mass formula successfully describes the general smooth variation of binding

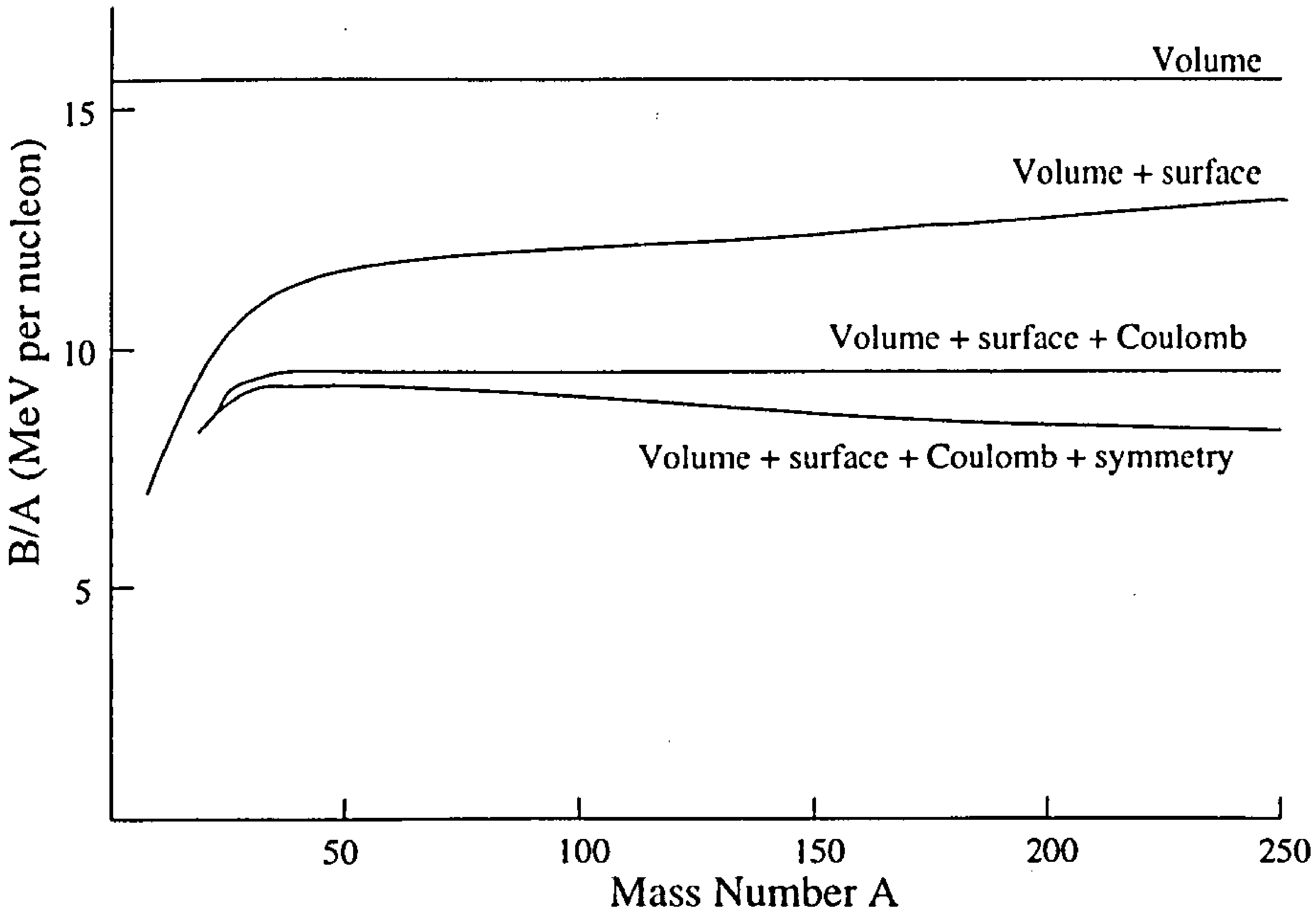

Figure 1.1: The contribution of various terms in the semi-empirical mass formula to the binding energy per nucleon. Adapted from citeKr88.

energy for most nuclei [Tu79]. However, discontinuities arise due to quantum shell structure.

1.2 The Shell Model

The collective liquid drop model does not account for microscopic effects. The shell model has provided remarkable clarification of the complicated details of atomic structure; therefore, nuclear physicists have attempted to use this model to characterise the structure of the nucleus. There is some experimental evidence to support the fact that this model appears to have a connection with the observed variations; for example, the nuclear radius and the low neutron cross-sections imply that a neutron-capture take place to deplete their numbers. However, the experimentally-observed features showed that the sudden and discontinuous behaviour occurs at the same proton or neutron numbers of N or Z = 2, 8, 20, 28, 50, 82 and 126 for stable nuclei [Kr88]. These are known as "magic" numbers.

The existence of this shell structure illustrates the need for a more detailed description of the nucleus in terms of the shell model. This model has had considerable success in explaining the shell gaps and describing the spin and parity of nuclei [VH73].

The development of a shell model is non-trivial due to the complex form of the nuclear potential. In the nucleus, each nucleon moves in a central potential, $V(r)$, which arises from the average interaction of each nucleon with all other nucleons. The shell model Hamiltonian H for the nucleus is composed of this average potential, $V(r)$ plus the sum of the individual kinetic energies of all the independent nucleons, T:

$$T = \sum_{i=1}^{A} \frac{+{p_i}^2}{2m_i} = \sum_{i=1}^{A} \frac{-\hbar^2}{2m_i}\nabla^2 \tag{1.5}$$

where m_i and p_i represent the nucleon mass and the momentum of the ith nucleon respectively. Accordingly, the nuclear Hamiltonian can be written as:

$$H = T + V(r) = \sum_{i=1}^{A} \frac{-\hbar^2}{2m_i}\nabla^2 + V(r) \tag{1.6}$$

where the second term describes the mean field potential. This mean field approximation is a good start for the development of a successful nuclear model.

1.2.1 The Harmonic Oscillator Potential

Early attempts to describe nuclear potentials were based on a simple square-well model. However, these approaches were superseded by a harmonic oscillator (HO), a useful starting point to describe the nuclear potential since it provides a first approximation of the nuclear potential, which is analytically soluble.

The HO potential (Figure 1.2) is described by:

$$V_{HO}(r) = \frac{1}{2}m\omega_0^2(r^2 - R^2), \tag{1.7}$$

where R is the nuclear radius, V(r) = 0 for r > R and ω_0 is the oscillator frequency.

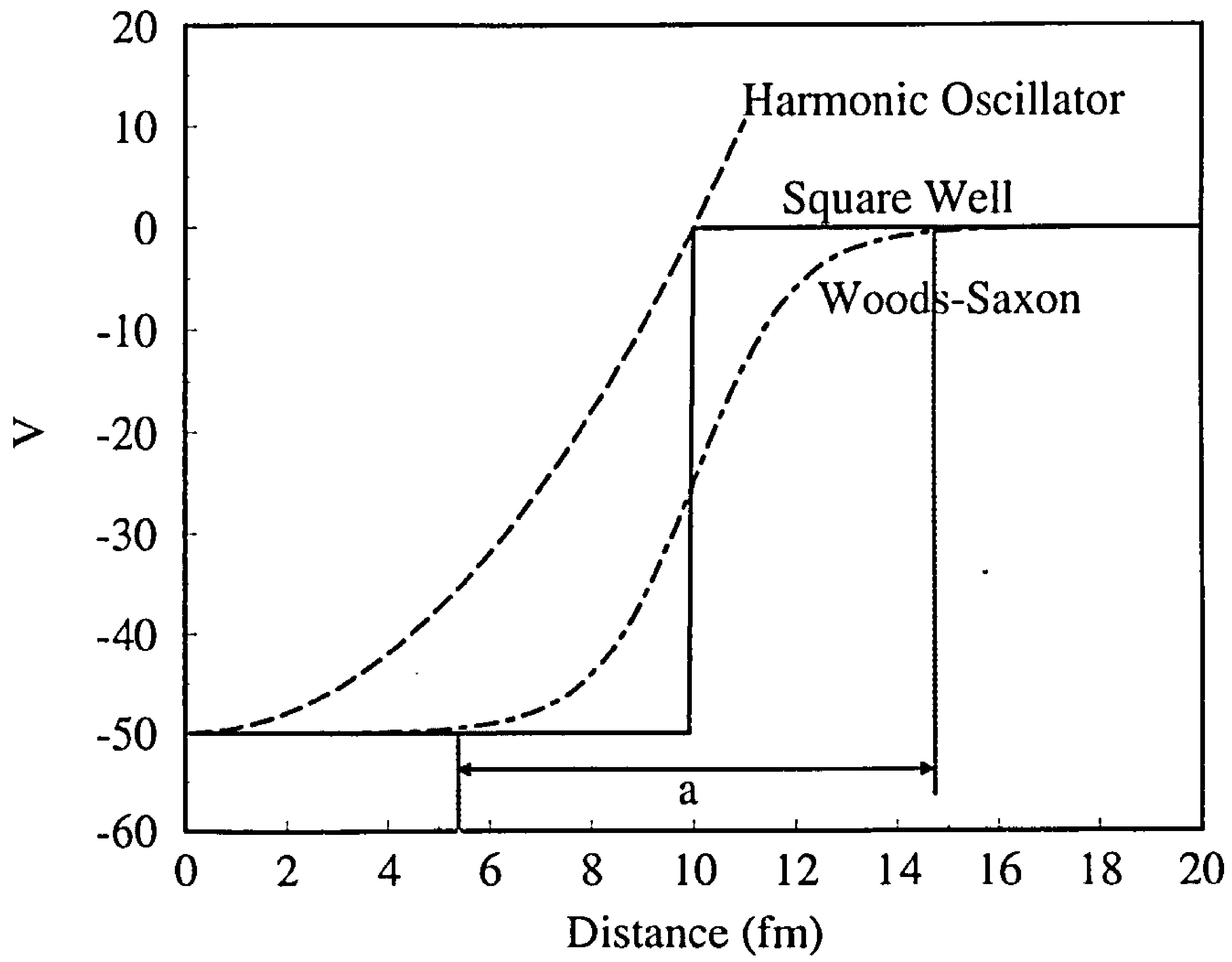

Figure 1.2: A schematic comparison of Harmonic Oscillator potential with the Woods-Saxon potential and Square Well potential.

The eigenvalues of the Hamiltonian are represented by:

$$E = \hbar\omega_0 \left(N + \frac{3}{2}\right) \tag{1.8}$$

where N is the principal quantum number, defined as:

$$N = 2n + l \tag{1.9}$$

Here, n is the radial quantum number, (n = 1, 2, ...) and l is the orbital angular momentum quantum number (l = 0, 1, 2, ...). The energy levels of the HO Hamiltonian can be labelled as Nl (l = 0, 1, 2, ... are labelled as s, p, d, ...). The levels comprising the same N are called an oscillator shell and are $D(N)$ fold degenerate

$$D(N) = \frac{1}{2}(N+1)(N+2). \tag{1.10}$$

The HO potential produces equally-spaced energy levels, which are shown on the left-hand side of Figure 1.3, where they are labelled by the quantum number N. Levels that arise from the same oscillator shell have the same parity, given by:

$$\pi = (-1)^N. \tag{1.11}$$

Therefore, shells with even N have positive parity and those with odd N have negative parity. However, this description of HO only reproduces the experimentally-observed magic numbers 2, 8, 20. For heavier nuclei, the shape of the simple HO potential is incorrect. Nevertheless, the HO potential can be further modified by adding the l^2 term, which makes the shape of the nuclear potential more realistic. This effect is shown in the middle portion of Figure 1.3. However, the observed magic numbers are still not correctly produced, even with the addition of the l^2 term.

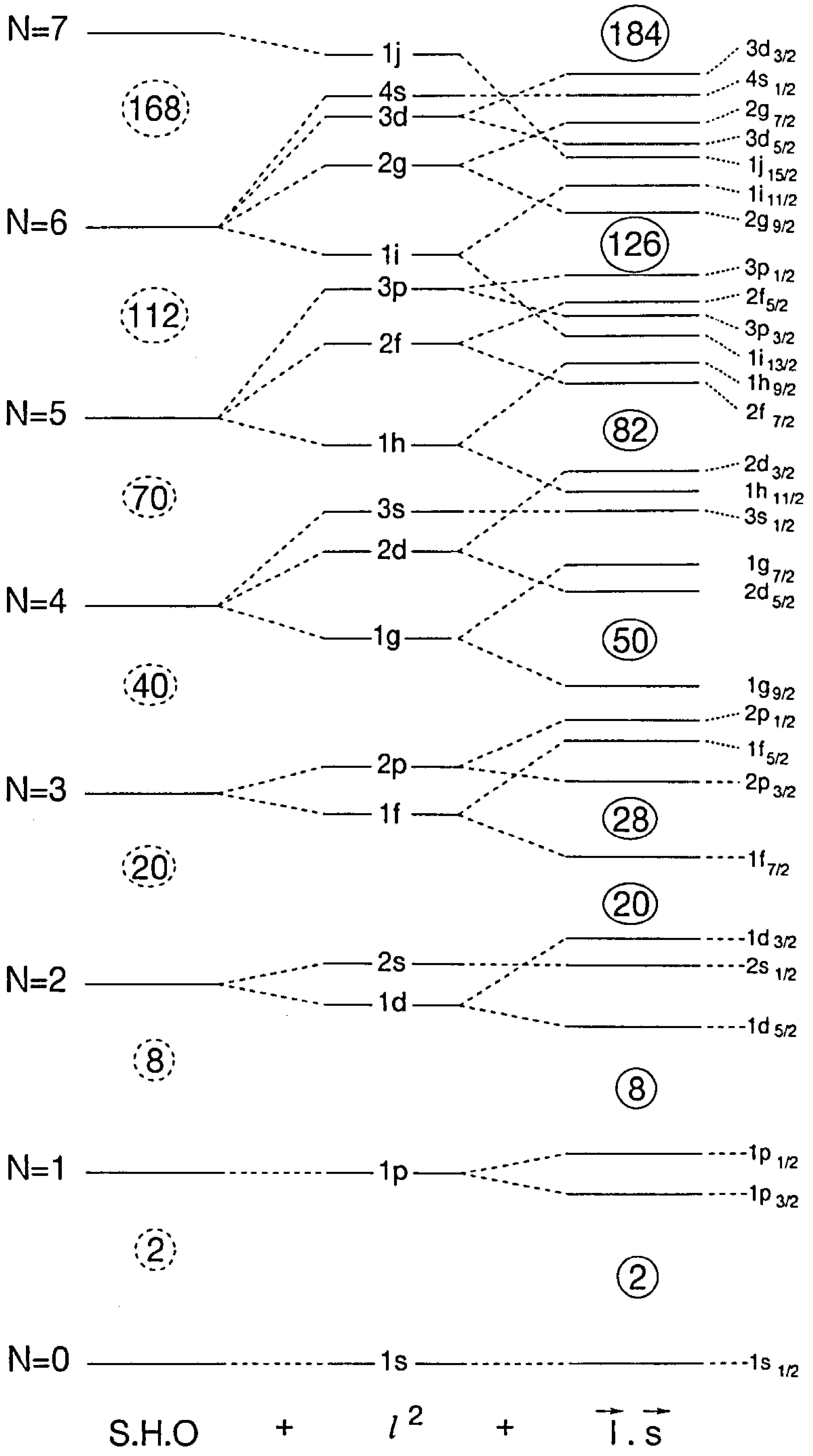

Figure 1.3: Single-particle energies for a simple harmonic oscillator (S.H.O), a modified harmonic oscillator with l^2 term, and a realistic shell model potential with l^2 and spin orbit ($\underline{l} \cdot \underline{s}$) terms.

1.2.2 The Woods-Saxon Potential

Providing a good approximation to the nuclear mean-field, the Woods-Saxon (WS) potential [WS54] has a form which derives from experimental observations. It has, therefore, advantages over the HO, such as classification of a finite well-depth. The WS potential is often used in nuclear structure studies and has the form;

$$V_{WS}(r) = \frac{-V_0}{1 + \exp(\frac{r-R_0}{a})} \tag{1.12}$$

where V_0 is the depth of the potential (approximately 50 MeV), R_0 is the nuclear radius, and a is a term added to describe the surface diffuseness of the nucleus which does not have a sharply-defined boundary (see Figure 1.2). With this potential the nuclear Hamiltonian becomes:

$$H_{WS} = \frac{-\hbar^2}{2m}\nabla^2 + \frac{-V_0}{1 + \exp(\frac{r-R_0}{a})} \tag{1.13}$$

The energy levels resulting from the potential in this form are similar to those shown in the central section of Figure 1.3. Although the agreement with the experimentally-observed magic numbers is now improved, the WS potential still does not reproduce them well at high N, Z. However, with the addition of a spin-orbit term, this potential can reproduce all the magic numbers.

1.2.3 Spin-Orbit Coupling

The correct sub-shell separation numbers were obtained for heavier nuclei in 1949, with the addition of the spin-orbit term in the WS potential, by Mayer [Ma49] and Haxel, Jensen and Suess [HJS49]. This spin-dependent term is known as the spin-orbit coupling and is written as:

$$V_{SO} = -f(r)\underline{l} \cdot \underline{s} \tag{1.14}$$

where $\underline{l}$ represents the nucleon-orbital angular momentum quantum number and $\underline{s}$ represents the intrinsic spin angular momentum quantum number. The spin-orbit coupling removes the spherical degeneracy of the potential, and states can be labelled with their total angular momentum, $\underline{j} = \underline{l} + \underline{s}$. Nucleons have s = $\frac{1}{2}$; therefore, the total angular momentum has two components, $j = l \pm \frac{1}{2}$. The levels obtained with the inclusion of the spin-orbit term are shown on the right-hand side of Figure 1.3.

The nuclear Hamiltonian now becomes $H = T + V_{WS} + V_{SO}$:

$$H_{WS} = \frac{-\hbar^2}{2m}\nabla^2 + \frac{-V_0}{1+\exp(\frac{r-R_0}{a})} - f(r)\underline{l}\cdot\underline{s} \tag{1.15}$$

and it reproduces the experimentally-determined magic numbers.

As can be observed from Figure 1.3, states with high-j, ($j = l + \frac{1}{2}$), are lower in energy than those with low-j states, ($j = l - \frac{1}{2}$); therefore, a high-j orbital may be lowered in energy so that it intrudes on the next lowest shell. This orbital is then known as an "intruder" orbital. Such an orbital, therefore, has opposite parity to those states arising from the "natural" parity orbits.

1.2.4 Nuclear Deformation

The potentials described in previous sections are all spherically symmetric; therefore, a further modification is necessary in order to describe deformed nuclei. Nuclei in the mass region A ≈ 60, 80, 130, 150, 190 and A > 220 (actinides) are found to have substantial deviation from the spherical shape in their ground states.

The deformed nuclear surface can be described by the length of the radius vector pointing from the centre of the nucleus to its surface in spherical polar coordinates

$$R = R(\theta,\phi) = R_0\left[1 + \alpha_{00} + \sum_{\lambda=1}^{\infty}\sum_{\mu=-\lambda}^{\lambda}\alpha^*_{\lambda\mu}Y_{\lambda\mu}(\theta,\phi)\right], \tag{1.16}$$

where R_0 is the radius of the sphere of equal volume to the deformed nucleus, $Y_{\lambda\mu}(\theta,\phi)$ are the spherical harmonics, and $\alpha_{\lambda\mu}$ describes changes in nuclear volume with λ defining the deformation type; (($\lambda = 1$) dipole, ($\lambda = 2$) quadrupole, etc.), with μ as an integer which varies from -λ to +λ. For an axially symmetric nuclei with quadrupole deformation (where $\lambda = 2$ and $\alpha_{22} = \alpha_{2-2} = 0$), only the Y_{00} and Y_{20}

harmonics are involved and the surface equation reduces to

$$R(\theta) = R_0(1 + \alpha_{00}Y_{00} + \alpha_{20}Y_{20}) \tag{1.17}$$

$\alpha_{00}Y_{00}$ is a normalisation term which ensures that the nuclear volume is conserved. The coefficient of the Y_{20} term is defined as $\alpha_{20} = \beta_2$, where β_2 is the quadrupole deformation parameter and is defined as:

$$\beta_2 = \frac{4}{3}\sqrt{\frac{\pi}{5}}\frac{\Delta R}{R_0} \tag{1.18}$$

where ΔR is the difference between the major and minor axes of the ellipsoid. It is often more convenient to describe α_{20} and α_{22} in terms of the Hill-Wheeler coordinates β_2 and γ which is the triaxiality parameter [HW53]:

$$a_{20} = \beta_2 \cos\gamma \tag{1.19}$$

and

$$a_{22} = \frac{1}{\sqrt{2}}\beta_2 \sin\gamma \tag{1.20}$$

The new parameterisation of the nuclear shape in terms of β_2 and γ is given by;

$$R(\theta,\phi) = R_0\left[1 + \sqrt{\frac{5}{16\pi}}\beta_2((3\cos^2\theta - 1) + \sqrt{3}\sin\gamma\sin^2\theta\cos 2\phi)\right] \tag{1.21}$$

After the definition of the β_2 and γ coordinates, the various types of nuclear shapes are shown in Figure 1.4. According to the Lund convention [An76], axially-symmetric shapes occur at multiples of $\gamma = 60°$.

When the shell model needs to be extended to describe nuclei with non-spherical shapes, the potential in the nuclear Hamiltonian must be deformed. The more realistic deformed potentials are adapted from the HO and WS potentials and are described next in Section 1.2.5.

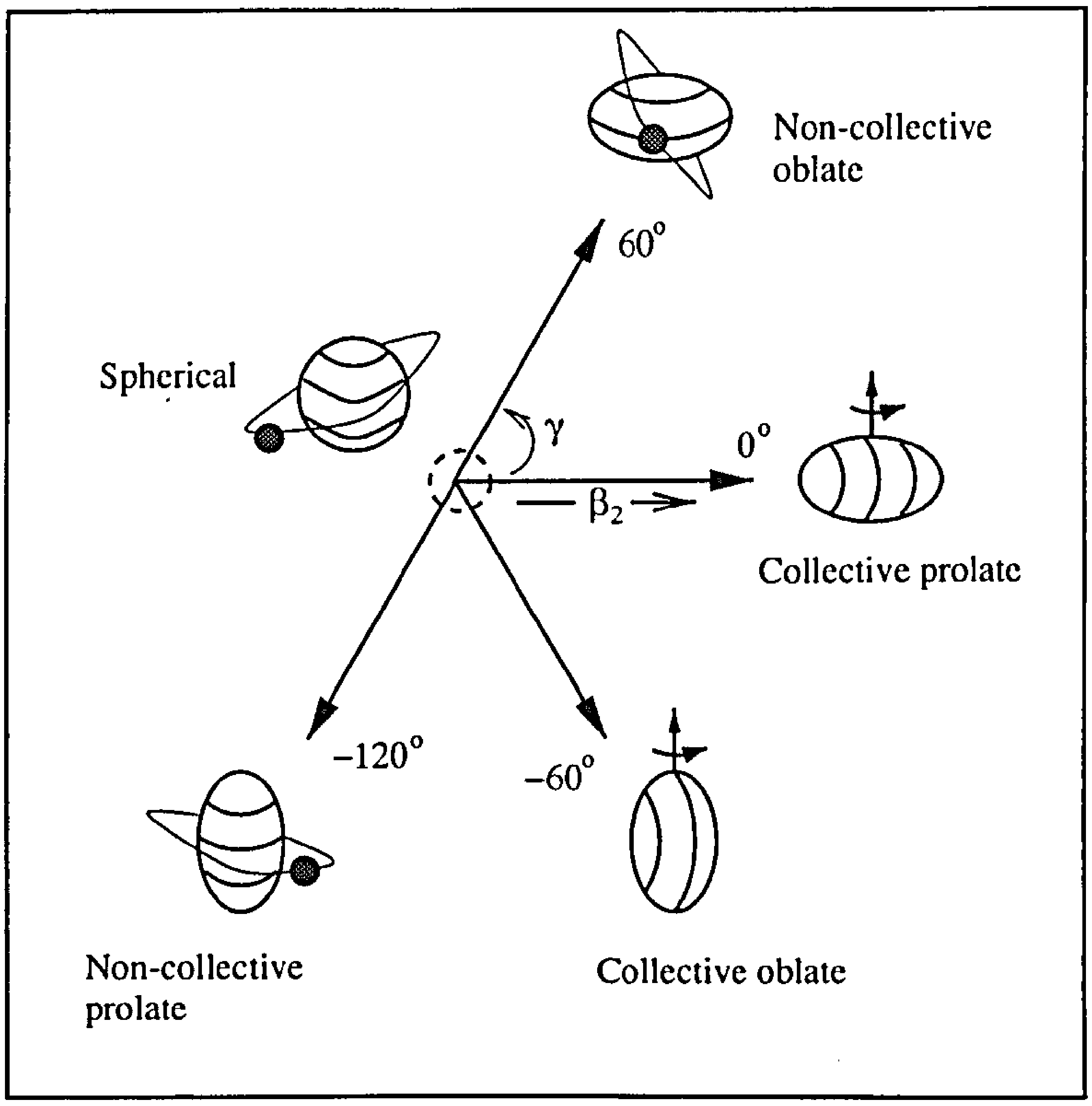

Figure 1.4: Parameterisation of quadrupole nuclear shape according to the Lund convention.

1.2.5 The Nilsson Potential

Nilsson suggested that two modifications had to be made to the standard HO potential in order to reproduce correctly the experimentally-observed "magic" numbers [Ni55]. He started from a spherical distribution using the Cartesian coordinate system to describe the shape of the nucleus. The total oscillation frequency, ω_0, can be written in terms of the Cartesian x, y and z components, as ω_x, ω_y and ω_z. Hence, the HO potential can be presented as:

$$V_{osc} = \frac{m}{2}({\omega_x}^2 x^2 + {\omega_y}^2 y^2 + {\omega_z}^2 z^2).$$

The deformed modified HO potential may be simplified by considering only axially-symmetric shapes such as:

$$\omega_\perp = \omega_x = \omega_y$$

and

$$V_{MHO} = \frac{m}{2}[\omega_\perp{}^2(x^2+y^2) + \omega_z^2 z^2] \tag{1.22}$$

where $\omega_\perp$ and ω_z are the oscillator frequencies perpendicular and parallel to the symmetry z-axis respectively.

Nilsson introduced the deformation parameter ϵ to allow a parameterisation of ω_x, ω_y, ω_z in terms of ω_0

$$\omega_\perp = \omega_0(\epsilon)\left(1 + \frac{1}{3}\epsilon\right) \tag{1.23}$$

and

$$\omega_z = \omega_0(\epsilon)\left(1 - \frac{2}{3}\epsilon\right) \tag{1.24}$$

where ϵ is the deformation parameter related to the β_2 by the formula

$$\epsilon = \frac{3}{2}\left(\frac{5}{4\pi}\right)\beta_2 \tag{1.25}$$

Finally, Nilsson added a spin-orbit term to reproduce the correct magic numbers. The Nilsson potential is defined as:

$$V_{Nil} = V_{MHO} - 2\kappa\hbar\omega_0\left[\underline{l}.\underline{s} - \mu(\underline{l}^2 - \langle \underline{l}^2\rangle_N)\right] \tag{1.26}$$

where $\underline{l}\cdot\underline{s}$ is the spin-orbit term in the stretched coordinate system and the $(\underline{l}^2 - \langle\ \underline{l}^2\ \rangle_N)$ term flattens the potential for the centre of nucleus. κ and μ are constants which define the strength of the spin-orbit interaction. These modifications reproduced the experimentally-observed "magic" numbers.

In the Nilsson model four quantum numbers are used to classify the orbitals.

$$[Nn_z\Lambda]\Omega^\pi \tag{1.27}$$

where N is the principal quantum number of oscillator quanta, n_z is the number of oscillator quanta along the z-axis, and Λ and Ω are the components of the orbital and total angular momentum along the symmetry z-axis. Their relationship can be seen in Figure 1.5. Finally, π is the parity of the state and is given by $\pi = (-1)^N$.

The projection of the orbital angular momentum $\underline{l}$, intrinsic spin $\underline{s}$ and total angular momentum $\underline{j}$ vectors on to the z-axis are Λ , Σ and Ω respectively in Figure 1.5. Their relationship can be summarised as:

$$\Omega = \Lambda \pm \Sigma \tag{1.28}$$

The projection of total coupled angular momentum $\underline{j}$ can also be defined in terms of the K quantum number:

$$K = \sum_{i=1} \Omega_i$$

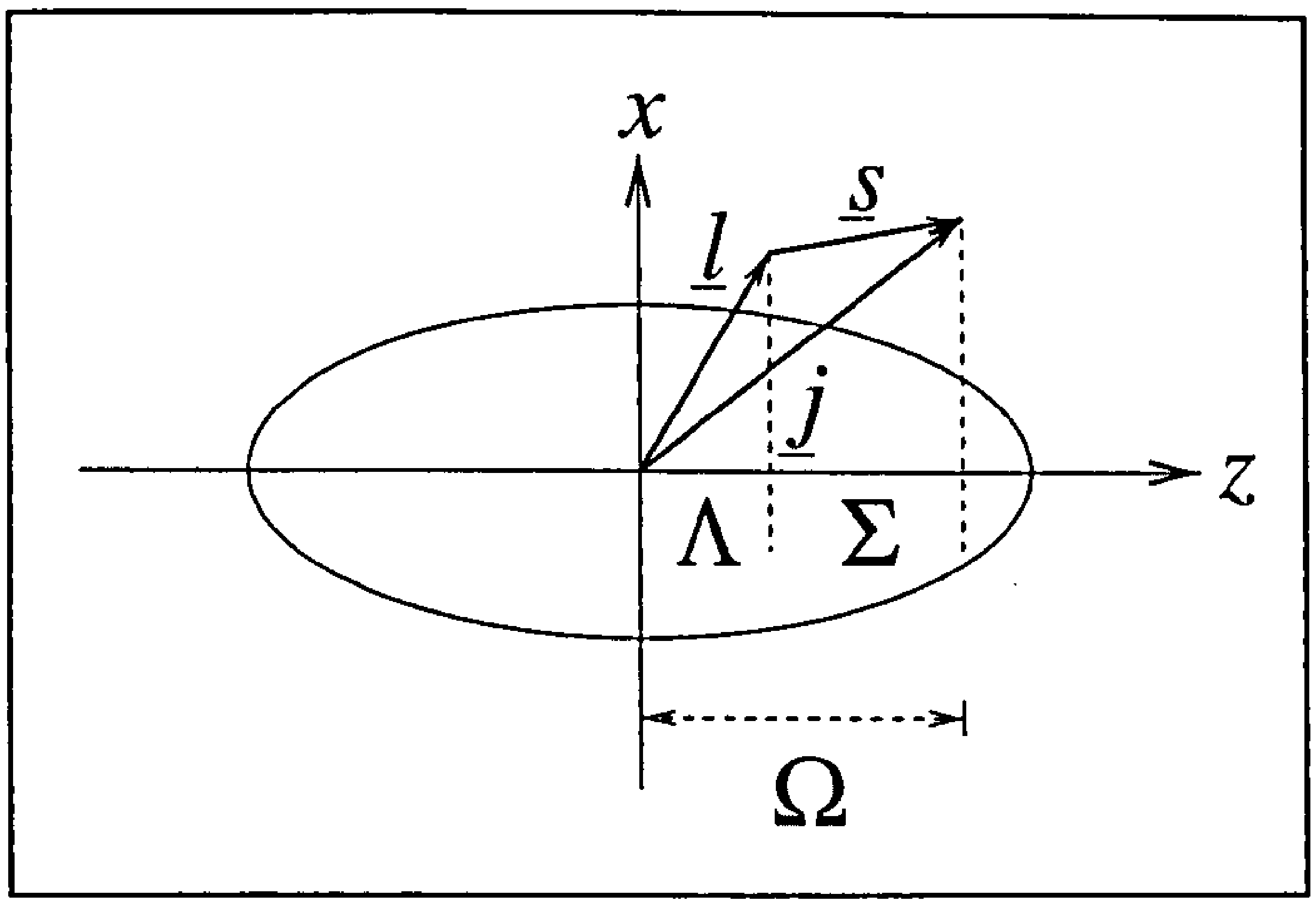

Figure 1.5: A schematic diagram of a deformed nucleus showing the projection of the orbital ($\underline{l}$), intrinsic ($\underline{s}$) and total angular momenta ($\underline{j}$) on to symmetry axis z.

Figure 1.6 shows a schematic of the Nilsson energy levels for the neutron of nuclei in the region $50 \leq N \leq 82$. The spherical shell model magic numbers are reproduced at $\beta_2 = 0$ in regions of low-level density.

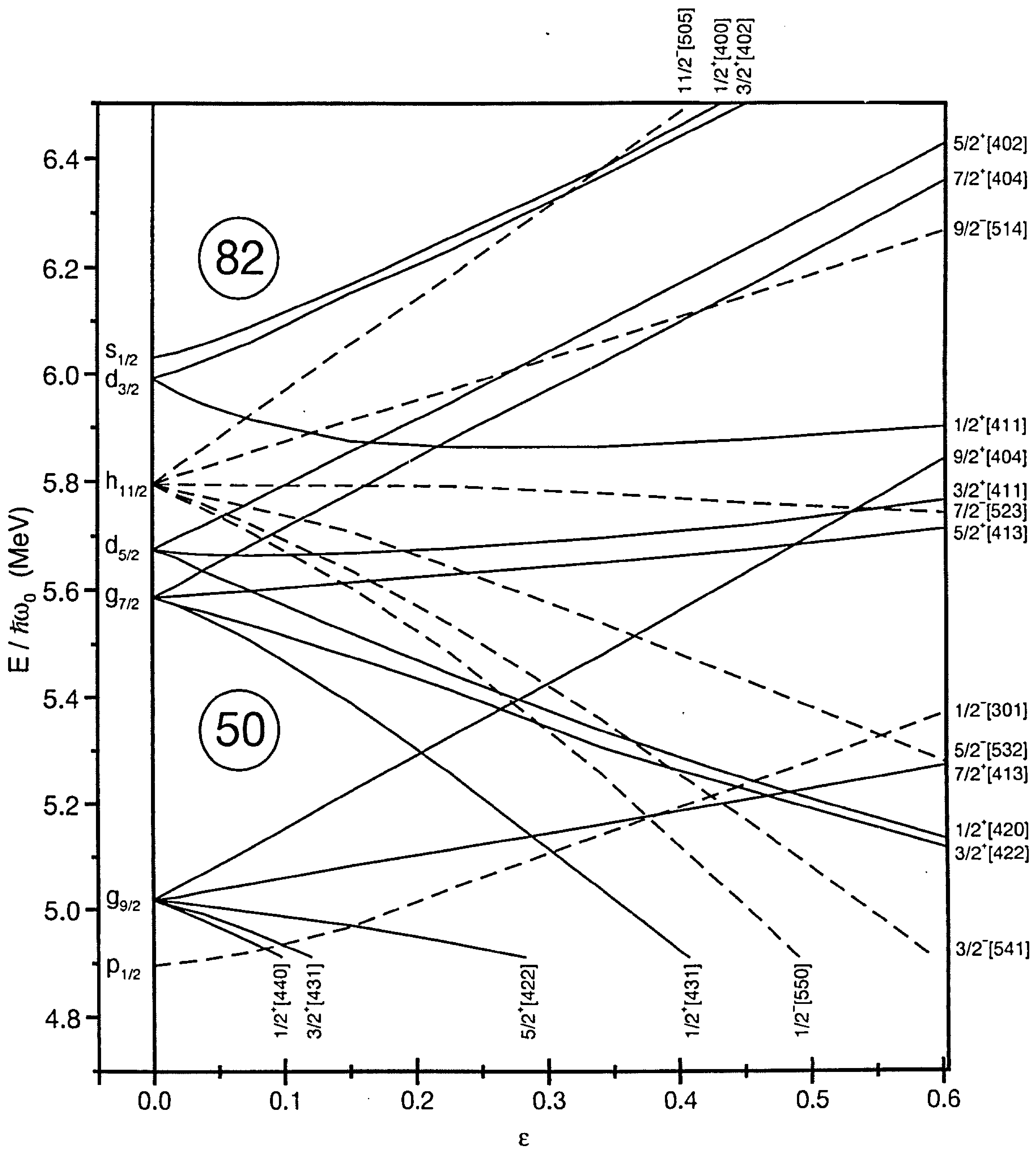

Figure 1.6: A Nilsson diagram calculated using a WS potential for orbitals with a range $50 \leq N \leq 82$. The magic numbers 50 and 82 are shown.

1.3 Nuclear Rotation

Quantum-mechanically, a spherical body can not rotate: this is due to the invariance of spherical shapes under rotation. Hence, for rotation to occur the nucleus has to exhibit some form of deformation. For example, taking the Cartesian coordinate, it can be seen that an ellipsoid can rotate about either x or y, while rotation is not allowed about the z-axis. In order to describe experimental spectra from rotating nuclei, both single-particle and collective models are necessary.

1.3.1 Single-particle Motion

Closed-shell nuclei have near-spherical symmetry and total angular momentum, $I = 0$, in the ground-state. Angular momentum is generated in these nuclei by the rearrangement of valence nucleons into different sub-orbitals close to the Fermi surface. The vector sum of the components of the orbitals occupied by these valence particles generates the total angular momentum of the nuclear state. The alignment of single-particle angular momenta j with the rotation axis gives rise to a large value of I. This characteristic behaviour can be seen in Figure 1.7.(b) for the nucleus ^{147}Gd.

1.3.2 Collective Rotation

In collective rotation, angular momentum can be generated by the coherent contribution of the individual nucleons. A deformed nucleus can rotate about an axis perpendicular to its symmetry axis (see Figure 1.7.(a) for the deformed nucleus ^{168}Hf). In this case, the sum of the projections on to the rotation axis gives the total angular momentum of the nucleus. In a rotational model, the collective rotational energy level can be given as:

$$E_{rot}(I,K) = \frac{\hbar^2}{2\mathcal{J}}\left[I(I+1) - K^2\right] \tag{1.29}$$

where I is the total collective angular momentum, K is its projection on the symmetry axis, and $\mathcal{J}$ is the moment of inertia of the nucleus. For high-spin nuclear structure

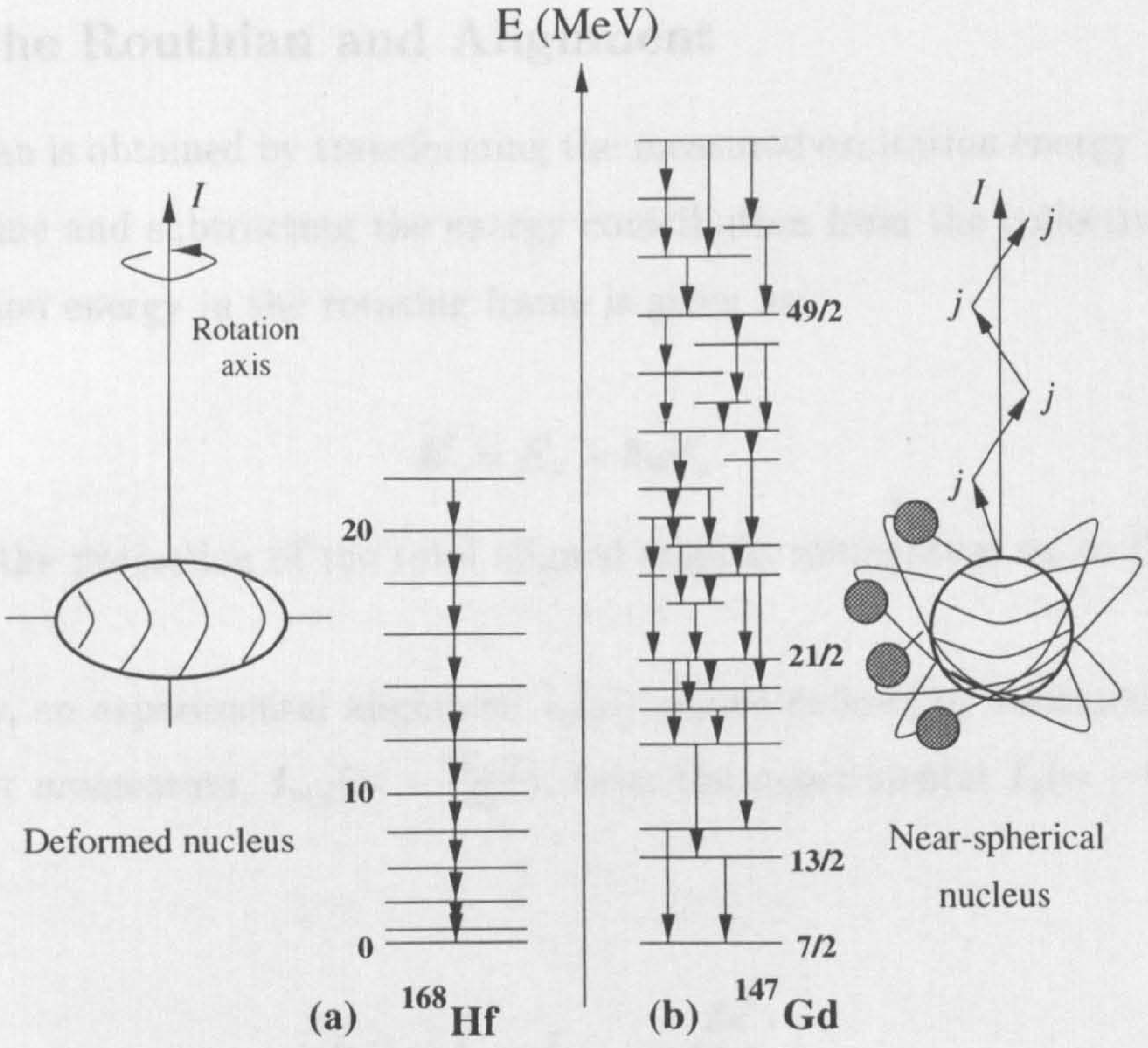

Figure 1.7: (a) collective rotation where the collective rotation happens around an axis perpendicular to the symmetry axis, (an example for ^{168}Hf), and (b) single-particle excitation where the angular momentum I is the sum of the projections on the symmetry axis, (an example for ^{147}Gd).

studies, $K \approx 0$ ($I \gg K$); therefore, the above equation may be simplified to:

$$E_{rot}(I) = \frac{\hbar^2}{2\mathcal{J}} I(I+1) \tag{1.30}$$

In a rotational cascade, a transition from one energy level to the next results in the emission of a γ-ray with energy

$$E_\gamma = E_{rot}(I) - E_{rot}(I-2) = \frac{\hbar^2}{2\mathcal{J}}(4I-2) \tag{1.31}$$

Nuclear rotation is usually described as a function of frequency and is defined as:

$$\hbar\omega = \frac{dE}{dI} \cong \frac{E_\gamma}{2} \tag{1.32}$$

1.3.3 The Routhian and Alignment

The Routhian is obtained by transforming the measured excitation energy E_x into the rotating frame and subtracting the energy contribution from the collective rotation. The excitation energy in the rotating frame is given as:

$$E' = E_x - \hbar\omega I_x \tag{1.33}$$

where I_x is the projection of the total aligned angular momentum on to the rotation axis (x).

Similarly, an experimental alignment $i_x(\omega)$ can be defined by subtracting a reference angular momentum, $I_{ref}(= -\frac{\delta E_{ref}}{\delta\omega})$, from the experimental $I_x(= -\frac{\delta E'}{\delta\omega})$ and is given by:

$$i_x(\omega) = I_x - I_{ref} = -\frac{\delta e'}{\delta\omega} \tag{1.34}$$

The alignment is related to the Routhian through the expression:

$$i_{th}(\omega) = -\frac{de'(\omega)}{d\omega} \tag{1.35}$$

The alignment information can be used to assist in the assignment of the structure of the nucleus.

1.3.4 Moments of Inertia

The excitation energy E of a nuclear state of spin I in a rotational band can be written as in equation(1.30):

$$E_{rot}(I) = \frac{\hbar^2}{2\mathcal{J}^0} I(I+1) \tag{1.36}$$

where $\mathcal{J}^0$ is the static moment of inertia of the state, and I is the angular momentum of the state. The x-projection of the angular momentum I_x in the rotational system is defined as:

$$I_x = \sqrt{I(I+1)} \tag{1.37}$$

The static moment of inertia can be derived using equations (1.36) and (1.37) and can be expressed as:

$$\mathcal{J}^{(0)} = \frac{\hbar^2}{2}\frac{{I_x}^2}{E} \tag{1.38}$$

There are two other moments of inertia: namely, the kinematic, $\mathcal{J}^{(1)}$, and the dynamic, $\mathcal{J}^{(2)}$, which can be used to explain the behaviour of the nucleus. Both moments of inertia ($\mathcal{J}^{(1)}$, $\mathcal{J}^{(2)}$) originate from the first and second derivatives of equation (1.36) respectively. Therefore, the kinematic moment of inertia is given as:

$$\mathcal{J}^{(1)} = \frac{\hbar^2}{2}\left(\frac{dE}{dI_x}\right)^{-1} = \hbar\frac{I_x}{\omega}. \tag{1.39}$$

The $\mathcal{J}^{(1)}$, moment of inertia provides information on the overall motion of the nucleus, while the $\mathcal{J}^{(2)}$ moment of inertia is responsive to single-particle alignments. The $\mathcal{J}^{(2)}$ moment of inertia is defined as:

$$\mathcal{J}^{(2)} = \frac{\hbar^2}{2}\left(\frac{d^2E}{dI_x^2}\right)^{-1} = \hbar\frac{dI_x}{d\omega}. \tag{1.40}$$

The kinematic and dynamic moments of inertia are related by:

$$\mathcal{J}^{(2)} = \mathcal{J}^{(1)} + \omega\frac{d\mathcal{J}^{(1)}}{d\omega} \tag{1.41}$$

For a rigid rotor, $\mathcal{J}^{(1)}$ does not depend on rotational frequency ω; so, $\mathcal{J}^{(1)} = \mathcal{J}^{(2)} = \mathcal{J}^{(rot)}$. If rotational states are assumed to decay by electric quadrupole moment (E2) γ-rays, $\mathcal{J}^{(1)}$ and $\mathcal{J}^{(2)}$ can be expressed as:

$$\mathcal{J}^{(1)} = \frac{(4I-2)\hbar^2}{2E_\gamma} \tag{1.42}$$

and

$$\mathcal{J}^{(2)} = \frac{4\hbar^2}{\Delta E_\gamma} \tag{1.43}$$

where ΔE_γ corresponds to the energy separation between two consecutive γ-rays in the band. The $\mathcal{J}^{(2)}$ dynamic moment of inertia is a useful quantity in the study of nuclei at high spin. It is also a useful parameter for interpreting superdeformed bands, where the excitation energy and spin are generally ambiguous quantities.

1.3.5 Band Crossing and Backbending

It has been shown that the first backbending which occurs in light rare-earth nuclei is probably due to the crossing of a pair of aligned $i_{13/2}$ neutrons [Gr73]. The band crossing arises when the Coriolis force becomes large enough to overcome the pairing force between the two $i_{13/2}$ neutrons and is able to align their angular momenta with the axis rotation. Subsequently, it becomes energetically favourable to generate angular momentum by the alignment of the two $i_{13/2}$ neutrons rather than by collective rotation.

The backbend phenomenon was first observed by Johnson *et al.,* [Jo71] in the ground-state rotational bands of ^{162}Er, ^{158}Dy and ^{160}Dy. This observation was interpreted as the crossing of two bands of different internal structures. In several cases, backbending has been observed due to the crossing of a second band below the ground state rotational band. For the nature of this second band, three possible explanations have been given. They are:

1. A sudden change in nuclear deformation [Th73].
2. A collapse of the pairing correlation [MV60].
3. An alignment of the angular momentum of two high-j nucleons with the rotational angular momentum [Ste75].

For example, in the case of the yrast band in nucleus ^{158}Er [Le77], the $I(I+1)$ rule breaks around $\hbar\omega \approx 0.3$ and around $\hbar\omega \approx 0.4$ and produces a large backbend in its alignment plot, as is shown in Figure 1.8. The "sharpness" of a backbend is dependent on the interaction strength of the band crossing. The anomalous behaviour

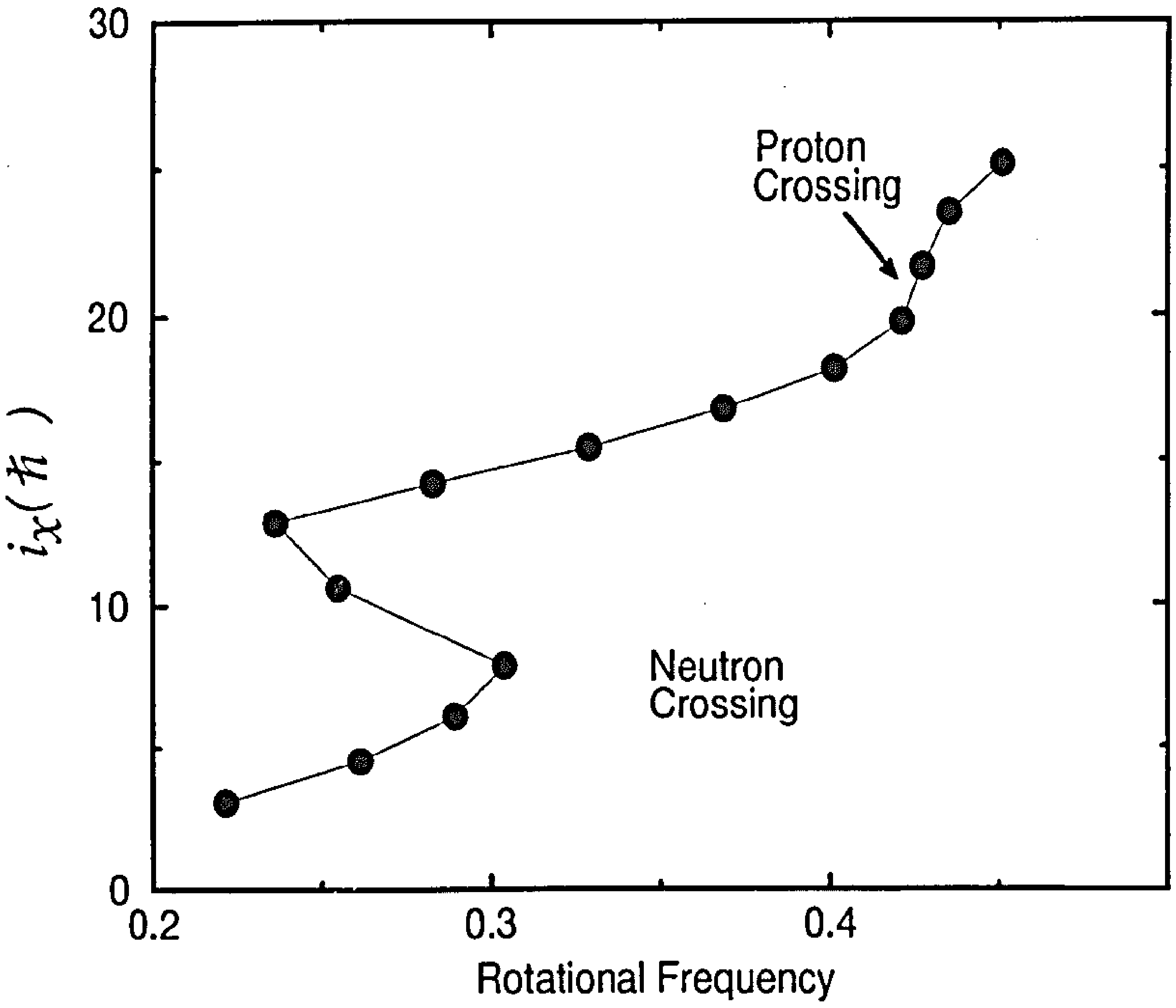

Figure 1.8: The alignment i_x plotted versus rotational frequency for the yrast band in ^{158}Er to show neutron and proton crossing in this band.

of the interacting superdeformed band is observed in ^{158}Er. The backbend is observed very sharply for a weak interaction *i.e.* for $i_{13/2}$ neutrons around $\hbar\omega \approx 0.3$ MeV (see Figure 1.8). At higher spins, a second discontinuity (upbend) is due to either additional $i_{13/2}$ neutrons or the crossing of a pair of aligned $j_{11/2}$ protons. This second crossing is much smoother and occurs around $\hbar\omega \approx 0.4$ MeV (shown in Figure 1.8). This is a characteristic of a much stronger interaction.

1.4 The Cranked Shell Model

The Cranked Shell Model gives a microscopic description of a rotating nucleus. The Cranked Shell Model was first described semi-classically by Inglis [In54] through the introduction of a "cranked coordinate system" that rotates around a fixed axis in space with a constant angular velocity, ω. The advantage of the Cranked Shell Model is that it describes the total angular momentum as the sum of the single-particle angular momenta which is described as:

$$I_x(\omega) = \sum_{i=1}^{N} j_{x,i} \tag{1.44}$$

where j_x is the projection of the single-particle angular momentum on to the rotation axis. The rotation of the nucleus about the x-axis perpendicular to the symmetry z-axis with a rotational frequency (ω) can be represented by the rotation operator $\hat{R}$, which describes the transformation from the laboratory frame to the rotating frame. $\hat{R}$ is given by:

$$\hat{R} = \exp\left[\frac{-i\omega t j_x}{\hbar}\right] \tag{1.45}$$

so that, in the rotating frame, the wave-function of the nucleon is given by:

$$\Psi_{rot} = \hat{R}\Psi_{lab} = \exp\left[\frac{-i\omega t j_x}{\hbar}\right]\Psi_{lab}. \tag{1.46}$$

The general time-dependent Schrödinger equation in the rotating frame is

$$-i\hbar\frac{d}{dt}\Psi_{rot} = H\Psi_{rot} \tag{1.47}$$

Differentiation of equation (1.46) and substituting into equation (1.47) reveals the cranking Hamiltonian

$$\hat{H}_{rot} = \hat{H}_{lab} - \omega j_x \tag{1.48}$$

where the first term, $\hat{H}_{lab}$, corresponds to the Hamiltonian in the laboratory system, and the second term, ωj_x, accounts for the effects of the centrifugal and Coriolis forces on the individual nucleons. The Coriolis and centrifugal force tend to align the single-particle angular momentum with the rotation x-axis and the symmetry z-axis respectively.

1.4.1 Parity and Signature

The cranking Hamiltonian does not conserve time-reversal symmetry or rotational invariance. The parity π and signature α are the only valid quantum numbers which remain in a rotating nucleus. Therefore, nuclear states in a rotating nucleus are labelled in terms of the parity of the state and the quantity of the signature.

If the parity operator $\hat{\pi}$ acts on a wave-function $\Psi(x)$, then for odd parity it needs to be

$$\hat{\pi}\Psi(x) = \Psi(-x) = -\Psi(x) \tag{1.49}$$

and for a nucleus of even parity

$$\hat{\pi}\Psi(x) = \Psi(-x) = +\Psi(x). \tag{1.50}$$

Parity is expressed as ± 1, which are the eigenvalues of the parity operator, $\hat{\pi}$. Hence, nuclear states are labelled $+$ or $-$ depending upon the effect of the reflection operator on the nuclear wave-function. Therefore, the total parity of the nucleus is determined by the product of the parities of all occupied levels.

The signature of a particular state can be similarly obtained by the effect of the rotation operator $\hat{R}$, which acts on the nuclear state u_α and is given by:

$$\hat{R}(u_\alpha) = exp\,(-i\pi\alpha)\,u_\alpha. \tag{1.51}$$

The signature α can be related to the angular momentum I by:

$$\alpha = I \mathrm{mod} 2 \tag{1.52}$$

Thus,

$$\alpha = 0 \text{ or } 1 \text{ for even-A nuclei}$$
$$\alpha = \pm\tfrac{1}{2} \text{ for odd-A nuclei.}$$

For a non-rotating deformed nucleus, the nucleons' orbits are doubly degenerate with respect to Ω. However, these levels are split by the rotation into two states of signature + or −, and these two energy levels are known as signature partners. For a rotating nucleus, each energy level is split into two energy levels of opposite signatures: $\alpha = +\frac{1}{2}$ and $\alpha = -\frac{1}{2}$. The magnitude of this so-called "signature splitting" depends on the angular momentum projection on to the rotational axis, j_x, and the magnitude of the rotational frequency.

Since the Coriolis force has little effect on low-j_x orbitals, signature partners, therefore, show very little signature splitting. However, the Coriolis force has a much greater effect on the orbits with high-j_x and low-Ω; therefore, there is large signature splitting. In this case, the effects of deformation and rotation on the energy levels of different nuclear potentials are summarised in Figure 1.9, showing from left to right the $N = 2$ state in a HO potential, the splitting effects in a WS potential, the addition of spin-orbit coupling, and then the effect on the nucleus of deformation and rotation.

1.4.2 Pairing

The pairing force is the short-range attractive interaction which exists between nucleons of the same angular momentum state, j. There is considerable experimental evidence to show the existence of this force. For example, it is observed that all even-even nuclei have ground-state spins of $I = 0\hbar$, which indicates that the nucleons are arranged in such a way that their angular momenta cancel out. In the case of odd-A nuclei, the ground-state spin is determined by the spin of the orbital occupied by the odd nucleon. The total binding energy of odd-A nuclei is found to be less than the mean binding energies of the two neighbouring even-even nuclei. It is also found that the energy-spacing between the ground-state and the first non-rotational excited state in even-even nuclei is greater than 1 MeV, whereas this gap is very small in odd-A nuclei.

Paired particles occupy time-reversed orbits, those orbitals close to the Fermi surface, are in another pair of time-reversed orbit, also resulting in a smearing of the nuclear Fermi surface (see Figure 1.10). In the independent particle shell model (broken curve), the levels are occupied up to a specific energy, λ. If the energy

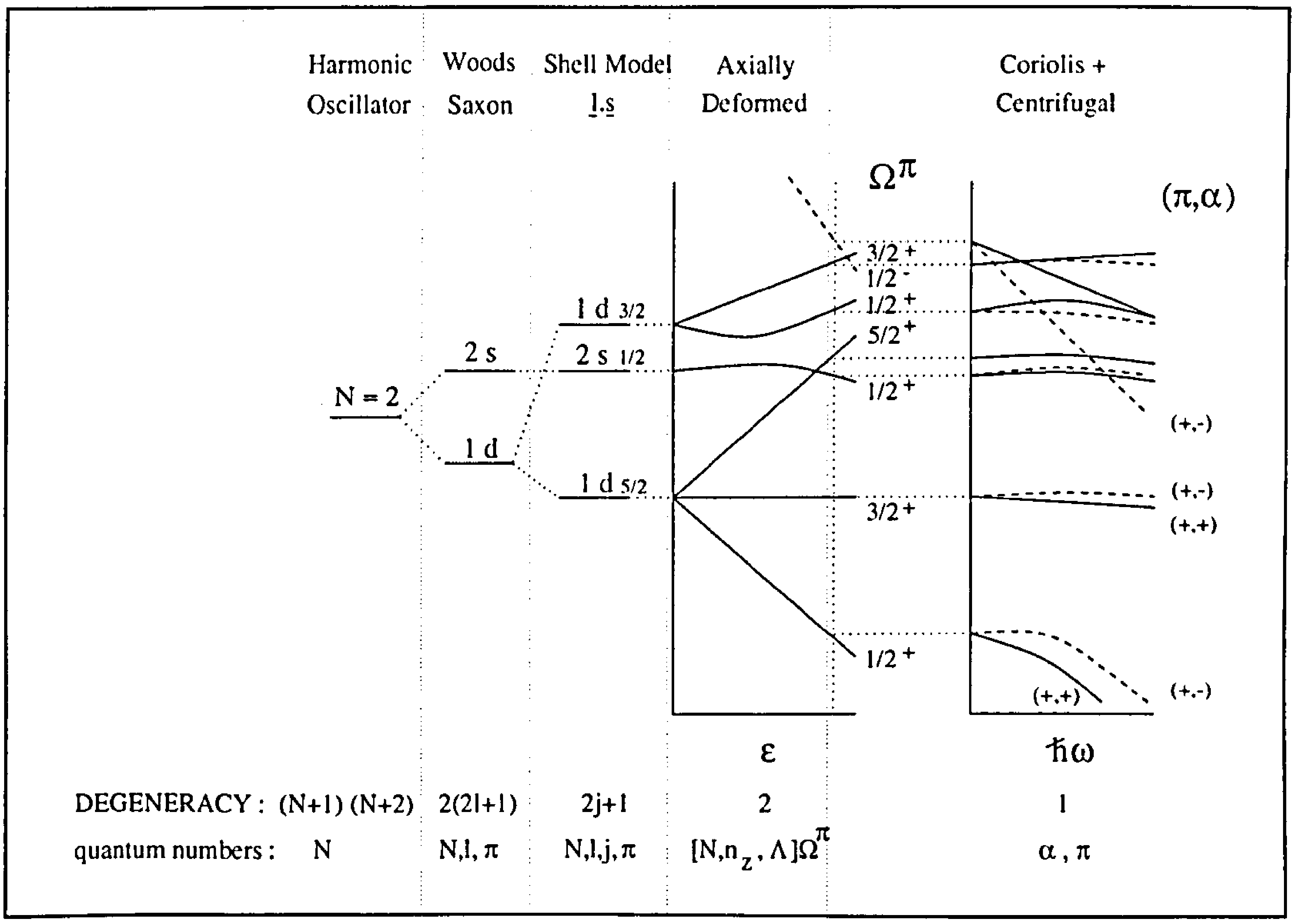

Figure 1.9: A schematic energy spectrum of N = 2 shell generated by various potentials. For each potential, the characteristic quantum numbers are indicated as π for the parity, N for the total oscillator quantum number, l for the orbital and j for the total angular momentum. For the axially symmetric case, n_z, Λ and Ω are the components along the nuclear symmetry axis of N, l and j respectively. The signature exponent α is related to the signature eigenvalue.

is greater than λ, the occupation-probability suddenly drops to zero. The pairing interaction allows configuration-mixing in such a way that the states close to λ are only partly occupied. The broken curve in Figure 1.10 shows that the Fermi surface loses its sharpness and is replaced by a diffuseness parameter 2Δ (where Δ is the pairing gap).

The similarity between the structures of super-conducting materials and nuclei has been proved ([BCS57] by the BCS theory [BMP58]). By considering paired nucleons, the theory changes from an interacting particle-hole system to a non-interacting "quasi-particle" scheme.

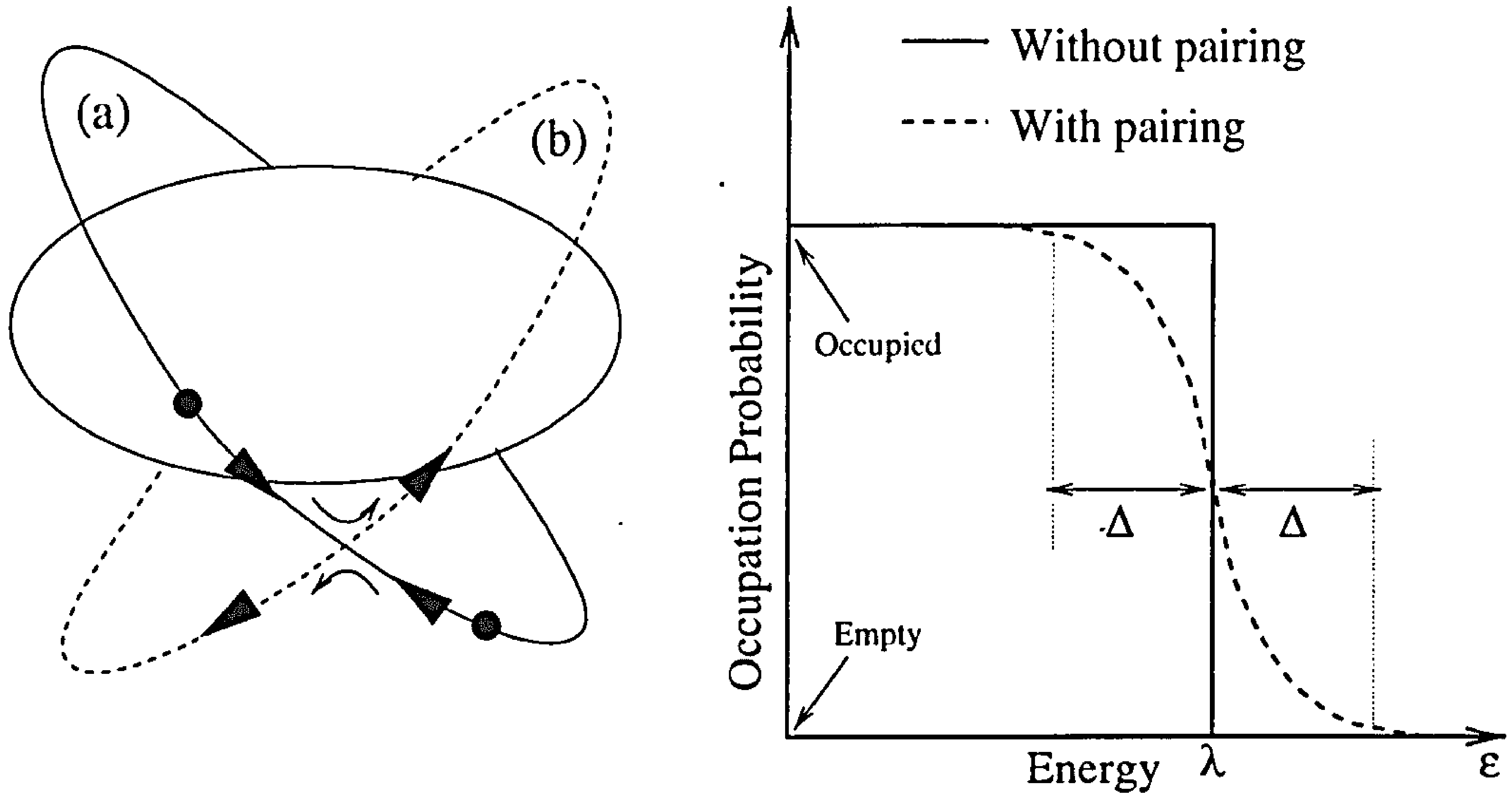

Figure 1.10: Ground-state occupation-probability as a function of shell energy. Solid line : no pairing interaction between shells. Dashed line: with pairing interaction between time-reversed states. λ is the Fermi energy; 2Δ is a diffuseness parameter ($= 2 \times$ pair gap). The left-hand side figure shows scattering between paired nucleons in orbit (a) into a second time-reversed orbit (b) which causes smearing of the Fermi Surface (right-hand side figure).

1.4.3 The Strutinsky Shell-Correction Method

The LDM is appropriate for describing the bulk properties of a nucleus, but it ignores the effect of the single-particle structure. The shell model reproduces single-particle effects but fails to reproduce bulk properties. On the other hand the Strutinsky Shell Correction Method [St66, St67] combines both these models to give a total energy description of the nucleus. In this procedure, it is convenient to separate the total energy, E_{tot}, into two terms:

1. a macroscopic term, which describes the bulk properties of the nucleus and represents a smooth density of states, E_{LD}.
2. a microscopic term, which corrects the oscillation in energy due to valence nucleons. These corrections are calculated from the shell model.

Therefore, the total energy can be given as:

$$E_{tot} = E_{LD} + \delta E_{shell} \tag{1.53}$$

The shell-correction energy is obtained by the sum of all the single-particle contributions, e_i, which divide into an oscillating part, $\delta Eshell$, and a smoothly-varying part, $\bar{E}_{shell}$, and is given as:

$$E_{shell} = \sum_{i=1}^{A} e_i = \delta E_{shell} + \bar{E}_{shell} \tag{1.54}$$

Since energy levels occur in shells, the level-density is not constant and does not show regular variations. It is useful to define the level-density concept, $g(e)$, as:

$$g(e) = \sum_{i=1} \delta(e - e_i) \tag{1.55}$$

where $\delta(e - e_i)$ is a Dirac delta function. This definition allows the calculation of the particle number, A, which is given as:

$$A = \int_{-\infty}^{\lambda} g(\epsilon) d\epsilon \tag{1.56}$$

where λ is the chemical potential. The normalisation procedure replaces the discrete level-density with a smooth level-density given by:

$$\bar{g}(e) = \sum_{i} S(e - e_i) = \frac{1}{\gamma} \int_{-\infty}^{+\infty} g(e) f\left(\frac{e - e'}{\gamma}\right) \delta e \tag{1.57}$$

where $S(e - e_i)$ is a smooth function and $f\left(\frac{e-e'}{\gamma}\right)$ is a Gaussian of width $\gamma \approx \hbar\omega_0$.

In order to provide a complete description of the nucleus, pairing should also be included in calculations. The E_{LD} term in equation (1.53), already includes the macroscopic part of the pairing energy. The correction, δE_{pair}, is calculated from the BCS model and is given as:

$$E_{pair} = \delta E_{pair} + \bar{E}_{pair} \tag{1.58}$$

The total energy can be expressed as:

$$E_{tot} = E_{LD} + \delta E_{shell} + \delta E_{pair} \tag{1.59}$$

A detailed calculation of the above term and the inclusion of nuclear rotation parameters can be found in the relevant references [St66, St67].

Chapter 2

The Experimental Details and Analysis

2.1 Heavy-Ion Fusion-Evaporation Reactions

The heavy-ion fusion-evaporation reaction provides the best method of populating states at the extremes of both spin and exact energy. This method was first proposed by Niels Bohr in 1936 [Bo36]. The mechanism of the heavy-ion fusion-evaporation reaction is illustrated in Figure 2.1 and is described below:

1. Projectile nuclei are accelerated to an energy E_{beam} using a particle accelerator, such as a cyclotron, and directed towards a target.

2. The beam nuclei interact with the target nuclei and, $\approx 10^{-20}$ seconds later, they may fuse to form a highly-excited rapidly-rotating compound nuclear system. In order to produce this highly-excited compound system, the projectile must have sufficient kinetic energy to overcome the Coulomb barrier that exists between the two nuclei. In the laboratory frame, the size of this barrier V_{lab} is given by :

$$V_{lab} = \left(\frac{A_p + A_t}{A_t}\right) \frac{1.44 Z_p Z_t}{1.2(A_p^{1/3} + A_t^{1/3} + 2)} \tag{2.1}$$

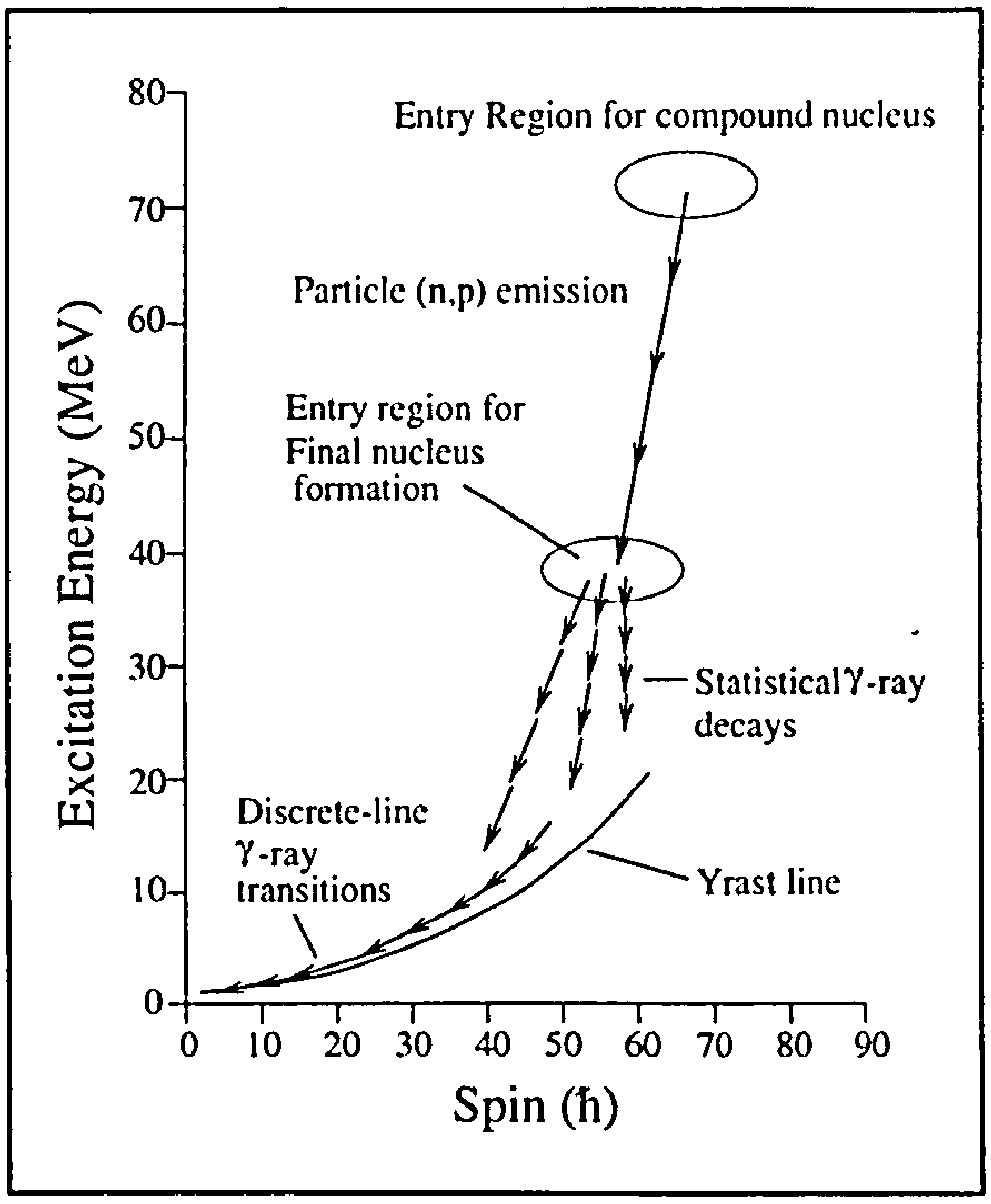

Figure 2.1: A schematic diagram of the process involved in the de-excitation of a compound nucleus formed in a Heavy Ion Fusion-Evaporation Reaction.

where A represents the mass number, Z represents the atomic number, and the subscripts p and t refer to the projectile and target nuclei respectively.

3. Once the compound system is formed, it can fission (if the excitation energy or total angular momentum or both is greater than the fission barrier) or it can lose energy via particle evaporation. This involves protons, neutrons and α particles being lost from the compound system and removing a large amount of energy but very little spin (e.g. neutrons remove $\approx$ 10 MeV of energy and 1-2 $\hbar$ of angular momentum).

4. When the excitation energy of a compound nucleus falls below the energy threshold for particle emission 10 MeV above the yrast line (defined as the sequence of states which have the lowest excitation energy at a particular spin value), the nucleus loses energy via a cascade of γ-rays. These γ-rays remove a large amount of energy but very little angular momentum.

5. When the excitation energy of the compound nucleus has decayed to 2 to 3 MeV above the yrast line, it starts emitting mostly quadrupole γ-rays which each remove 2 $\hbar$ of angular momentum from the system. This mode of de-excitation continues until the nuclear ground state is reached (at $E_{ex} = 0$ MeV).

2.1.1 Target and Beam Requirements

Although each experiment requires a specific target, there are some general features that need to be considered when choosing the target. The target material used for the foils should be isotopically enriched to a high purity-level (95%-99%) in order to reduce contamination which may cause unwanted reaction products. The target needs to have a high melting-point (> 500 K); this ensures that the target thickness and, therefore, the radiation rate remain constant throughout the experiment. Beam energy also reduces as it passes through the target.

The choice of target thickness is a compromise between obtaining high statistics and good energy γ-ray resolution. A thick target provides high statistics because there is a high probability of a heavy-ion fusion reaction occurring between the projectile and the target nuclei. However, thick targets cause poorer resolution due to broadening effects caused by the slowing down of the recoiling nuclei. This is only true for high-spin states. Thin targets are used to ensure that all γ-rays are emitted from recoiling nuclei which are not slowed down in the target material. They are often backed with a suitable backing to provide support, if such a backing is required. Thin targets are generally stacked together, allowing good energy resolution and high statistics.

2.2 Interaction of γ-rays with Matter

There are three main types of interaction mechanism by which a γ-ray can interact with matter. These methods of interaction are illustrated in Figure 2.2 and are described below:

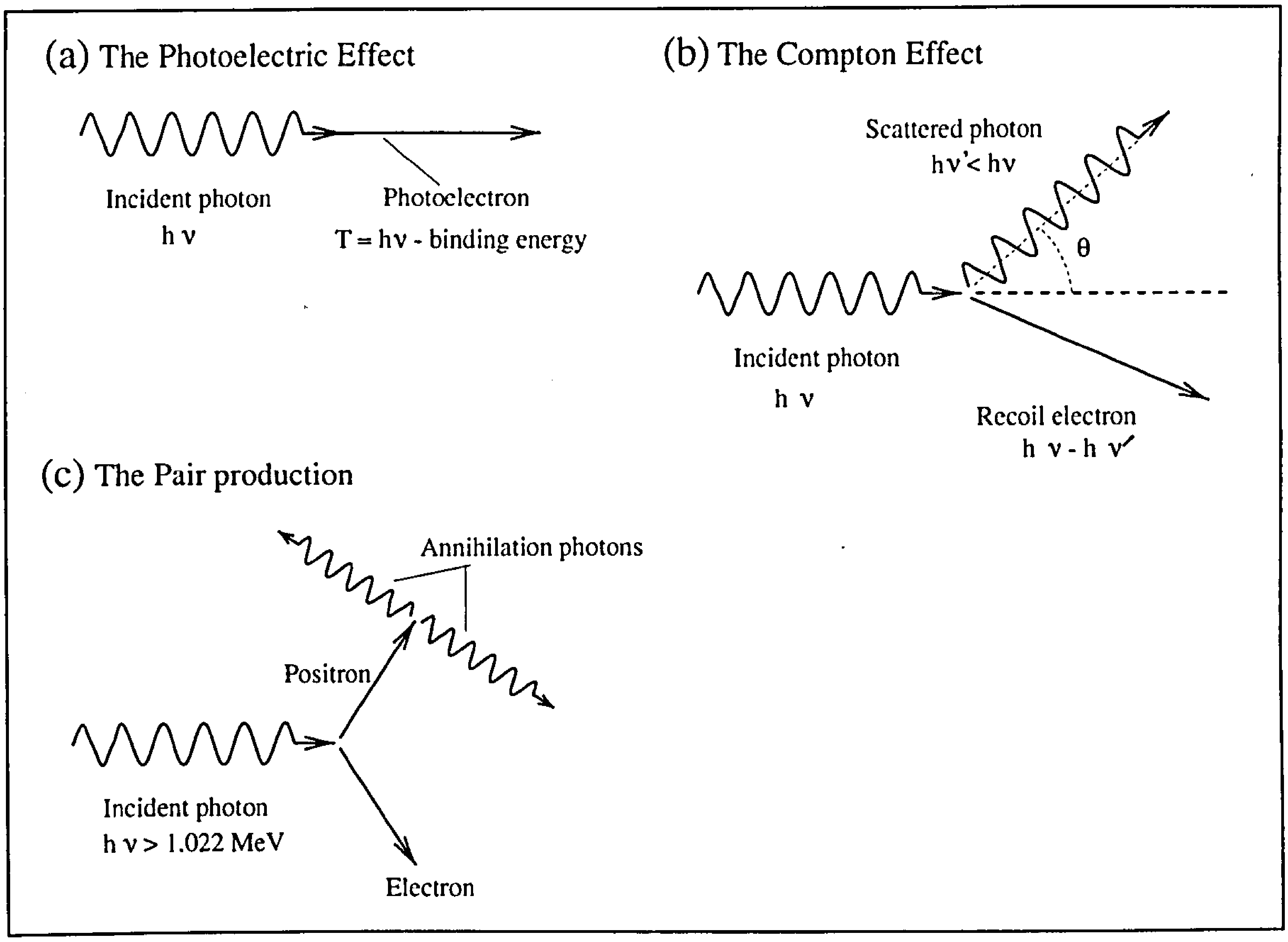

Figure 2.2: The three main interaction processes of γ-rays with matter: (a) the Photoelectric effect, (b) the Compton effect, and (c) Pair production.

The Photoelectric effect : This occurs when a γ-ray photon ionises one of the absorber atoms, transferring all its energy to an atomic electron (called a photoelectron) (see Figure 2.2.(a)). This process is the most likely method of interaction for γ-rays of low energy ($<$ 200 keV). The energy (T) of the photo-electron is given by:

$$T = h\nu - E_b \tag{2.2}$$

where $h\nu$ is the energy of the incident γ-ray photon and E_b is the binding-energy of the photo-electron.

The Compton Effect : The incoming γ-ray photon scatters off an atomic electron through an angle θ with respect to its original direction (see Figure 2.2.(b)). In this process, a portion of the γ-ray energy is transferred to an atomic electron. From a conservation of energy and momentum, the final energy of the scattered photon ($h\nu'$) can be shown to be :

$$h\nu' = \frac{h\nu}{1 + (\frac{h\nu}{m_o c^2})(1 - cos\theta)} \tag{2.3}$$

where $h\nu$ is the incident γ-ray energy, $m_o c^2 (= 511$ keV) is the electron rest-mass energy, and θ is the angle through which the γ-ray is scattered.

Note that from the equation (2.3), a wide range of energy-transfer is possible in the scattering process, depending on the scattering angle, θ. For example, maximum energy-transfer occurs for $\theta = 180^\circ$. The Compton effect is the most likely process by which γ-rays in the energy range 200 - 1000 keV interact with matter.

Pair Production : If the incident γ-ray energy is greater than 1.022 MeV, then a γ-ray can produce an electron-positron pair (but only when in the vicinity of the Coulomb field of an atom). The excess energy ($h\nu-$ 1.022 MeV) is equally-divided between the electron and positron as kinetic energy. When the positron slows down to an energy comparable with that of an atomic electron, annihilation takes place, creating two annihilation photons each of energy 511 keV, (Figure 2.2.(c)).

2.3 γ-ray Detectors

There are two different types of detector used today in γ-ray spectrometer arrays: scintillation and semiconductor.

2.3.1 Scintillation Detectors

Scintillation detectors work by converting the energy deposited by ionising radiation into pulses of light via electron excitation. This process occurs because electrons in the valence band of the scintillator are excited to the conduction band due to the interaction of ionising radiation, such as a γ-ray. These electrons can then decay back to the valence band with the emission of a photon. A photomultiplier tube is used to convert this optical radiation into an electric current proportional to the energy deposited in the scintillator material.

The energy-resolution of scintillation detectors is poor in comparison with a semiconductor detector; this is due to statistical fluctuations in the number of photoelectrons and discrepancies within the photomultiplier tube. However, the advantages of a scintillator detector are their transparency to their own photo-emission, linear energy conversion, and short decay-times. The advantages of a scintillator material are its high density and high atomic number (since they derive good photoelectric absorption).

There are different types of material that can be used as a scintillator: these include bismuth germinate, $Bi_4Ge_3O_{12}$ (BGO) or sodium iodide activated with thaelium (NaI(Tl)). These materials are not usually used in primary detectors, but are used more commonly for anti-Compton shielding [BS96]. In the case of the GAMMASPHERE [Lee90] detector array (see Section 2.4.1), the detector shields utilise BGO.

2.3.2 Semiconductor Detectors

Semiconductor detectors essentially work as solid state ionisation detectors. In pure semiconductors, a valence band (full of electrons) and an empty conduction band are separated by a band gap. Electrons can be excited from the valence band, leaving behind a hole as they move across into the conduction band. In an intrinsic semiconductor, the number of electrons and holes is equal.

The semiconductor detector material used for detecting γ-rays in γ-ray spectroscopy is high-purity germanium (HPGe) crystals. The germanium detector is based on a reverse-biased p-n junction diode [Kn89]. As p- and n-type semiconductors are brought into contact, there is a migration of charges which results in a depletion-region (where there are no free charge carriers) between the two semiconductors. This depletion-region constitutes an active volume where radiation can interact and be detected. Furthermore, the depletion region can be increased by applying a reverse bias voltage to the semiconductor material, in our case HPGe. A typical bias voltage is between 1-3 kV.

Ionising radiation interacts with the semiconductor materials in the depletion-region, creating electron-hole pairs. These charge carriers are swept towards the +ve and −ve electrodes due to the electric field generated by the bias voltage. As the number of particle-hole pairs is directly proportional to the energy deposited, the γ-ray energy can be determined from the residual current pulse. The main advantage of using a semiconductor material is the relatively small ionisation energy ($\approx$ 3 eV), which ensures a large number of charge carriers per interaction. This means that the the statistical fluctuations in the number of charge-carriers are reduced and a large amount of charge per pulse leads to a good signal-to-noise ratio. The HPGe detectors are operated at liquid nitrogen (LN_2) temperatures in order to reduce the thermal noise.

2.3.3 Compton Suppression

Photoelectric events are the most important interaction between the incident γ-ray and the detector for the γ-ray energies studied during the course of this work. When an incoming γ-ray interacts with the detector material, it can scatter out of the detector, leading to incomplete energy deposition in the detector. Background generated in this manner can be minimised by surrounding the germanium detector by scintillator material to detect the Compton Scattered γ-ray (this type of detector is known as an escape-suppressed spectrometer). A typical escape-suppressed spectrometer consists of two parts: the HPGe detector and the BGO suppression shield with a BGO backplug. Figure 2.3 illustrates a GAMMASPHERE escape-suppressed spectrometer.

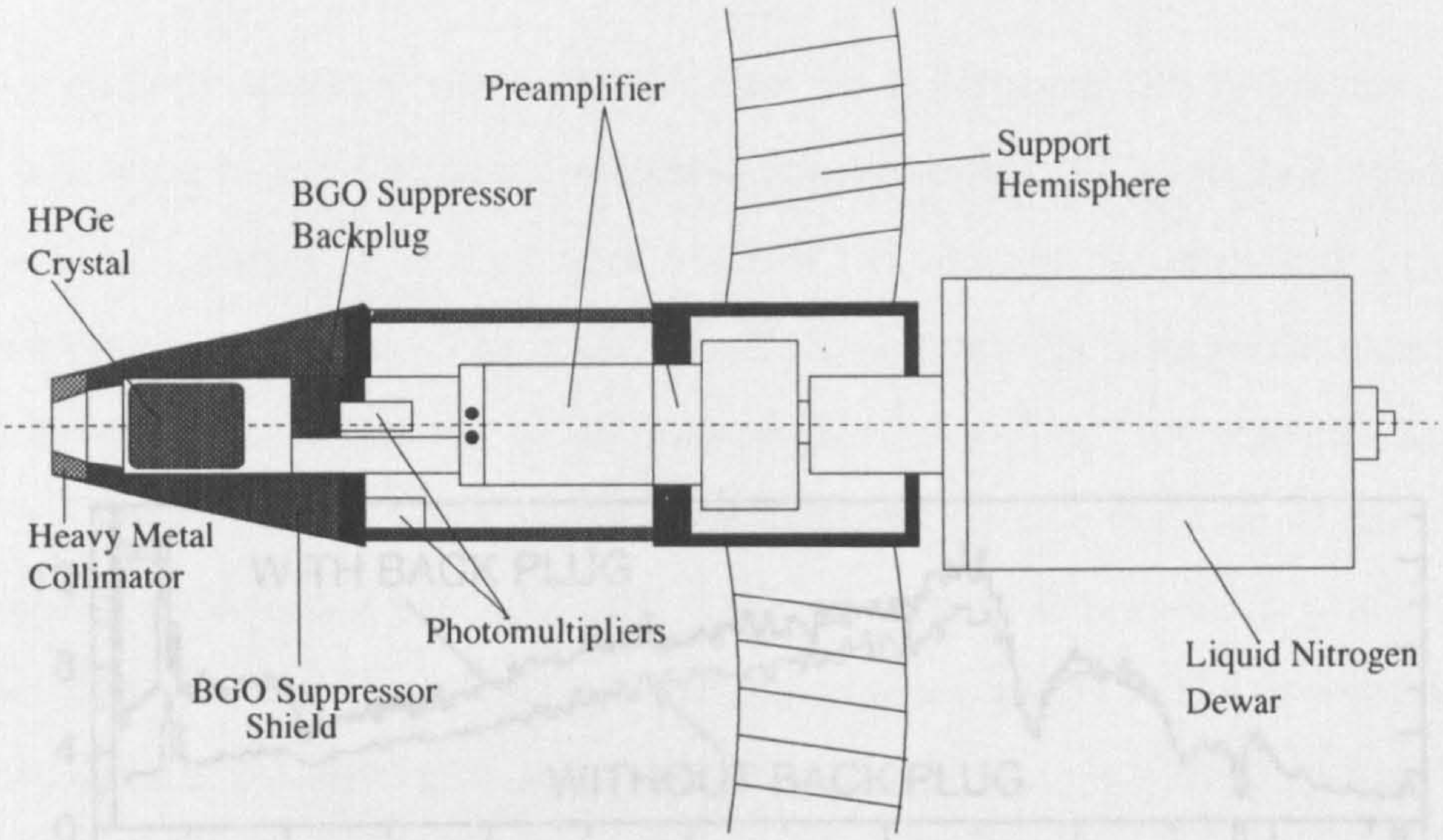

Figure 2.3: A schematic diagram of an escape-suppressed germanium detector used in a GAMMASPHERE array.

If γ-ray scattering occurs in both the germanium and BGO detectors, then a Compton scatter can be electronically suppressed and the event is rejected. Unsuppressed HPGe detectors typically have peak-to-total value (PT) of $\approx 20\%$. With the use of the escape-suppression system, the PT will improve to $\approx 60\%$ [BS96], and this system has a resolution of $\Delta E_\gamma \approx 2.5$ keV at 1300 keV. The spectra obtained with a ^{60}Co source taken with and without Compton suppression of the germanium detector are compared in Figure 2.4.(a). Ideally, such a spectrum would consist of just two ^{60}Co photopeaks at the energies of 1173 keV and 1333 keV (two thin peaks on the right side of the spectrum in Figures 2.4.(a),(b)). It has been shown by Baxter [Ba92] that, when a backplug is incorporated, the PT values are $\approx 10\%$ better than the suppressed values without the backplug (see Figure 2.4.(b)). In addition, in the same figure, the Compton edges (two broad peaks just below the photopeaks) can be clearly seen.

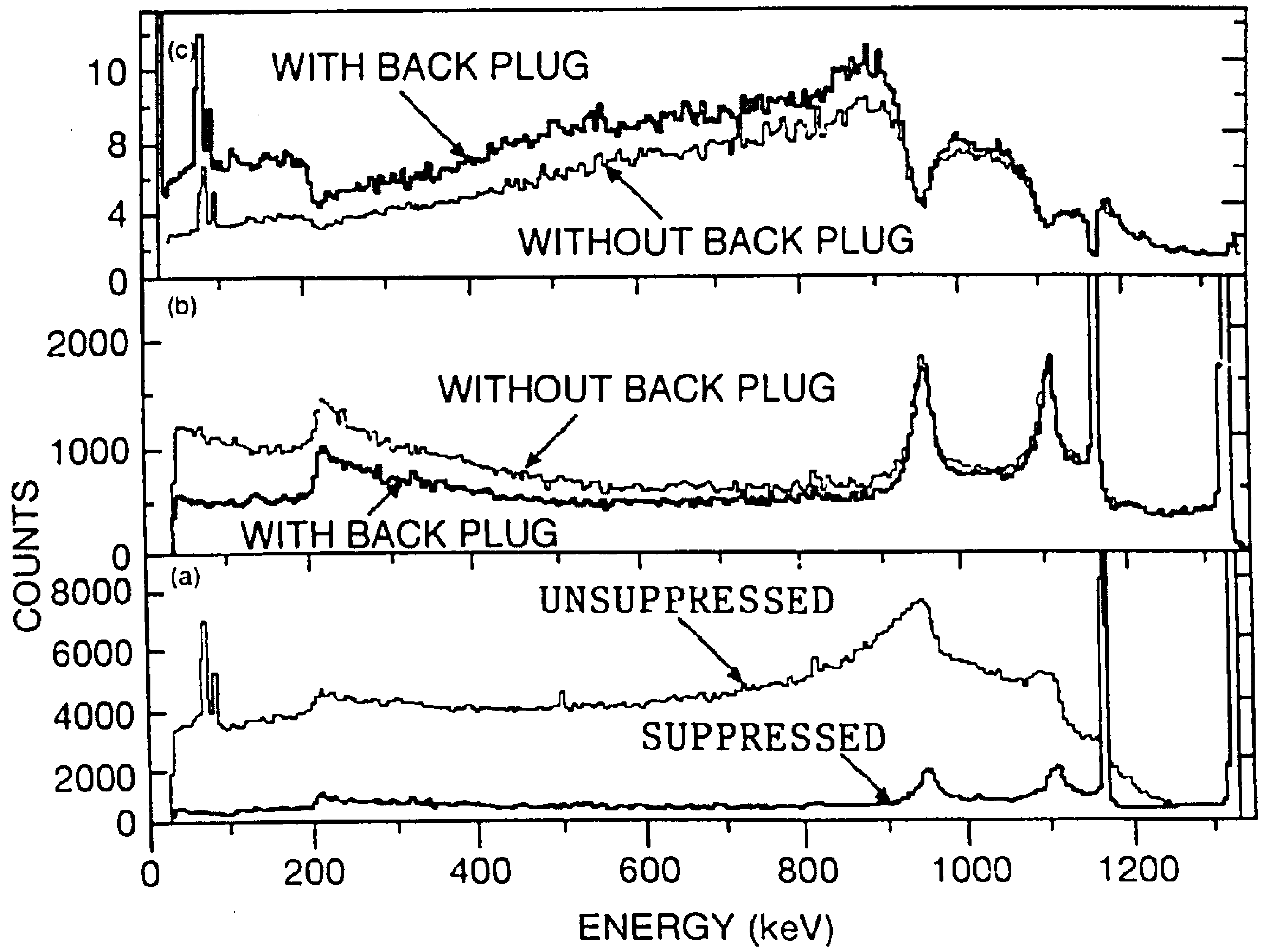

Figure 2.4: The γ-ray spectra for a ^{60}Co source shows (a) the effect of using Compton suppression with a ^{60}Co source; (b) suppressed spectra with and without backplug contribution to the suppression; (c) the ratio of the unsuppressed to the suppressed spectrum with and without backplug contribution to the suppression.

2.4 Arrays of Ge Detectors

High-spin nuclear spectroscopy is performed by measuring the properties of γ-rays emitted following heavy-ion fusion-evaporation reactions. This reaction tends to form the nucleus of interest in a high-spin state which decays by emitting a cascade of mutually-coincident γ-rays. The detection of these γ-rays by a single detector provides minimal information about the properties of the transitions (the energies and intensities). The ideal tool for γ-ray spectroscopy would be one capable of measuring all the individual γ-rays in a cascade with 100% efficiency. However, in practical terms, this is not possible; but there have been significant advances in the development of γ-ray spectrometers consisting of large numbers of germanium detectors (or "arrays"). Today, the most advanced arrays are EUROBALL [No94, BS96] and GAMMASPHERE [Lee90].

2.4.1 The GAMMASPHERE Array

In this thesis, the GAMMASPHERE spectrometer was used to measure the energies, intensities and correlations between γ-rays. The GAMMASPHERE array is designed to hold up to 110 escape-suppressed HPGe detectors, packed closely in a 4π arrangement. The support frame is based on a configuration of a 122 element polyhedron comprising 110 hexagonal and 12 pentagonal faces. The 12 pentagonal faces are for beam access, support structures and specialised detectors while the 110 hexagonal faces are used for mounting the escape-suppressed HPGe detectors. The suppression performance of this type of escape-suppressed HPGe detector has been reported in [Ba92].

Figure 2.5 shows a close-up photograph of the array with one quarter of the detectors installed. The full GAMMASPHERE array is composed of two hemispheres, each of which can rotate ± 90 degrees, thereby allowing easier access to the detector positions at the top and bottom of the array. In both hemispheres, the Ge detectors are positioned at the following angles relative to the beam axis : 5 detectors at 17.3° , 5 at 31.7° , 5 at 37.4° , 10 at 50.1° , 5 at 58.3, 10 at 69.8, 5 at 79.2° , 5 at 80.7 and 5 at 90°. When the array is closed, the distance between the target and detector is $\approx$ 25 cm. The full implementation of the GAMMASPHERE array will have 80 segmented [Mac94] detectors in the central section. Increased segmentation enhances the resolving-power of the array. The resolving-power (R) of the array can be expressed by the equation (2.4):

$$R = \left(\frac{SE_\gamma}{\Delta E_\gamma} \times PT \right). \tag{2.4}$$

SE$_\gamma$ is the average peak separation and ΔE_γ is the resolution of detectors.

The high resolving-power provided by the GAMMASPHERE reveals new scientific opportunities for a broad range of nuclear studies, such as superdeformed [Tw86] and hyperdeformed states. The full GAMMASPHERE array with 110 detectors will have a total photopeak efficiency of 9.4% and a resolving-power of 9.4 which will provide a limit of observation of $\sim 3 \times 10^{-5}$ [BS96].

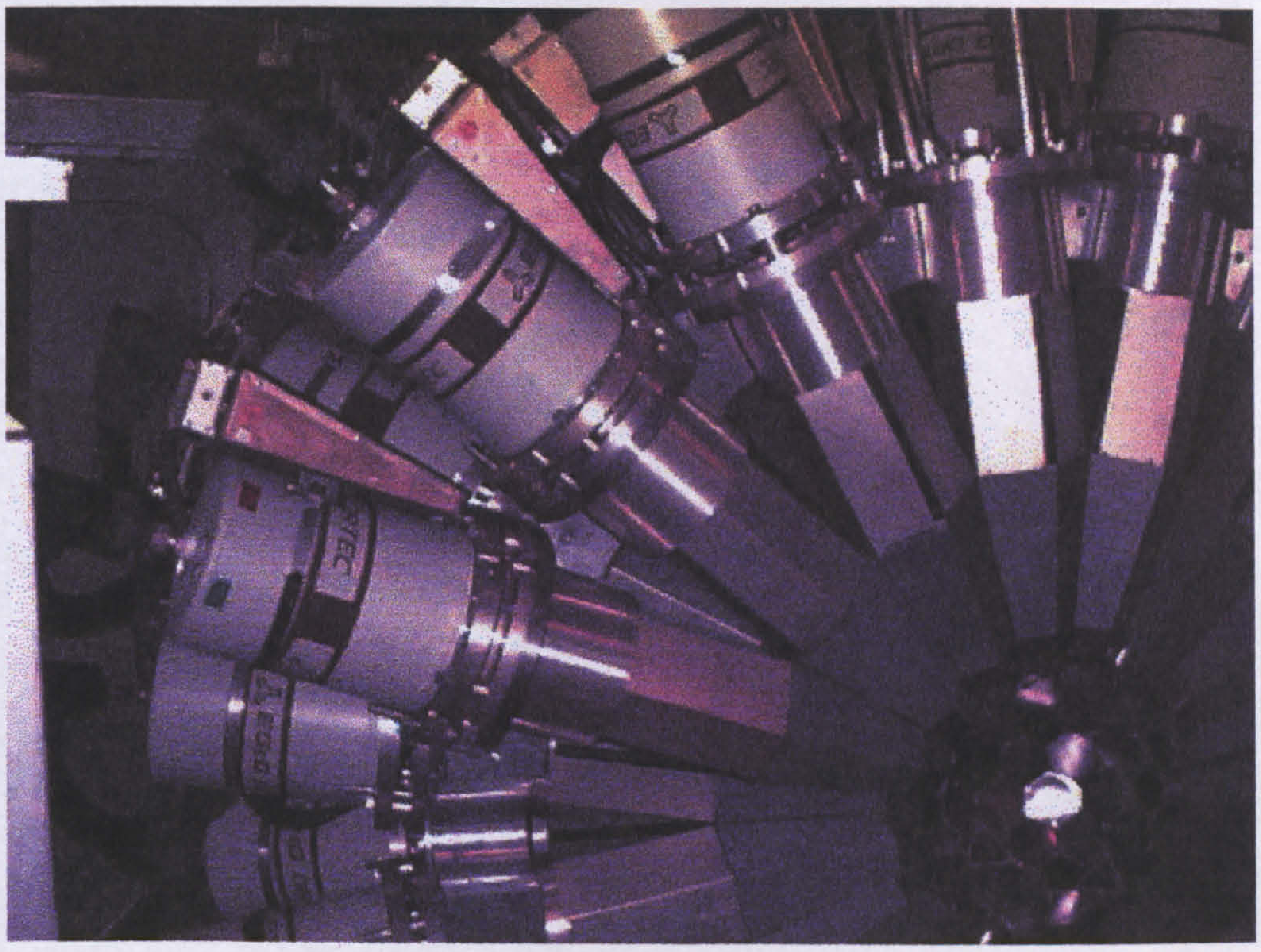

Figure 2.5: A close-up of the GAMMASPHERE array with one quarter of the detectors installed, showing escape-suppressed germanium detectors.

2.4.2 Electronic and Data Acquisition System

The electronics and data acquisition (DAQ) for the GAMMASPHERE array are briefly described in this section; more detailed descriptions can be found in [Lee90].

The GAMMASPHERE DAQ system is based on the VXI (VME eXtended for Instrumentation) standard bus. This standard bus uses electronic cards which contain high-density analogue signal processing and digital circuitry. The VXI crates reduce the amount of cabling and improve the reliability of the electronics. Furthermore, VXI cards host the front-end electronics with highly-integrated electronics cards for the different detectors. One VXI card also hosts a master trigger card; therefore, it is more reliable than those units based on the NIM electronics. Both analogue and digital signals for the two germanium detectors and their fourteen BGO suppression elements can be processed by each VXI card. Additionally, electronic cards contain the master trigger, a histogrammer, an event builder and a data storage interface system.

Further details of the Ge and BGO VXI cards and the data acquisition system for the GAMMASPHERE array are given in [Lee90]. The whole system, connected by fibre-optic links to workstations, is controlled by a master trigger that validates the operation of the VXI cards, where each of the cards has its own local trigger. Each event is transformed into a suitable format for storage and online sorting by the event builder using a software routine. The data are then passed via an optical cable to the tape-server where they are stored on magnetic tape. Furthermore, the data can be written on up to eight magnetic tapes at a rate of up to $\approx$ 4 megabytes/second.

2.4.3 Energy Calibration and Efficiency of the Array

Energy and efficiency calibration were obtained using standard ^{56}Co, ^{60}Co and ^{152}Eu radioactive sources, which emit γ-rays in the energy range $80 < E_\gamma < 3500$ keV. The efficiency curve shown in Figure 2.6 was obtained from the spectra of ^{152}Eu and ^{56,60}Co generated from the sum of all the detectors in the GAMMASPHERE array. The intensity of the transitions was fitted in single (one dimensional 1-D) spectra and normalised with the known relative intensities of the ^{152}Eu and ^{56,60}Co transitions using the EFFIC Oak Ridge computer program.

From Figure 2.6 it can be seen that there is a rapid decrease in the detection efficiency at low energies because of poor penetration into crystal and, therefore, poor charge collection. Additionally, the low-energy events drop rapidly outside the coincident time window because their smaller rise-time means that the electronic processing is less reliable than for those with energies above 200 keV. The relative intensities of the transitions can be obtained by correcting measured peak areas using this efficiency curve.

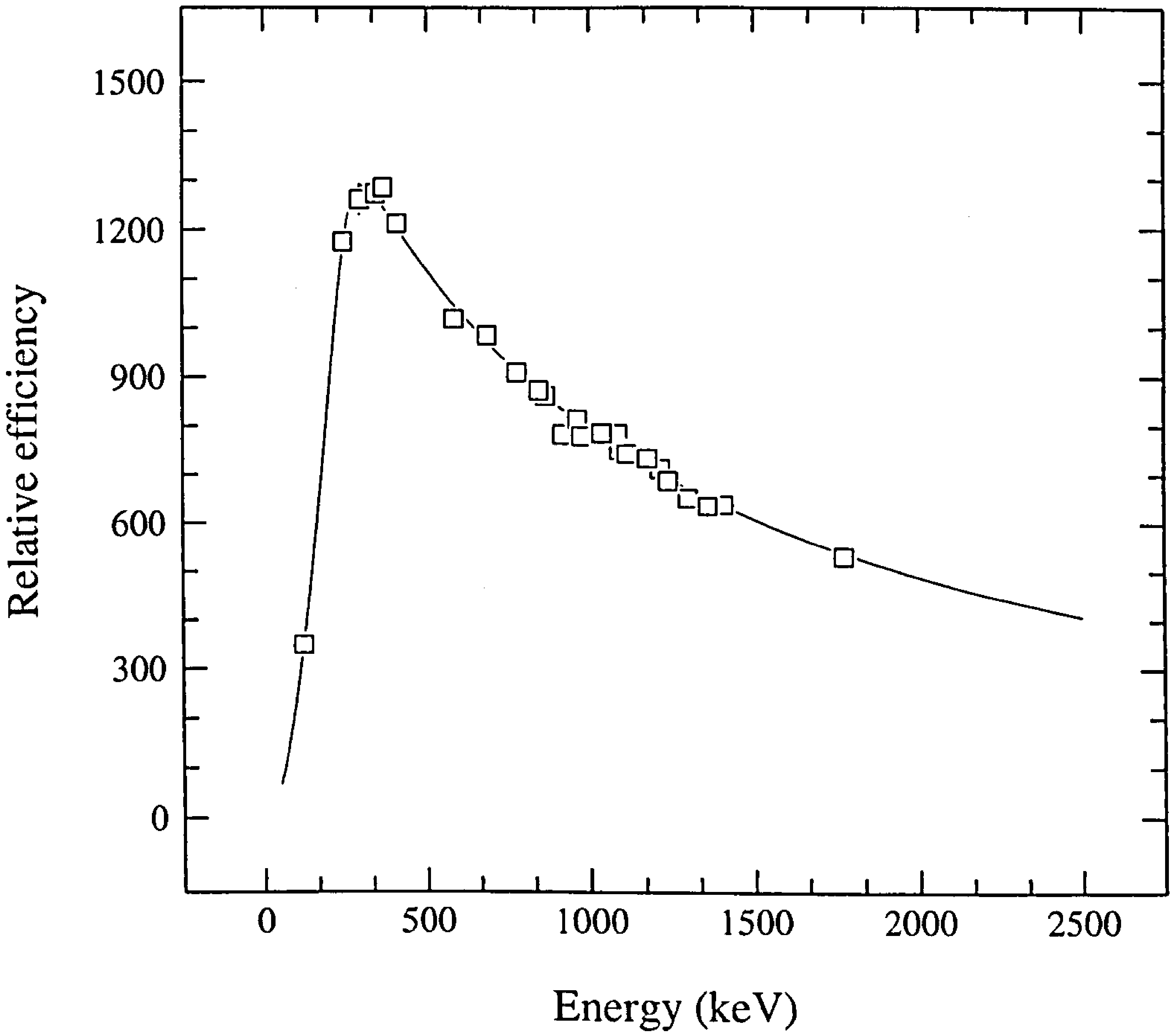

Figure 2.6: The efficiency curve obtained for the GAMMASPHERE array taken with ^{152}Eu and ^{56,60}Co source.

2.5 Data Analysis Methods

The energy, intensity and multipolarity of a γ-ray can be obtained when it interacts with one of the detectors in the array. In order to obtain such measurements, a one-dimensional (1-D) spectrum must be produced. However, this can be achieved in two ways: either directly or indirectly from a two-dimensional (2-D) coincidence "matrix" or a 3-D "cube".

For the purposes of this thesis, the most statistically-significant high-fold coincidences were from a double-gated, triple-gated and quadruple-gated matrix. In order to make use of these data, a series of gated 1-D and 2-D spectra were constructed.

In the 2-D spectrum (matrix) sort, gated matrices are sorted by using double and triple gates with a gate-list (which has lower and upper limits for each transition and consists of 6-20 transitions): for example, in a double-gated matrix, each pair of γ-rays in an event (γ_1, γ_2) is considered in turn and incremented at the position ($E_{\gamma 1}$, $E_{\gamma 2}$) only when there are two other γ-rays in the event which satisfy the gating conditions. Such matrices are analysed by setting gates on one axis of the matrix and projecting out the γ-rays observed in coincidences on the other axis.

In the cube sort, each triple coincidence event (γ_1, γ_2, γ_3) is incremented as a single count at a position ($E_{\gamma 1}$, $E_{\gamma 2}$, $E_{\gamma 3}$). A 1-D spectrum is then extracted by gating on the cube in a two-stage process. Firstly, a gate set on the z-axis projects out a 2-D matrix in the $x - y$ plane and, subsequently, another gate can then be set on the projected matrix to produce a double-gated 1-D spectrum. 3-D analysis has proven to be powerful in discovering the long cascades of γ-rays associated with superdeformed bands. Some of the new superdeformed bands were found using this method, and these will be presented in Chapters 4 and 5.

2.5.1 Angular Correlation Sorting

Although it is possible to deduce information about the multipolarities of the γ-rays by measuring the angular positions of detection with respect to the beam, a complete analysis of angular distributions was not undertaken in this present work. However, the Directional Correlation Orientation (DCO) method [Dr90] was used to compare the γ-rays observed at forward and backward angles and those observed at 90° angles, which is sufficient to distinguish between γ-rays of multipolarity 1 and 2. The multipolarity of the γ-rays (stretched dipole transitions (ΔI =1) or stretched quadrupole transitions (ΔI =2) can be deduced from the ratio shown below:

$$R_{DCO} = \frac{I_\gamma(fb)}{I_\gamma(90^\circ)} \tag{2.5}$$

where $I_\gamma(fb)$ is the intensity of the γ-ray detected with the detectors positioned at forward and backward angles while the $I_\gamma(90^\circ)$ is the intensity of γ-ray detected at angles close to 90°. This ratio depends upon many things, such as the difference in the efficiencies of the different types of detector and the difference in the number of detectors at each angular position. However, this complicated analysis can be avoided by using the known γ-rays of the determined multipolarity of the stretched dipole and the stretched quadrupole transitions for calibrations. For the angles and efficiencies of the detectors in the GAMMASPHERE array, typical values of R_{DCO} for stretched quadrupole transitions and stretched dipole transitions are 1.0 and 0.7 respectively.

Chapter 3

Superdeformation

3.1 Introduction

Superdeformation was first introduced to explain the observation of fission isomers in the actinide nuclei (for example, ^{242}Am) [Po62, St67]. These isomers were associated with a second minimum in the nuclear potential energy surface, due to the shell effects which help to stabilise the deformation. This deformation is also enhanced by electrostatic stress; the former is primarily a result of the Coulomb repulsion due to the abundance of protons. These heavy nuclei were seen to decay from excited states with abnormally short half-lives of spontaneous fission from nuclear ground states; however, this half-life is longer compared to the half-life of spontaneous fission from excited states. These fission isomers have very short fission decay lifetimes because the second minimum has a thinner potential barrier (which means increased tunnelling probability); this can be seen in Figure 3.1. However, further calculations [Be75] showed that superdeformed (SD) shapes can occur at high angular momentum in lighter nuclei.

The first experimental evidence for superdeformation was found in $^{152}_{66}$Dy$_{86}$ [Ny84]. This arose from the analysis of the γ-ray continuum in an $E_\gamma - E_\gamma$ correlation matrix where "ridges" were observed. It was suggested that these ridges resulted from SD states and came from moment of inertia measurements. The first discrete line

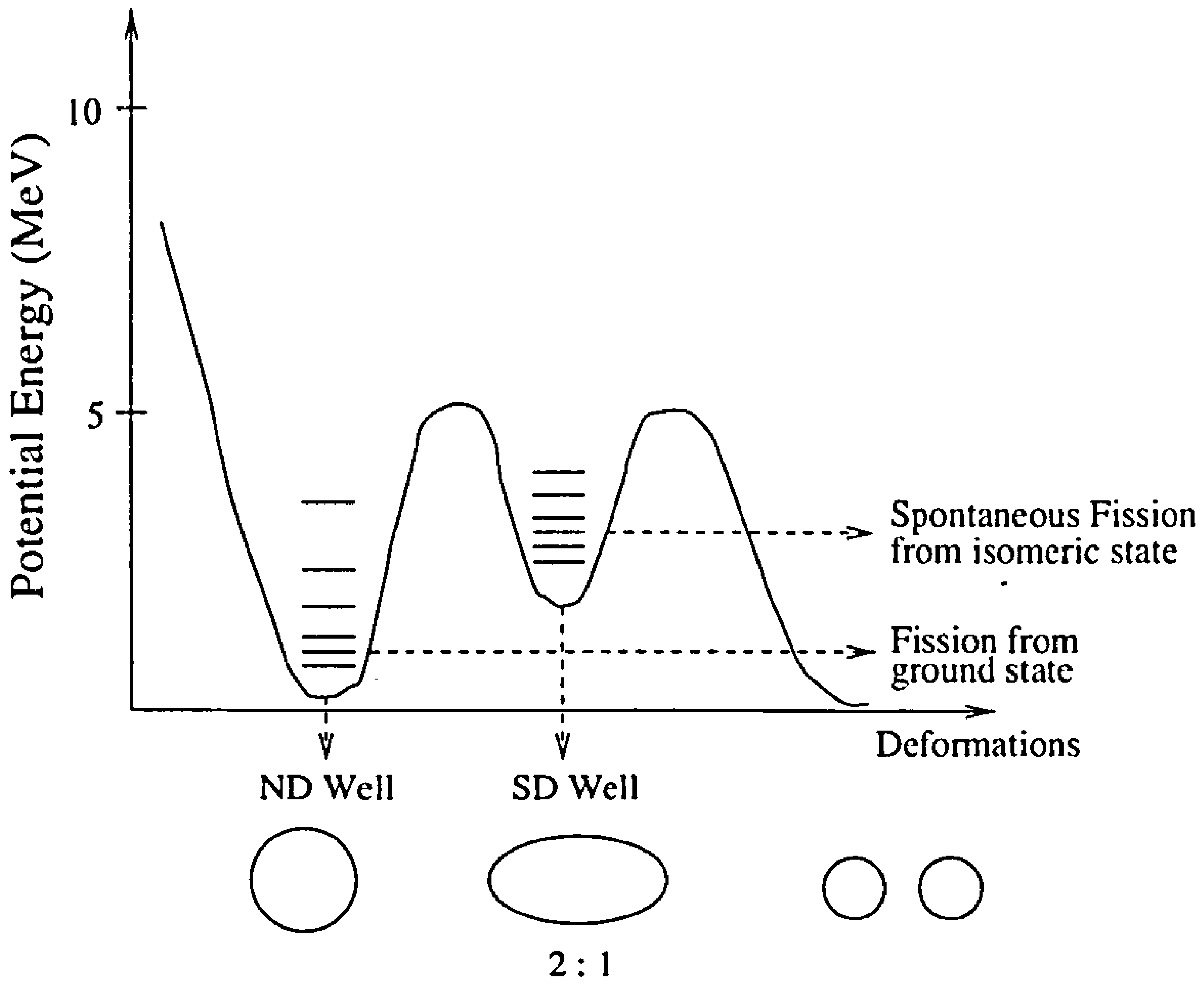

Figure 3.1: A schematic illustration of the behaviour of the potential energy as a function of deformation to show fission from ground state and isomeric state.

spectrum of an SD band was discovered in $^{152}_{66}Dy_{86}$ by Twin *et al.*, in 1986 [Tw86] occurring in a nucleus with an axis ratio of 2:1:1 (abbreviated to 2:1). At about the same time, evidence for a highly deformed nucleus (with an axis ratio of 3:2) was found in $^{132}_{58}Ce_{74}$ by Nolan *et al.*, [No85]. To date there are five regions of the Segré chart in which superdeformation has been discovered : these are the mass A $\approx$ 80 region (nuclei close to $^{82}_{38}Sr_{44}$ [Sm95]), the A $\approx$ 130 region (nuclei close to $^{132}_{58}Ce_{74}$ [No85]), the A $\approx$ 150 region (nuclei close to $^{152}_{66}Dy_{86}$ [Tw86]) and the A $\approx$ 190 region (nuclei close to $^{192}_{80}Hg_{112}$ [JK91]). Recently an SD structure has been observed in $^{62}_{30}Zn_{32}$ [Mac97]. For this study, the SD region of interest is the A $\approx$ 150 mass region and in particular the nucleus $^{150}_{64}Gd_{86}$.

3.2 Superdeformation in the A $\approx$ 150 Region

Calculations were performed for most nuclei in the Segré chart [Ra80, Be81, DN85] and it was found that one of the best cases for observing an SD structure lay in the region of N = 80-86 and Z = 64-66. These predictions were determined from analysis of the calculated nuclear potential energy surfaces, where a strong minimum was observed at $\beta_2 \approx 0.62$. A detailed description of how this procedure was performed is explained in [DN85]. A lifetime measurement of the rotational structure in ^{152}Dy [Ben87] confirmed the SD nature of the band, with a quadrupole moment of $Q_\circ$ = 19±3 eb indicating an axis ratio of 2:1 in agreement with the theoretical predictions.

To date, SD bands have been identified in 21 nuclei [Si96] in this region of the Segré chart. Furthermore, the discovery of SD bands in $^{154}_{68}\text{Er}_{86}$ [Ber95] and $^{153}_{67}\text{Ho}_{86}$ [Ap97] have pushed the borders of superdeformation in this region to higher proton numbers and into the next intruder shell (N = 7).

3.3 Properties of Superdeformed Bands

An SD band is characterised by a sequence of highly-collective E2 transitions with a constant energy separation. The yrast SD band is formed by the occupation of all energy levels below the nuclear Fermi surface. Thus, this band is the most strongly-populated SD structure. In the A ≈ 150 mass region, every nucleus exhibits at least one excited SD band (except the $^{154}_{68}\text{Er}_{86}$ nucleus, which has only one observed SD band). Some of the properties of mass 150 SD bands are outlined below:

1. In-band γ-ray energy separation (Δ E$_\gamma$) is regular and between ≈ 40 and 60 keV.
2. The γ-ray transitions range from ≈ 550 to 1700 keV.
3. The magnitude of the $\mathcal{J}^{(2)}$ moment of inertia lies in the range ≈ 75 to 90 MeV/$\hbar^2$.
4. The population intensities of the bands are very small, being between ≈ 0.04% and 2% of the total fusion-evaporation cross-section for the production of the nucleus. In the A ≈ 130 region, this value can be up to 5%.

5. Excited SD bands are built on particle-hole excitations close to the nuclear Fermi surface.

6. The first excited SD band carries ≈ 30-50 % intensity relative to the yrast band in $Z < 66$ nuclei. However, there is one exception for the nucleus ^{152}Dy, where the excited bands carry 4-9 % intensity relative to the yrast band because the nucleons have to be excited across the large shell gaps.

7. The relative in-band intensity profile for this mass region has three distinct parts (see Figure 3.2): first, the de-population region (A), where the intensity of the SD band is lost by three or four transitions (lowest energy γ-ray) into the normal-deformed (ND) states; secondly, the plateau region (B), where no distinguishable feeding or decay-out occurs; thirdly, the feeding region (C), where the band is populated from continuum transitions (high energy γ-ray) until it reaches a limit where the band has a 100 % intensity.

8. It is estimated that the SD states lie approximately 3-5 MeV above the ND states. There have been no discrete links observed between the SD states and the ND states in this mass region. However, links have been observed between the SD states and the ND states in neodymium isotopes (^{133,135,137}Nd) [Baz94, Del95, Lu95], ^{134}Nd [Pe96] and ^{143}Eu [At93]. Similar links have been observed in ^{194}Hg [Kh96].

High-N Orbital Assignments:

The spectroscopic properties of SD bands in different nuclei can be characterised by the number of occupied high-N intruder orbitals. In the A ≈ 150 region, these orbitals arise from the $N = 6$ proton states (originating from the $i_{13/2}$ sub-shell) and the $N = 7$ neutron states (originating from the $j_{15/2}$ sub-shell) [Tw90]. The occupation of specific high-N intruder orbitals can have dramatic effects which result in contributions of varying magnitude to the $\mathcal{J}^{(2)}$ [Be88]. The Gd isotopes are one of

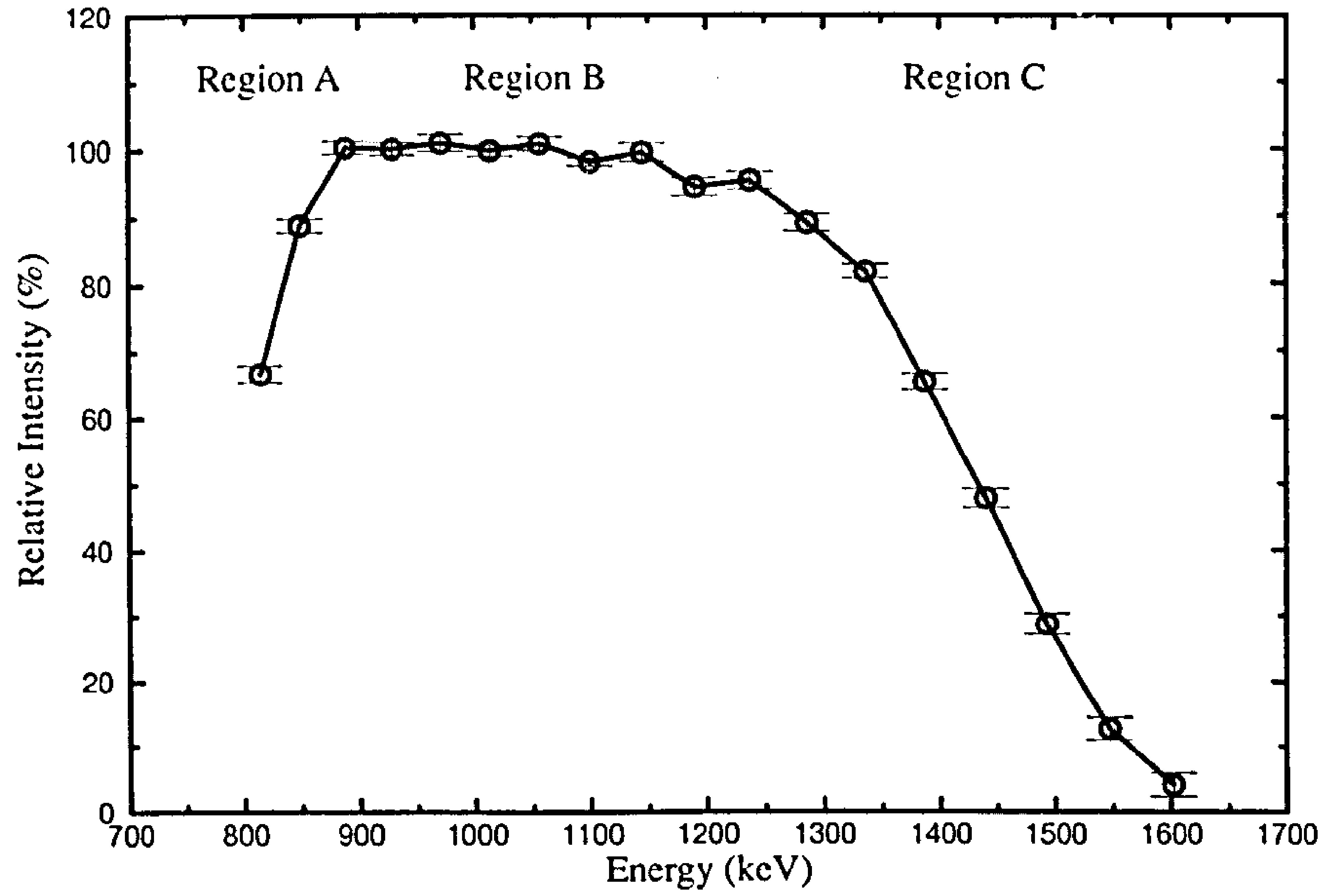

Figure 3.2: The relative in-band intensity of the yrast SD band in ^{150}Gd , normalised to the average intensity in the plateau region (B). This figure illustrates the de-population region (A), plateau region (B) and feeding region (C) (see text).

the best examples to show shape-effects and pairing correlations in this mass region. These effects in Gd isotopes will be discussed later in Chapters 4 and 5. As a general conclusion, the variations of $\mathcal{J}^{(2)}$ with rotational frequency, ω, show that the few nucleons in high-N orbitals play an important role in all SD bands in this mass region. Hence, the configuration assignment of the SD bands involves single-particle states $\pi 6^p \nu 7^n$, where p and n represent the number of protons and neutrons in the N = 6 and N = 7 intruder orbitals respectively.

Identical SD Bands:

After the discovery of multiple SD bands within a single nucleus ^{153}Dy [Joh89], it became possible to investigate further the microscopic structure of both single-particle states close to the nuclear Fermi surface in the second potential well. It was observed that SD bands in one nucleus (e.g. mass A) could sometimes have similar properties (e.g. $\mathcal{J}^{(2)}$) to the SD band in a neighbouring nucleus (e.g. mass A + 1). The first reported case of the pair of identical SD bands was in the ^{150}Gd and ^{151}Tb nuclei [By90]. The first excited SD bands in these nuclei were identical to the yrast bands in their Z+1 neighbours to within 2 keV. The similar $\mathcal{J}^{(2)}$ moments of inertia can be understood if the identical bands have the same high-N configurations. When the particle-hole excitation in the excited SD partner takes place from low-N to a high-N orbital, (in the case of the ^{150}Gd -^{151}Tb pair) the particle was excited from the low-N orbital ([301]1/2$^-$) into a strongly-curving orbital ([651]3/2$^+$). The [301]1/2$^-$ orbital is flat and, thus, a hole-state occupying such a level had little effect on the moment of inertia $\mathcal{J}^{(2)}$.

Further examples of identical SD bands observed in this mass region are discussed in Ref. [Bak95]. A pair of SD bands with similar transition energies were observed at the $\frac{1}{4}$, $\frac{1}{2}$ and $\frac{3}{4}$ energy points of the partner bands. By using high efficient γ-ray arrays (EUROBALL and GAMMASPHERE), more identical SD bands were discovered, some of which were to be found in Gd isotopes. This will be discussed in Chapters 4 and 5.

3.4 Previous Studies of ^{150}Gd & ^{151}Gd

Bengtsson *et al.*, suggested that the $\mathcal{J}^{(2)}$ moments of inertia for ^{150}Gd and ^{151}Tb would vary as a function of rotational frequency [Be88]. This prediction is in strong agreement with the discovery of the SD bands in these nuclei [Fa89], and with variations in the $\mathcal{J}^{(2)}$ moments of inertia. Further experimental work by Byrski *et al.*, [By90] showed that excited SD bands exist in ^{150}Gd and in ^{151}Tb. It was found that the properties of these SD bands closely resembled those of the yrast SD bands in their neighbouring nuclei. From those studies, it appears that the first excited band in ^{150}Gd is identical to the yrast SD band of ^{151}Tb, and that the first excited band of ^{151}Tb is identical to the yrast SD band of ^{152}Dy. These SD bands were interpreted from proton particle-hole excitations as lying between low-N [301]1/2$^-$ orbital and the high-N [651]3/2$^+$ intruder orbital. The yrast SD band in ^{150}Gd has been assigned the $\pi6^2\nu7^2$ intruder configuration where the lowest two N = 6 proton and N = 7 neutron orbitals are occupied [Fa89].

Six SD bands have been previously reported in ^{150}Gd , using data from the EUROGAM γ-ray spectrometer [Cl95]. SD bands 2 and 4 interact due to the near-degeneracy of the two levels. Even though crosstalk was observed between these two bands, the inter-band linking transitions could not be identified [Bea93]. However, analysis for the present study has confirmed the crosstalk between the two bands and also identified the linking transitions. Further information will be given in Chapter 4.

One of the SD bands, namely, band 5, exhibits a pronounced discontinuity (back-bending) in the γ-ray transition energies [Fa94], which is interpreted as the band crossing. It was suggested that this band decays primarily into band 1 at the band crossing, but no linking transitions were observed. However, sufficient statistics in the present work have enabled these linking transitions between the two bands to be observed. This is the first observation of linking transitions between the two SD bands in the A $\approx$ 150 region and further details will be discussed in Chapter 4.

The quadrupole moments and deformations were measured for six SD bands in ^{150}Gd [Bea98], and it was found that deformation drives both the high-N intruder and low-N natural parity states.

There has been no SD study for ^{151}Gd to date; hence, no SD structures have been found in this nucleus. Six SD bands were observed and assigned to ^{151}Gd for the first time in this nucleus from this work. The results will be presented in Chapter 5.

3.5 Motivation for the study of ^{150}Gd & ^{151}Gd

The overiding objective of this study is to investigate and understand in more detail the decay mechanism of SD bands in the 150 mass region. The other aims are outlined as:

1. To search for SD linking transitions and thereby to establish the spins and excitation energies of SD bands in ^{150}Gd.
2. To study the ND to SD decays and to permit an understanding of the nature of collective excitations in the second minimum.
3. To discover further examples of excited SD structures.

3.6 The Experiment

An experiment was performed at the Lawrence Berkeley National Laboratory (LBL) using the GAMMASPHERE γ-ray spectrometer [Lee90] to populate high-spin states in ^{150}Gd. The reaction used was ^{130}Te(^{26}Mg, 6n)^{150}Gd with a beam energy of 149 MeV provided by the 88-Inch Cyclotron accelerator. The target consisted of two tellurium foils of 500 μg cm^{-2} thickness on a 500 μg cm^{-2} layer of gold with a thin layer of aluminium between the tellurium and gold to prevent any migration of tellurium. To compensate for varying detector gains, the data were gain-matched online to fully-stopped peaks in ^{150}Gd. During the experiment, an unsuppressed Ge fold > 5 was required before accepting an event, and the event-rate was $\sim$ 5000 events per second. Under these conditions, a total of 1.4×10^9 events was accumulated.

Chapter 4

Superdeformed bands in ^{150}Gd

Investigation of New Superdeformed Bands

The ratio of population intensities was obtained by measuring the intensity flow through the ground-state transitions in their respective level schemes in a Radware Cube[Rad95]. The relative intensities of ^{149,150,151}Gd are 16%, 66%, and 18% respectively, within an uncertainty of ± 5 % on each figure.

An automatic search routine was employed to search for rotational structures with an γ-ray energy separation appropriate to superdeformation in the mass 150 region (45 - 60 keV).

4.1 Results

4.1.1 New Superdeformed bands in ^{150}Gd

Analysis has revealed fourteen rotational γ-ray cascades with properties consistent with superderformed shapes. Six bands have been assigned to ^{151}Gd and will be discussed in Chapter 5; the remaining eight bands have been assigned to ^{150}Gd and are presented in this chapter. The bands have been assigned to particular isotopes in view of their relationships with the low-spin transitions of ^{150,151}Gd. Furthermore, the close relationships between transition energies of the new bands with those in neighbouring nuclei has been used to suggest configurations.

On the basis of the observation of new SD bands and their measured relative intensities, the convention for labelling has been amended according to Table 4.5.

Old Scheme	New Scheme
Band 1	Band 1
Band 2	Band 3
Band 3	Band 4b
Band 4	Band 4a
Band 5	Band 2
Band 6	Band 5

Table 4.1: Reclassification of known SD bands in ^{150}Gd .

The spectra of the six previously-known SD bands [Cl95] and the eight new SD bands observed during the progress of this work are presented in Figures 4.1, 4.2, 4.3, 4.4 and 4.5. These spectra are generated from a 1-D spectrum sort using a gate-list for each individual SD band. During the sort, 4 gates had to be satisfied before the remaining γ-rays in the event were incremented into the spectrum (quintuples) (as described in Section 2.5). Furthermore, a double-gated spectrum was subtracted from the quadruple-gated spectrum in order to avoid contamination and produce clean spectra of the SD bands.

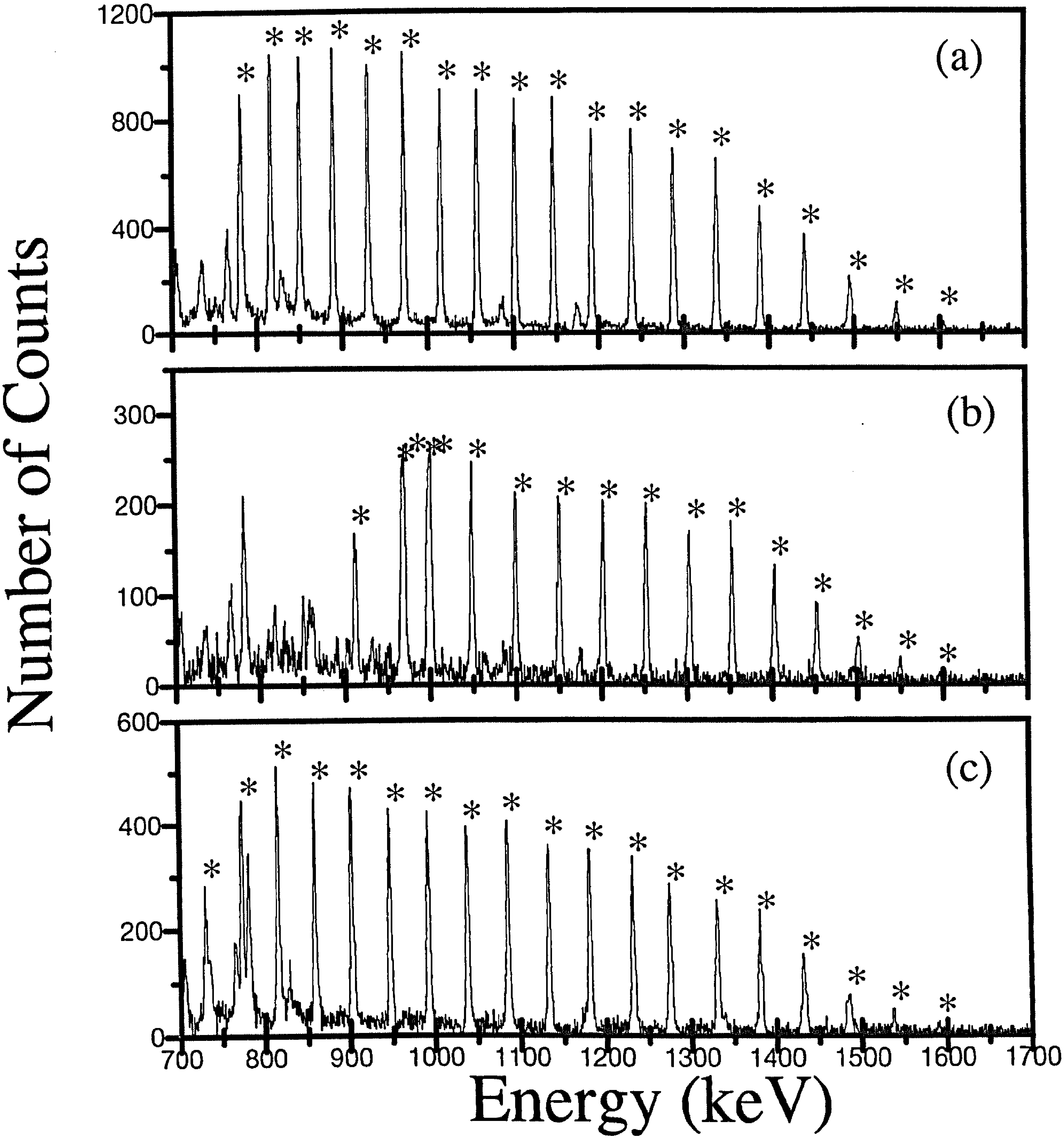

Figure 4.1: Background subtracted quadruple-gated spectra of band 1 (a), band 2 (b), band 3 (c) in ^{150}Gd.

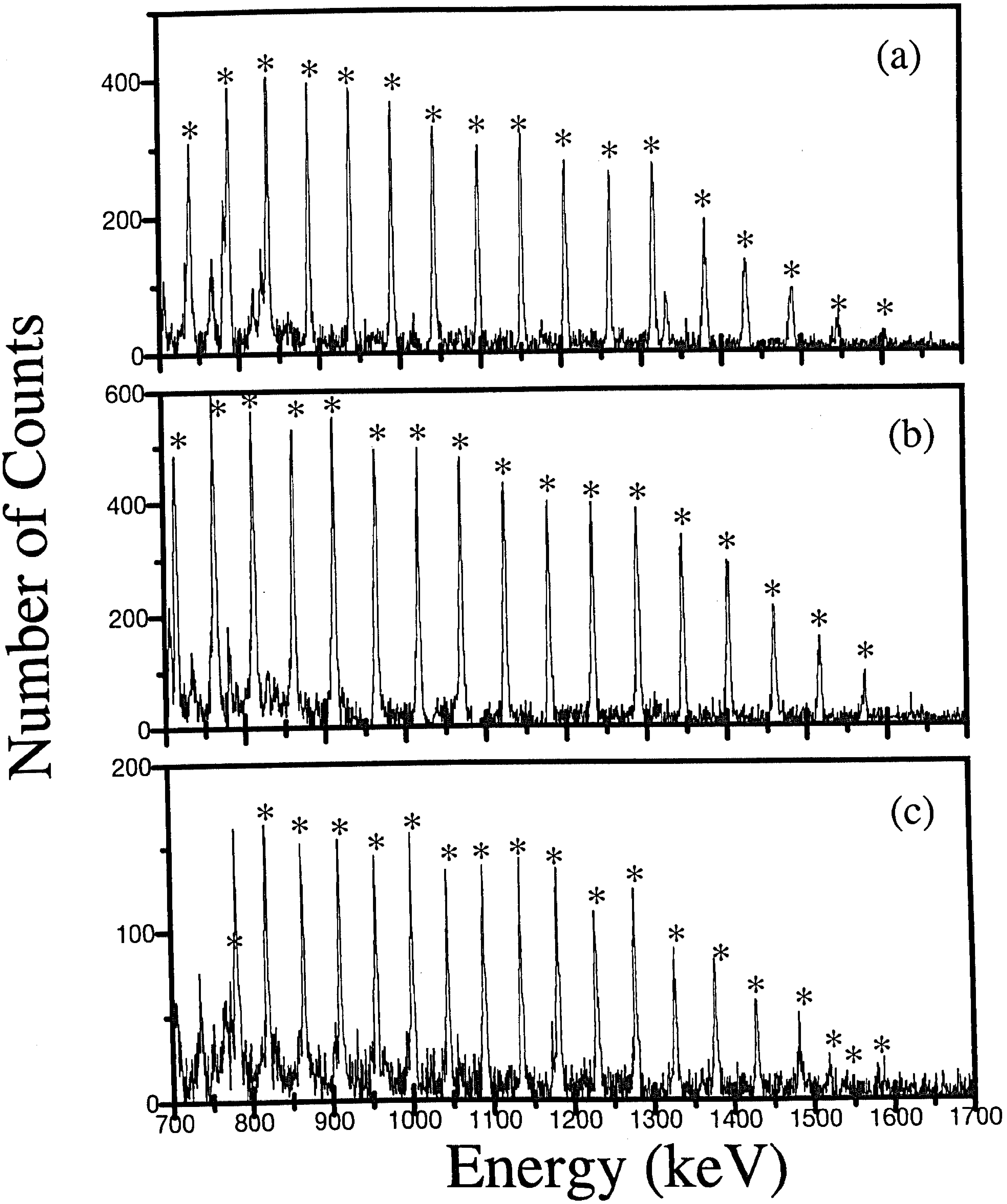

Figure 4.2: Background subtracted quadruple-gated spectra of band 4a (a), band 4b (b), band 5 (c)in ^{150}Gd.

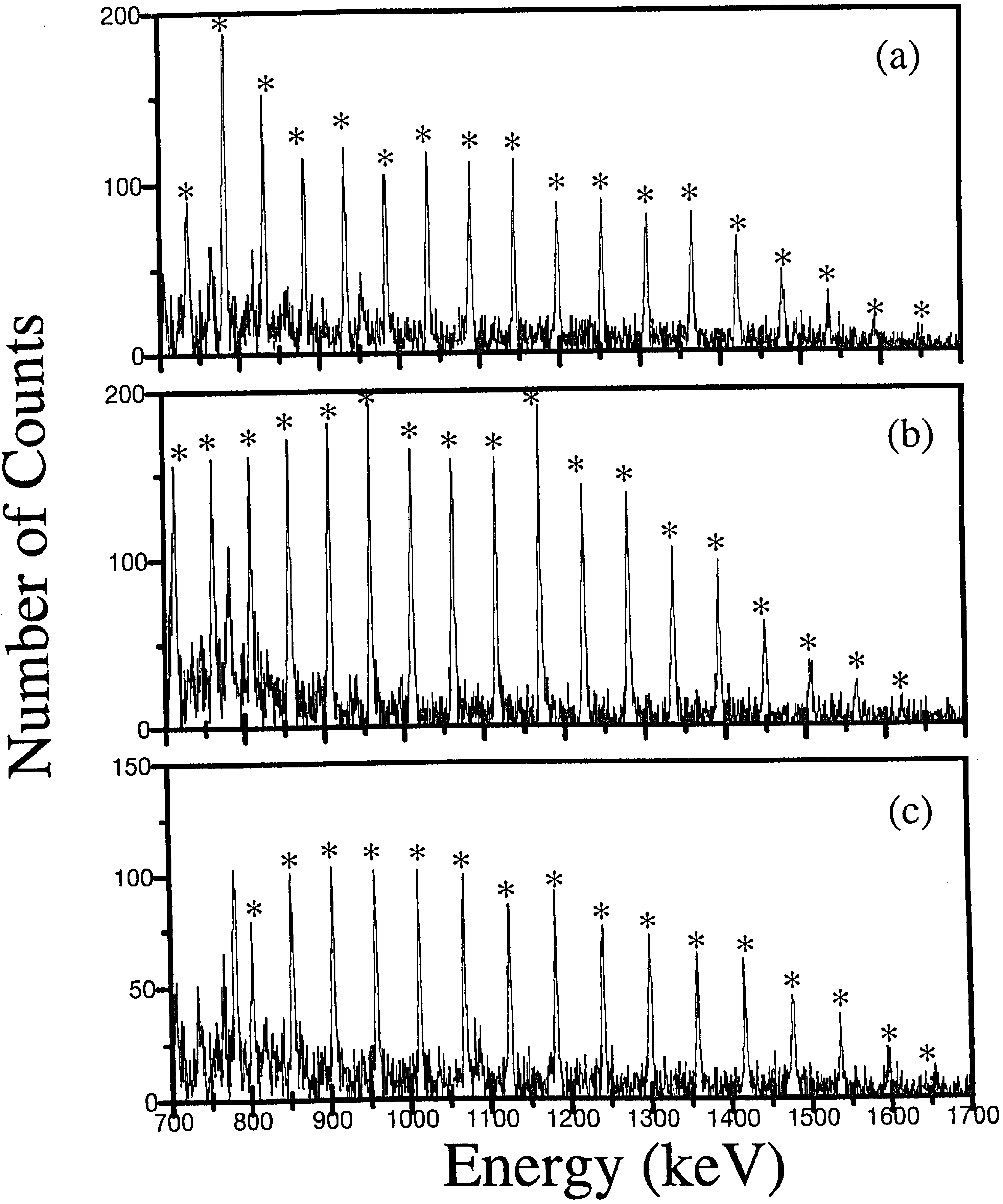

Figure 4.3: Background subtracted quadruple-gated spectra of band 6a (a), band 6b (b), band 7 (c)in ^{150}Gd.

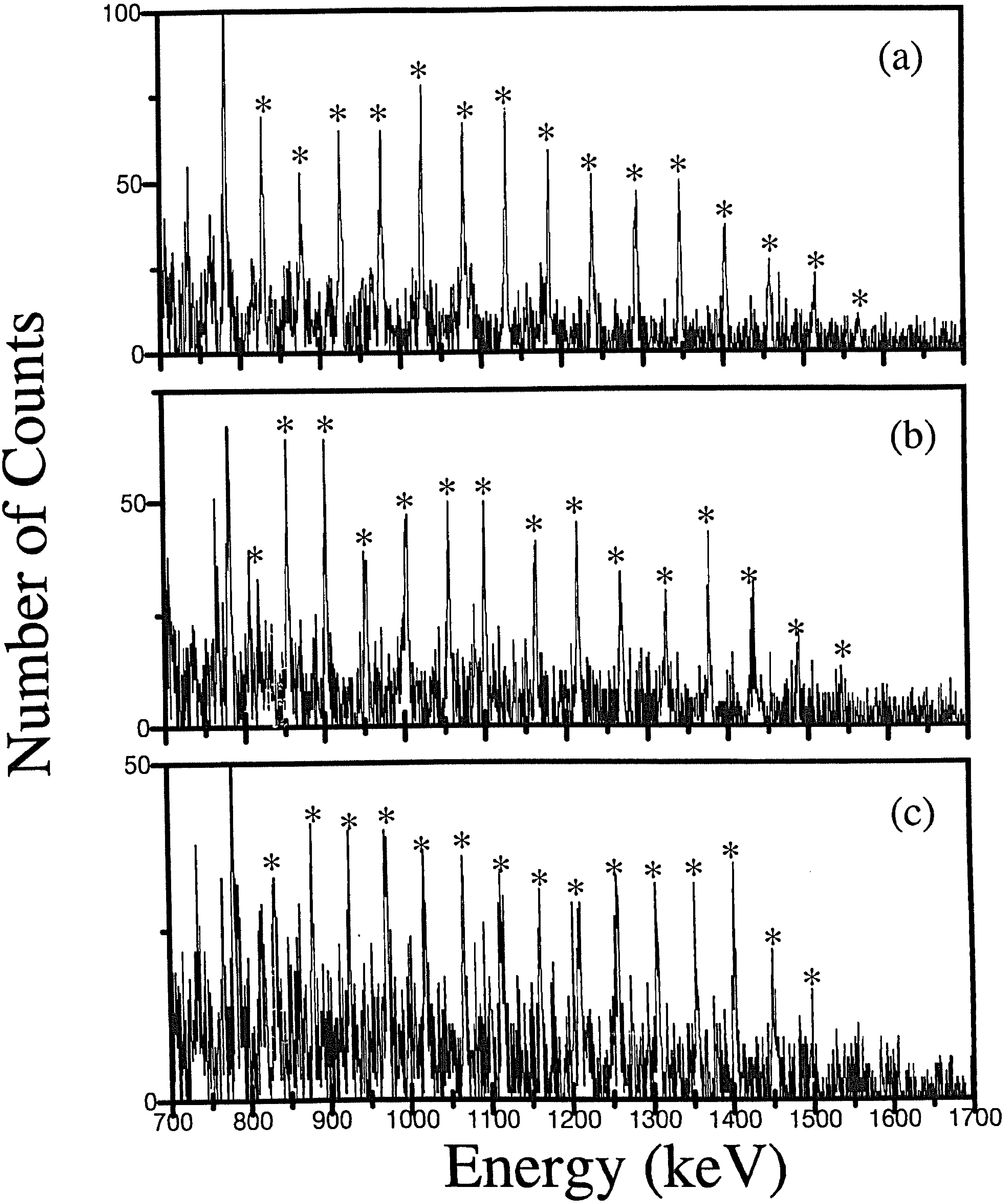

Figure 4.4: Background subtracted quadruple-gated spectra of band 8a (a), band 8b (b), band 9 (c) in ^{150}Gd.

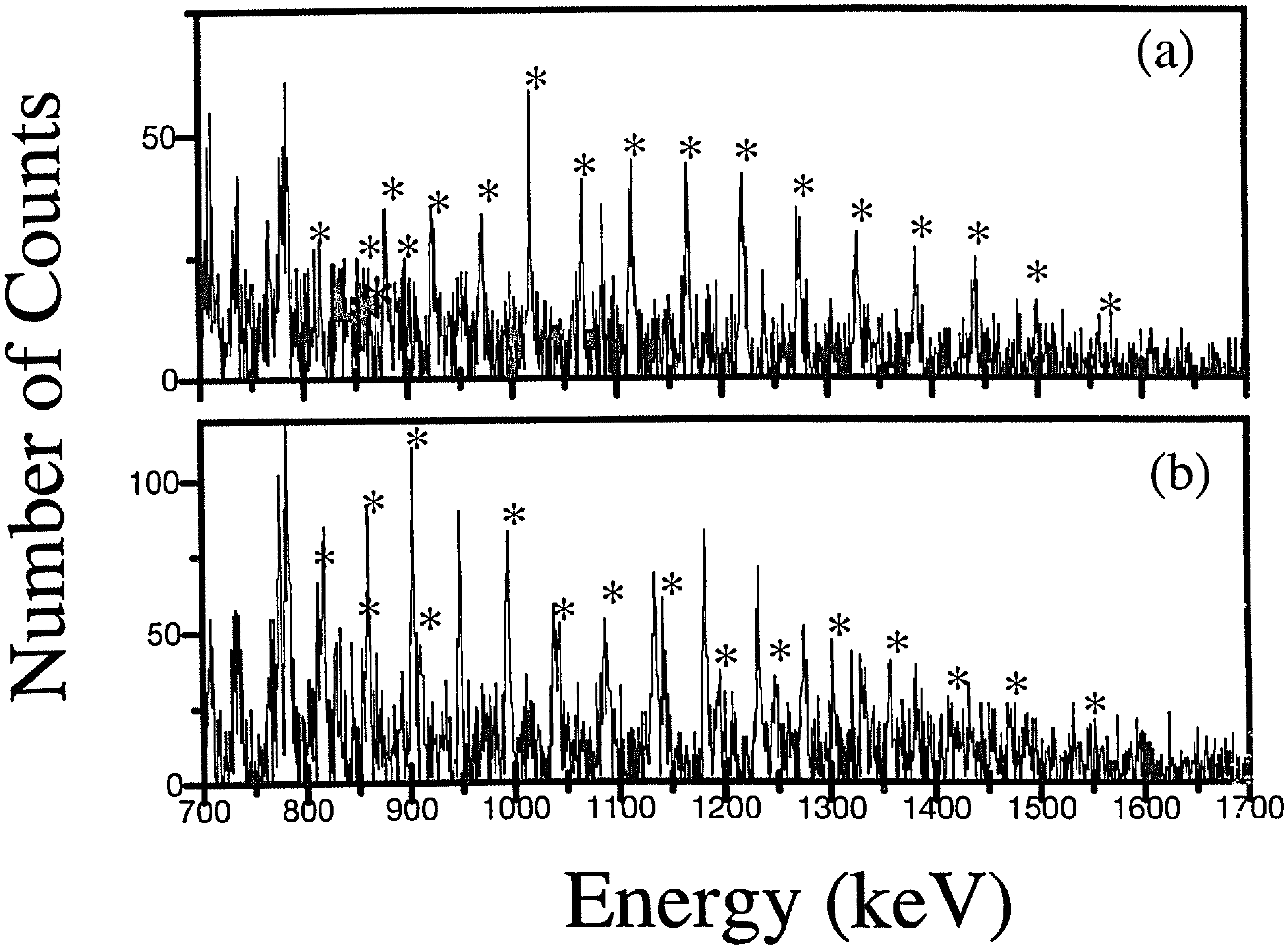

Figure 4.5: Background subtracted quadruple-gated spectra of band 10a (a), band 10b (b) in ^{150}Gd.

4.1.2 Transition Energies and Relative Intensity

The transition energies were measured using the peak-fitting routine in the analysis software Scana [Ur92] and GF2 [Rad95]. Uncertainties were extracted for the energies of each transition based on the individual statistical and calibration contributions. For very clean uncontaminated spectra, such as that of band 1, the uncertainties are typically 0.1 keV or less, although this value does increase with increasing γ-ray energy due to the effects of Doppler broadening and the efficiency of the array. The uncertainties are greater for those transitions which exhibit some degree of contamination, especially those in the weakly-populated SD bands. Tables 4.2, Table 4.3 and Table 4.4 contain the transition energies and associated errors of the fourteen SD bands in ^{150}Gd.

The statistics obtained in the present experiment have allowed four of the six previously-known SD structures in ^{150}Gd to be extended to both lower and higher energies.

1. One new transition at an energy of 1601.7 keV has been observed in band 1.
2. Band 2 has a new γ-ray transition at an energy of 1595.9, 1645.5 keV.
3. Band 4a has a new transition at an energy of 1658.4 keV.
4. Band 5 has four new transitions: one at the lower energy end of the band (771.6 keV) and three at higher-energy (1516.7 keV, 1536.0 keV, 1589.9 keV, the latter suggesting a backbend taking place at the top of band 5).
5. Two previously-identified transitions (618.0 keV, 665 keV) in band 4b [Bea93] were identified as members of the low-lying transitions of ^{149}Gd, and were not observed in coincidence with the remaining band members. They are, therefore, not members of band 4b.

Eight new SD structures have been observed in ^{150}Gd and furthermore, analysis has revealed linking transitions between several SD bands:

1. Linking transitions have been observed between bands 1 and 2 and between bands 3 and 4a. These will be dealt with in Section 4.3 and Section 4.4 respectively. This is the first observation of such linking transitions in the A $\approx$ 150 region.
2. Two of the new bands (namely, band 10a and band 10b) show a discontinuity (backbend) at lower energies. Further studies are required to investigate and understand this behaviour in these bands.

Transition Energies (keV)					
B1	B2	B3	B4a	B4b	B5
815.0(1)	910.2(2)	727.9(2)	688.1(3)	712.5(3)	771.6(4)
849.1(1)	966.1(3)	771.5(2)	735.8(4)	761.2(3)	817.1(3)
887.9(1)	995.6(3)	814.3(2)	785.2(5)	810.5(3)	862.9(2)
928.9(1)	968.6(3)	857.3(5)	834.4(3)	860.0(3)	908.4(2)
970.9(1)	999.0(2)	900.7(2)	885.3(3)	910.6(4)	953.2(2)
1013.5(1)	1046.8(2)	945.3(2)	936.6(4)	962.5(4)	998.3(2)
1056.5(1)	1097.6(2)	990.6(2)	988.6(2)	1014.9(3)	1042.4(3)
1100.1(1)	1148.7(2)	1036.7(2)	1040.9(2)	1068.2(2)	1087.7(4)
1144.6(1)	1199.9(2)	1083.3(2)	1095.3(2)	1122.4(3)	1133.1(2)
1190.5(1)	1250.9(2)	1131.4(3)	1149.3(2)	1177.1(3)	1179.4(2)
1237.9(1)	1301.2(2)	1179.3(2)	1203.9(2)	1232.2(3)	1227.1(4)
1286.6(1)	1351.6(2)	1229.8(2)	1259.3(2)	1287.7(3)	1275.1(2)
1336.6(1)	1401.0(2)	1273.4(2)	1313.7(2)	1343.8(3)	1325.2(3)
1387.8(1)	1450.4(2)	1328.6(2)	1377.3(2)	1400.5(3)	1375.1(3)
1440.1(1)	1499.1(3)	1378.6(2)	1428.3(2)	1457.1(3)	1426.1(3)
1493.1(2)	1547.6(4)	1430.3(2)	1486.4(3)	1513.9(3)	1480.1(3)
1547.0(3)	1595.9(7)	1482.2(3)	1543.2(4)	1569.1(3)	1516.7(4)
1601.7(4)	1645.5(9)	1535.4(4)	1600.1(6)		1536.0(4)
		1587.8(7)	1658.4(6)		1589.9(8)

Table 4.2: Transition energies of SD bands 1-5 in ^{150}Gd obtained from this work.

Transition Energies (keV)				
B6a	B6b	B7	B8a	B8b
733.2(2)	711.2(5)	800.6(4)	827.8(5)	804.1(4)
778.2(2)	758.5(7)	850.0(3)	875.4(4)	851.7(4)
829.9(2)	806.4(2)	902.4(2)	924.4(3)	900.2(3)
879.8(2)	855.6(2)	955.3(3)	974.4(4)	951.3(4)
930.2(2)	905.4(2)	1010.2(2)	1025.1(3)	1001.5(3)
981.4(2)	956.4(2)	1066.2(2)	1076.9(4)	1053.8(4)
1033.9(2)	1008.2(2)	1122.2(2)	1128.9(4)	1098.1(3)
1087.0(2)	1060.8(2)	1179.8(2)	1182.5(5)	1161.8(3)
1141.4(2)	1113.9(2)	1238.0(3)	1236.1(4)	1212.4(3)
1195.6(3)	1168.4(2)	1296.6(3)	1290.1(4)	1265.9(5)
1250.9(2)	1222.6(2)	1355.7(3)	1345.0(4)	1320.6(5)
1306.5(2)	1278.0(2)	1415.0(3)	1400.1(5)	1375.6(5)
1362.7(3)	1333.7(2)	1474.0(4)	1455.9(6)	1430.7(8)
1419.0(3)	1390.2(3)	1534.0(5)	1511.8(7)	1485.4(9)
1475.3(4)	1446.8(3)	1594.1(7)	1567.3(9)	1538.9(9)
1532.3(6)	1503.9(4)	1652.5(9)		
1589.9(7)	1560.7(6)			
1644.7(9)	1617.9(8)			

Table 4.3: Transition energies of SD bands 6-8 in ^{150}Gd obtained from this work.

Transition Energies (keV)		
B9	B10a	B10b
830.1(5)	815.1(7)	808.9(5)
876.6(4)	849.1(4)	858.6(7)
922.6(5)	889.1(8)	909.8(8)
970.0(3)	877.7(6)	856.5(8)
1016.6(4)	922.7(5)	900.7(5)
1064.3(4)	969.4(5)	945.7(5)
1112.0(5)	1015.6(5)	991.6(5)
1160.0(7)	1065.4(6)	1040.3(8)
1207.7(6)	1112.5(6)	1093.0(9)
1254.4(5)	1165.9(7)	1140.3(5)
1302.7(5)	1218.8(6)	1192.0(5)
1351.7(5)	1271.4(6)	1244.9(6)
1400.1(5)	1326.9(5)	1299.1(6)
1448.9(5)	1382.4(7)	1354.8(8)
1495.0(9)	1438.4(6)	1411.4(6)
	1496.1(8)	1468.6(8)
	1556.6(9)	1530.8(8)
		1592.1(9)

Table 4.4: Transition energies of SD bands 9-10 in ^{150}Gd obtained from this work.

Relative Intensity Measurements

Relative intensity measurements reflect the intensity of a rotational band relative to the band with the maximum intensity. Such measurements were performed by setting clean (uncontaminated) gates (typically 7 - 12 gates) on each SD band, then measuring the peak area of an individual γ-ray in the band. After gate adjustments, these areas were corrected for efficiency using an efficiency curve (Figure 2.6) which was produced for this experiment.

The relative intensity profiles of SD bands are often characterised by three major regions: the feeding region, the plateau region, and the de-population region (Section 3.3). The relative intensity distributions for the SD bands in ^{150}Gd are illustrated in Figures 4.6 and 4.7. These plots have been normalised to the plateau region, which is defined as carrying 100% of the total intensity of the band.

The main features of the relative intensity diagrams are:

1. The feeding region starts at 1200 keV and extends to $\approx$ 1600 keV for the previously-known SD bands (typically 5 - 7 transitions). In band 9, the feeding starts at 1400 keV.

2. A plateau region extends to $\approx$ 850 keV in bands 3, 4a, 4b, 5, 6a, 9 and $\approx$ 900 keV in bands 1, 6b, 7, 8a, 8b, 10a, 10b, and an anomalously-high energy range of $1100 \leq E_\gamma \leq 1250$ keV in band 2.

3. De-excitation over several transitions in bands 1, 3, 4a, 4b, 5, 6b, 7, 8a, 10b, or very fast decay-out in just one or two transitions in bands 6a, 8b, 9, 10a. The decay-out intensity observed for band 2 confirms the backbending assignment.

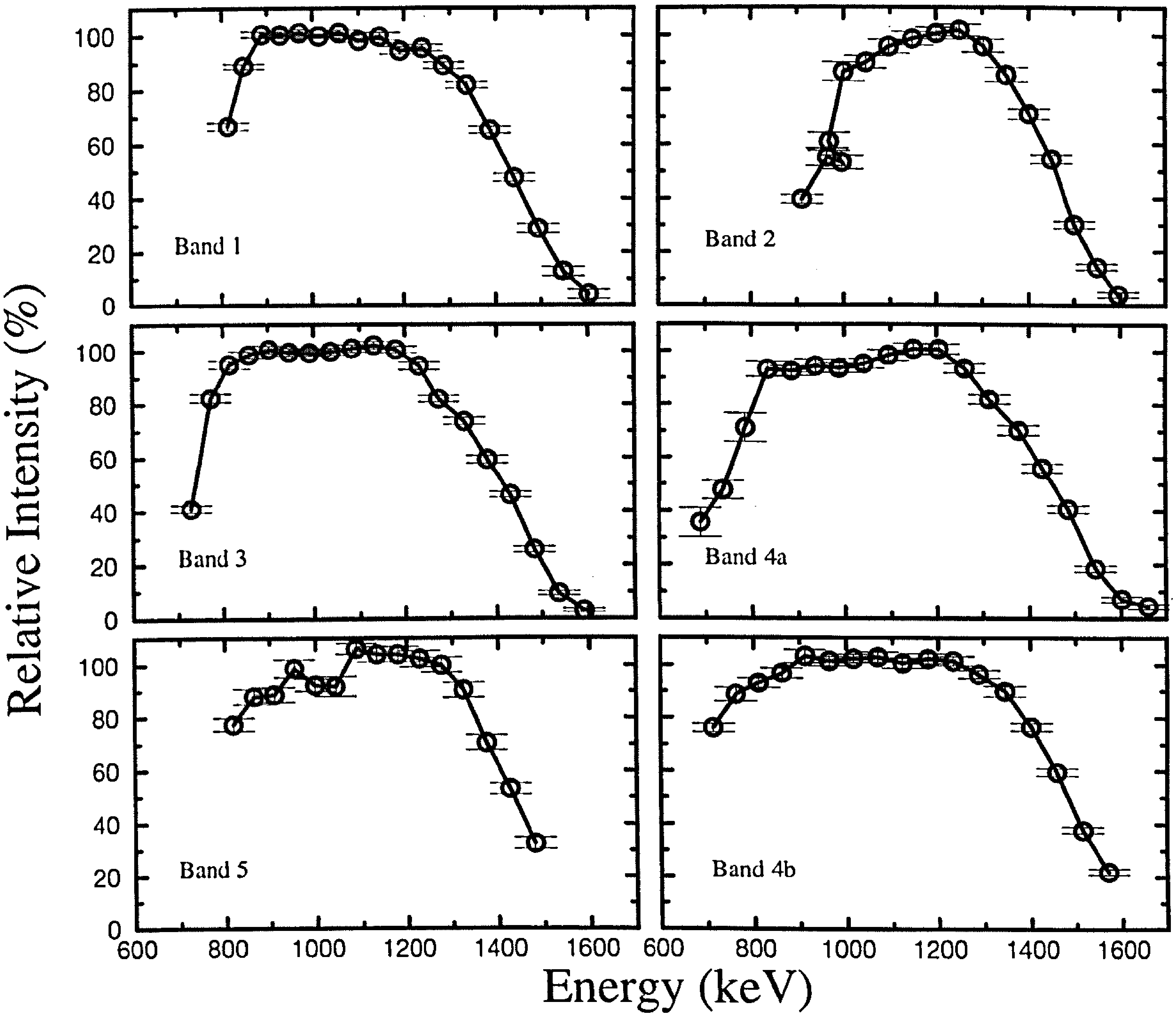

Figure 4.6: The relative intensity measurements for band 1, band 2, band 3, band 4a, band 4b and band 5 in ^{150}Gd. They have been normalised to the average intensity of the plateau region.

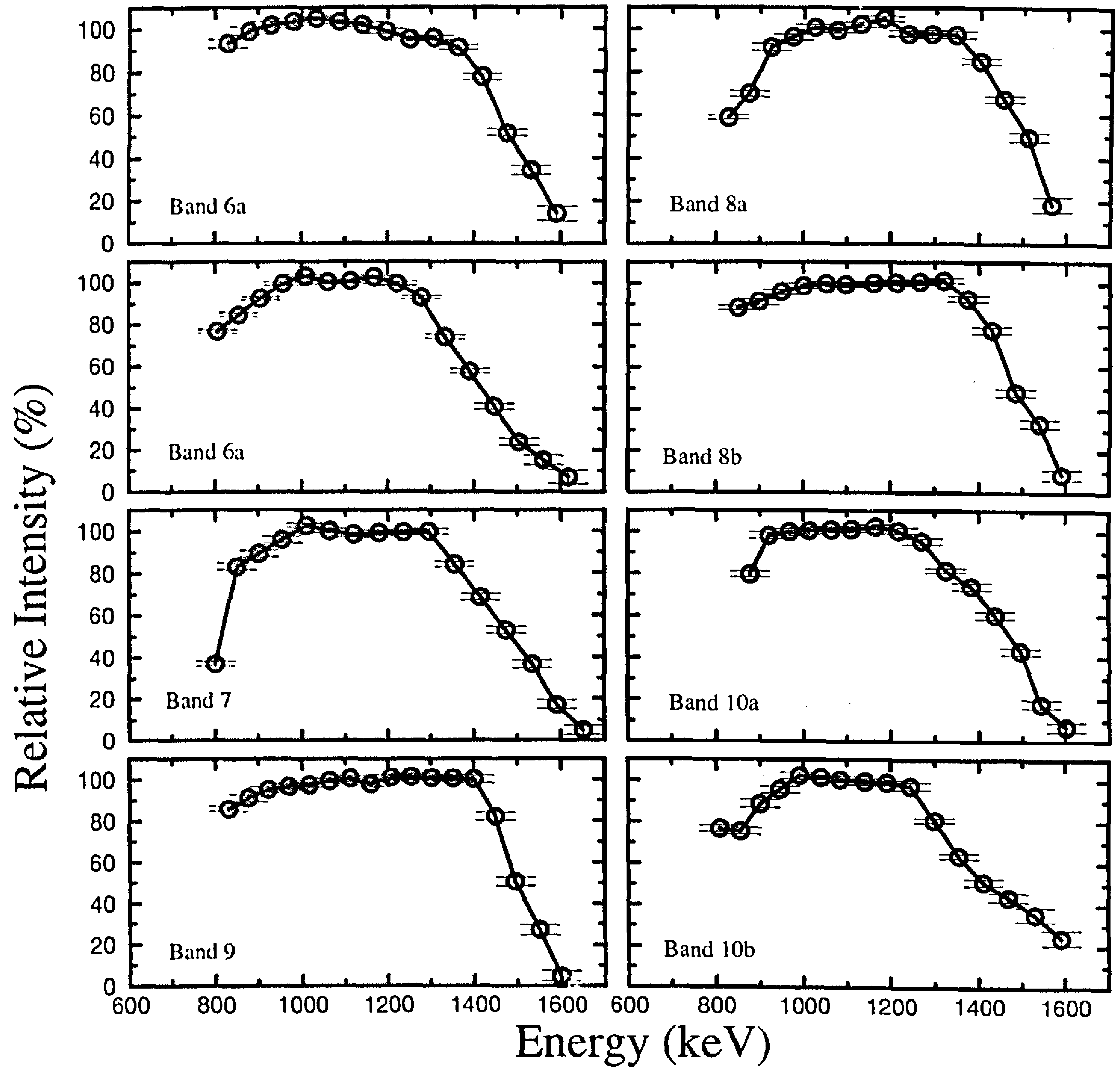

Figure 4.7: The relative intensity measurements for band 6a, band 6b, band 7, band 8a, band 8b, band 9, band 10a and band 10b in ^{150}Gd. They have been normalised to the average intensity of the plateau region

The intensities of the excited SD bands relative to band 1 were also measured using similar gating conditions. For this, six gates were set in the plateau region of each SD band, thus allowing a direct comparison of the intensity of 100% transitions in each excited SD band with that of band 1. The results are listed in Table 4.5 as a percentage relative to band 1 (100%).

SD Bands	Intensity (%) Relative to Band 1
Band 1	100
Band 2	47 ± 3
Band 3	45 ± 3
Band 4b	42 ± 4
Band 4a	44 ± 3
Band 5	30 ± 3
Band 6a	19 ± 2
Band 6b	19 ± 2
Band 7	18 ± 2
Band 8a	10 ± 2
Band 8b	8 ± 2
Band 9	6 ± 1
Band 10a	6 ± 1
Band 10b	6 ± 1

Table 4.5: The intensities of the SD bands (1-10) in ^{150}Gd relative to yrast SD in ^{150}Gd.

4.1.3 Spin Assignments

As no γ-ray linking transitions have been observed between the SD and the ND states in ^{150}Gd, the spins and parities of the observed SD bands cannot be assigned unambiguously. This being the case, it is possible to assign spins to the observed SD bands based on transition-energy relationships; the method will be outlined below. With the observation of linking transitions between SD bands 1 and 2, and bands 3 and 4a (which is presented in Section 4.3 and 4.4), the spin assignments of these bands relative to each other have been established unambiguously.

The spin assignment of band 1 was obtained [Fa89a] from relative intensity measurements of the SD to ND transitions. From this, a value for the average entry-spin to the ND yrast state was deduced. It was calculated [Cl95] that the de-excitation of SD band 1 occurred at an excitation energy of 3 – 4 MeV above the ND yrast state and that the spin-gap was $\approx 3\ \hbar$. On the basis of this information, the lowest transition in band 1 (815.0 keV) is assigned to link levels of spin $32^+ \rightarrow 30^+$ with an error of $\pm\ 2\ \hbar$. The parity of the band is derived from its orbital configuration.

A detailed systematic approach to determine the nuclear-level spins of SD bands has been outlined by Ragnarsson [Ra93] and Stephens [Ste90]: The Ragnarsson method involves calculations of the relative (or effective) alignments between SD bands as described in Section 1.3.3. The first step in this process is to make certain assumptions about the relative spins of SD bands, based on the premise that there is indeed a relationship between transition energy and spin.

Many SD rotational bands in different nuclei have been found to have identical (or equivalent i.e., identical averages of) transition energies within one or two keV, which was much more similar than predicted. This behaviour can be characterised as an alignment effect where the alignment is quantized in units of 1/2 or 1 $\hbar$. This alignment effect is shown in Figure 4.8.(a). There are five possible spin-values between I and I + 2, which are indicated on the ordinate in Figure 4.8.(a). The solid sloping line represents a spin versus energy plot for even-mass nuclei while the broken line is for odd-mass nuclei. The separation between the γ-ray energies in the even-even

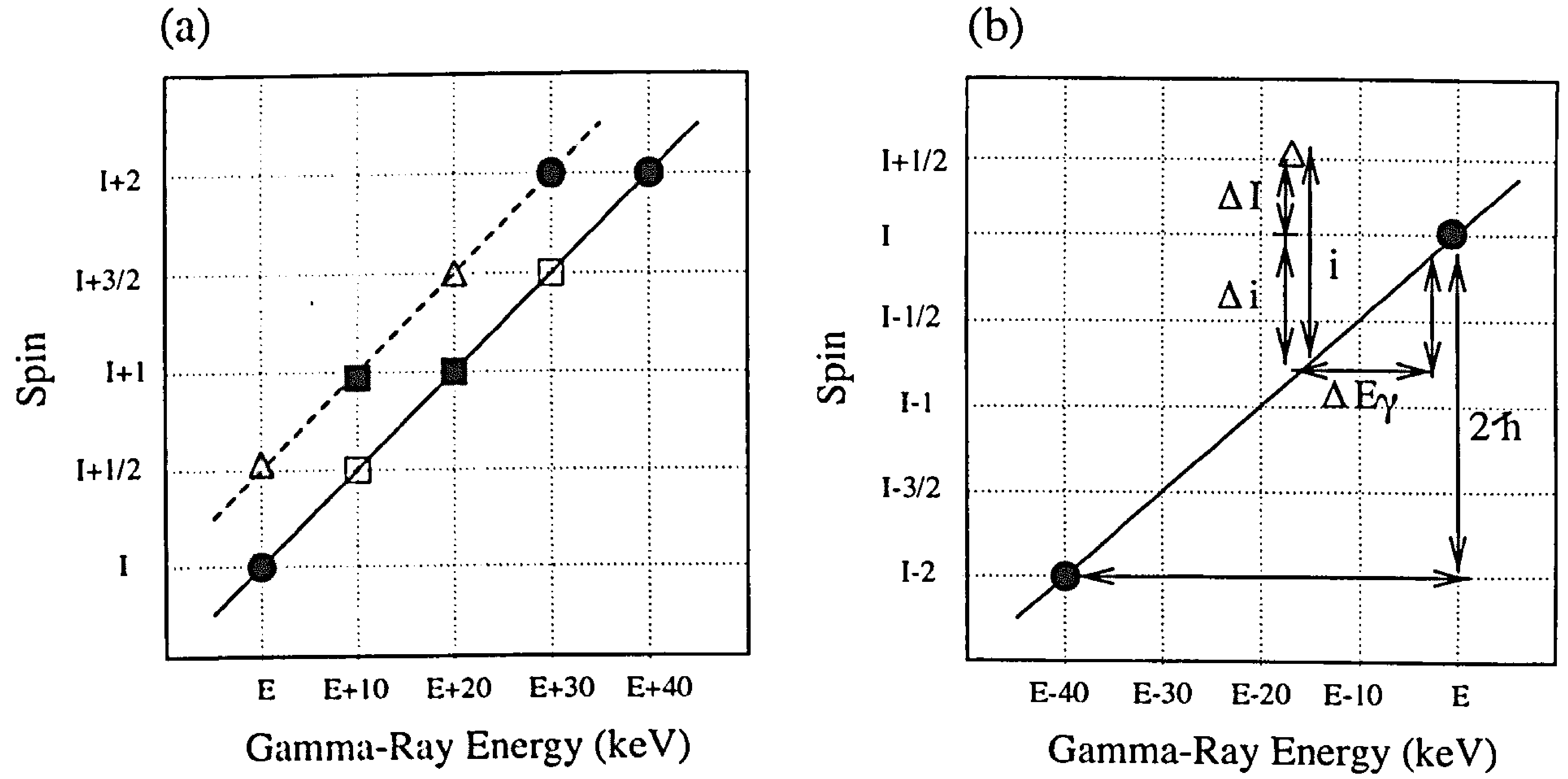

Figure 4.8: (a) the relationship between spin and γ-ray energy for two different alignments, (b) a diagram to show the alignment, i, and the incremental alignment, Δi.

system (I and I + 2) is taken to be 40 keV, as is typical for SD bands. In this example, the two lines have the same slope, they have the same dynamic moment of inertia and thus, the same separation between γ-ray energies. In this case, a band in the odd-mass neighbour with identical energies (triangle symbols) has an alignment of $1/2\ \hbar$ or $3/2\ \hbar$ relative to the reference band. For half-way point energies (empty squares), the alignment is $0\ \hbar$ or $1\ \hbar$. This is typical behaviour of rotational bands in many SD nuclei.

The alignments are determined by the method illustrated in Figure 4.8.(b). A "new" band can be considered in an odd-mass nucleus. One transition from the latter is indicated by a triangle. Its alignment relative to a band selected as a reference in an even-even nucleus is indicated by circles on a solid line. The alignment can be obtained by comparing those transitions that are closest in energy between the new band and the reference band. The alignment consists of two parts: the real difference in spin between the two emitting states ΔI, and the incremental alignment Δi that represents the spin difference associated with the difference in γ-ray energy. ΔE_γ

represents the energy differences between the transitions in the new band and the reference band. The difference in γ-ray energy between the closest transitions in the reference band is represented as $\Delta E_{\gamma}^{\circ}$, which is associated with a spin change of $2\hbar$. From this, the incremental alignment Δi is defined as:

$$\Delta i = \frac{2\Delta E_{\gamma}}{\Delta E_{\gamma}^{\circ}} \tag{4.1}$$

As can be seen from the above equation, the incremental alignment does not require any knowledge of the spins.

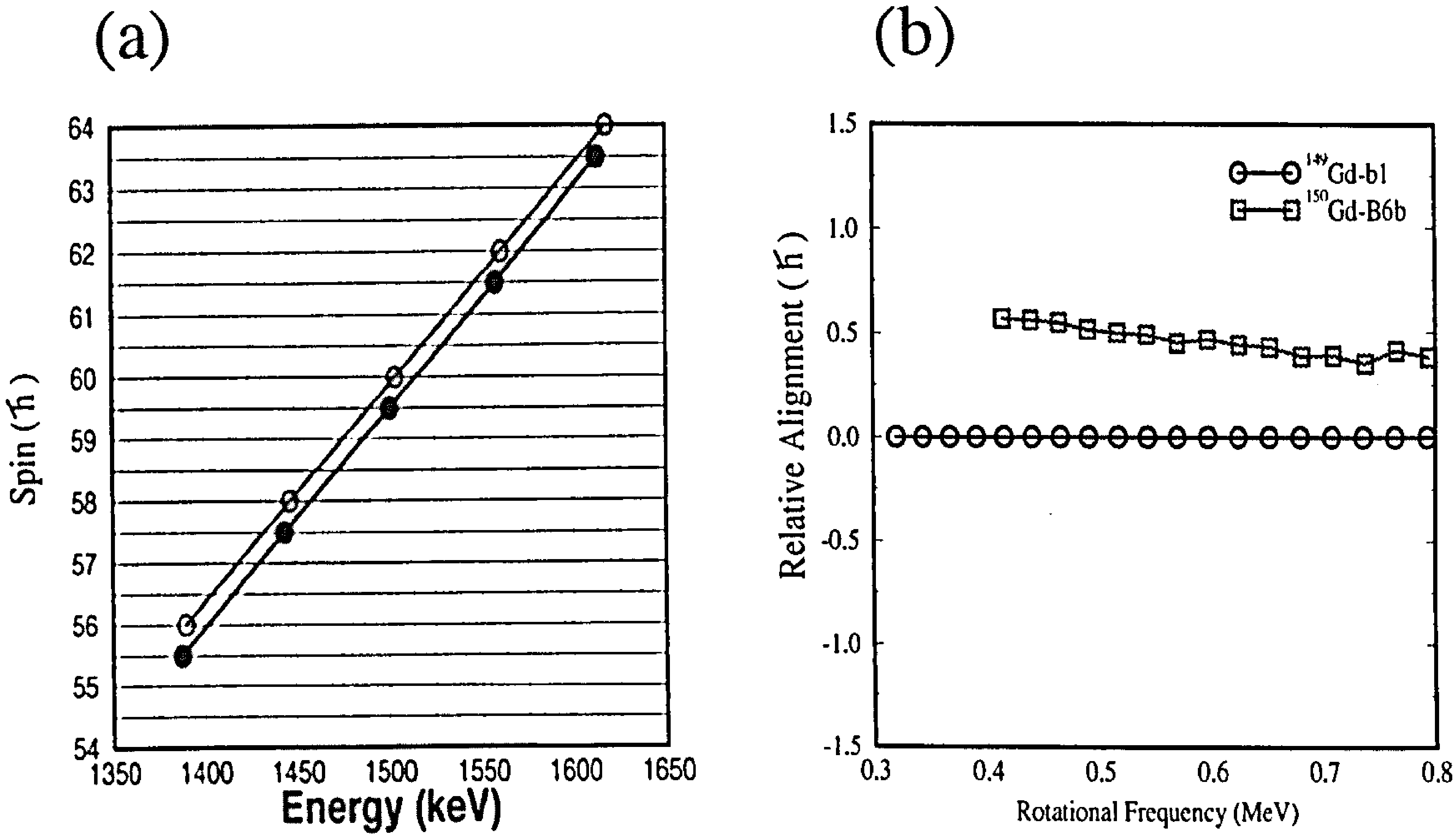

Figure 4.9: (a) the relative alignment for band 6b was plotted relative to the reference band 1 in ^{149}Gd, (b) the relationship between spin and γ-ray energy for two different alignments (e.g filled circles represents the yrast band in ^{149}Gd and empty circles represents the band 6b in ^{150}Gd).

Figure 4.9.(a) shows an example of how this method was used to determine the spins for band 6b in ^{150}Gd. The sloping lines represent spin versus energy plots and shows possibilities for an even-even (band 6b with empty circles) and an even-odd

(yrast band 1 in ^{149}Gd with filled circles) nucleus with identical relationship between γ-rays. An example of relative alignment calculation is shown in Figure 4.9.(b) for SD band 6b in ^{150}Gd relative to the yrast SD band in ^{149}Gd. It is seen that there is only a $\Delta i = 0.5\ \hbar$ alignment between these bands. From this relative alignment, an assumption as to the spins of band 6b can be made due to the similarities in their γ-ray energies.

The spin assignments for all the new SD bands in ^{150}Gd have been obtained using this method.

The reference band was chosen based on the similarities in $\mathcal{J}^{(2)}$. The identification of the linking transitions between bands 1 and 2 and their assignment as stretched E2 transitions gives $\Delta I = 2$ between bands 1 and 2. Since band 1 is the ground-state band and the nucleus is even-even, the spins are, therefore, expected to be even, and this will require the band 2 to be even also. This assignment is based on the similarities of the γ-ray energies between band 2 and the yrast SD band of ^{152}Dy. However, the spin assignments are $2\hbar$ lower than is currently assumed [Ra93] for the yrast SD band in ^{152}Dy. The level schemes of previously-known and newly-observed SD bands in ^{150}Gd are shown in Figure 4.10 and Figure 4.11.

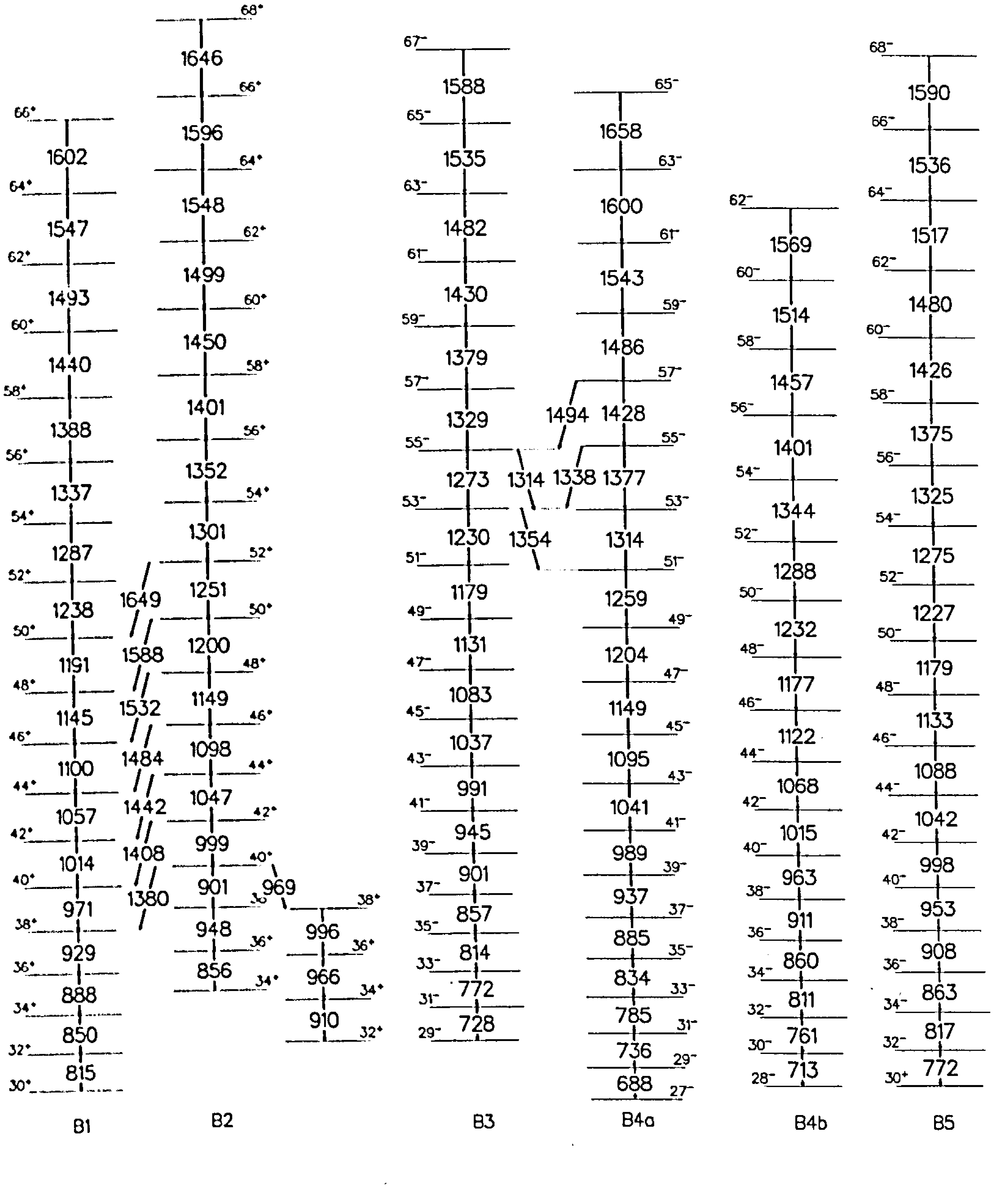

Figure 4.10: The partial level scheme of SD bands 1-5 in ^{150}Gd with their spin-values.

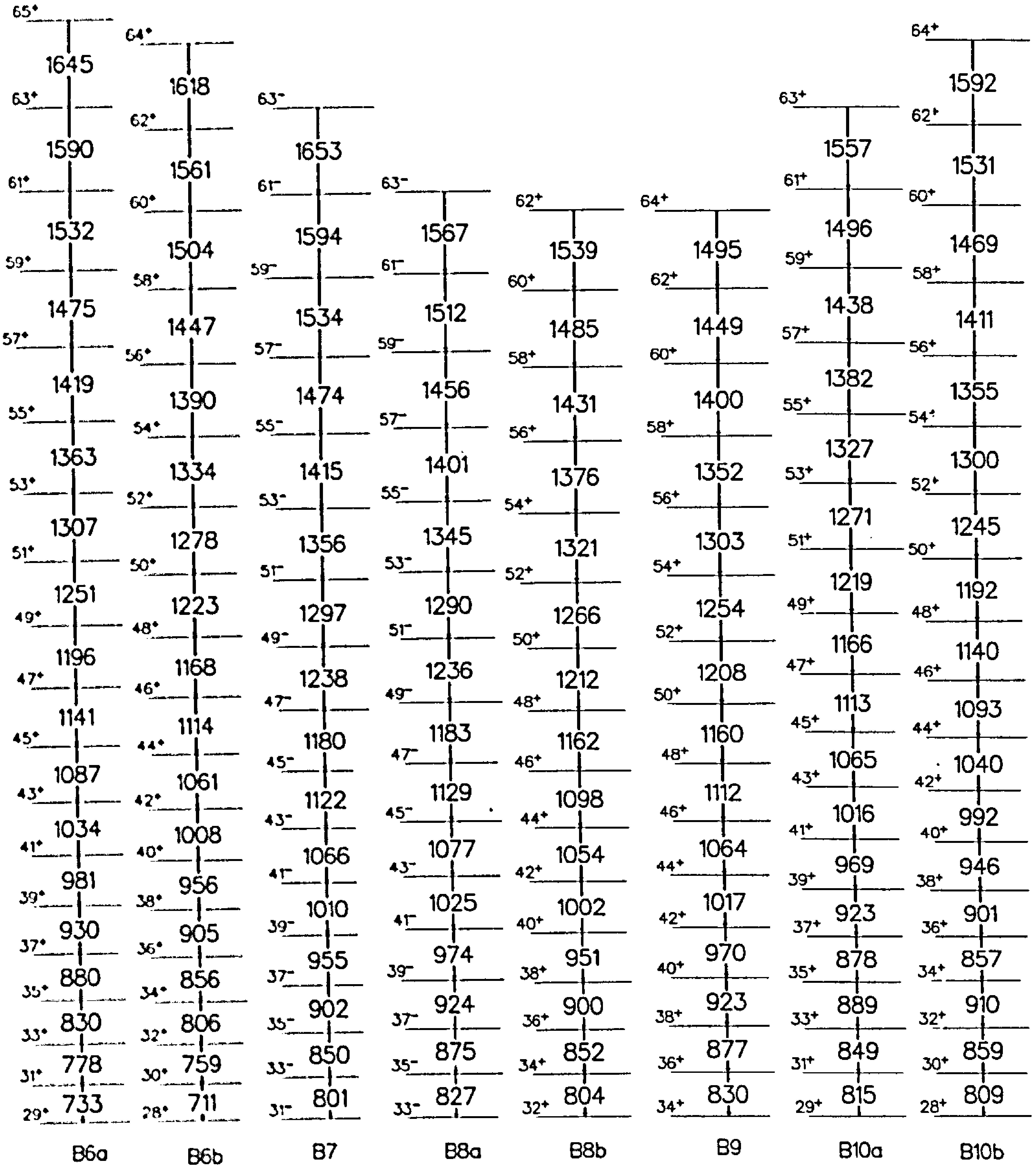

Figure 4.11: The partial level scheme of new SD bands 6-10 observed in ^{150}Gd with their spin-values.

4.2 Discussion

4.2.1 Dynamic Moments of Inertia and the high-N Configurations

An interpretation of the experimental dynamic moments of inertia for SD bands enables their microscopic structure close to the Fermi surface to be determined. In order to determine the high-N intruder configuration for the newly-observed SD bands in ^{150}Gd , the $\mathcal{J}^{(2)}$ moment of inertia of these bands is compared with the $\mathcal{J}^{(2)}$ moments of inertia of the yrast SD bands in the adjacent Z = 64, 65, 66 and N = 84, 85, 86, 87 nuclei. Using this method also allows determination of whether the bands are based on neutron or proton excitation. The $\mathcal{J}^{(2)}$ of the new bands, along with the suitable yrast SD bands in the adjacent nuclei, are presented in Figure 4.12 and Figure 4.13.

Although there are no important changes in the $\mathcal{J}^{(2)}$ of the previously-known bands in ^{150}Gd, they are discussed here to emphasise the effects of the new transitions and also for comparison with the newly-observed bands. Accordingly, it is useful to review their behaviour and configurations in order to compare and understand the structures of bands in ^{150}Gd.

Band 1 (B1)

The observed variations in the dynamic moment of inertia $\mathcal{J}^{(2)}$ of band 1 in ^{150}Gd are very large. Indeed, they are among the largest observed of the known yrast SD bands of the A $\approx$ 150 mass region [Af96]. These variations in the $\mathcal{J}^{(2)}$ for band 1 (see Figure 4.13) are characterised by a rapid increase in magnitude at $\hbar\omega \approx 0.4$ MeV, which has been attributed to a paired neutron N = 7 band-crossing [Na89]. Additionally, the small deviation in the $\mathcal{J}^{(2)}$ at $\hbar\omega \approx 0.5$ MeV is brought about by the alignment of a pair of N = 6 protons [Na89]. The large decrease in $\mathcal{J}^{(2)}$ with increasing frequency has been explained using CSM calculations in terms of the $\pi 6^2 \nu 7^2$ (+ , + i) configuration, (see Ref. [Na89]).

Band 2 (B2)

At high frequencies (above $\hbar\omega \approx 0.5$ MeV), the transition energies of B2 are very similar to the yrast SD band in ^{152}Dy, which has two additional protons in high N = 6 orbitals and has the configuration $\pi 6^4 \nu 7^2$. The $\mathcal{J}^{(2)}$ moment of inertia of B2 (see Figure 4.12) is, therefore, expected to approach that of SD band 1 in ^{152}Dy. This is, indeed, observed with increasing frequency. In view of these similarities, band 2 is assigned the same high-N intruder configuration as the yrast SD band in ^{152}Dy. There are, however, large differences in measured $\mathcal{J}^{(2)}$ between these two bands at low frequencies. Furthermore, the $\mathcal{J}^{(2)}$ for B2 exhibits irregularities and then experiences a sudden discontinuity. This discontinuity indicates that a band-crossing (or interaction) has occurred at $\hbar\omega \approx 0.45$. It is suggested that this band is based on a 2-proton(π) 2-hole (2p-2h) excitation from the ^{150}Gd SD core [Fa94].

Band 3 (B3)

Figure 4.12 shows a comparison of the $\mathcal{J}^{(2)}$ for ^{150}Gd Band 3 and ^{151}Tb band 1 ($\pi 6^3 \nu 7^2$). As can be observed from Figure 4.12, the $\mathcal{J}^{(2)}$ of B3 shows a smooth decrease from $\mathcal{J}^{(2)} = 92$ to 78 $\hbar^2 MeV^{-1}$ over the frequency range of $0.35 \leq \hbar\omega \leq 0.8$ MeV, with the exception of a small discontinuity at $\hbar\omega \approx 0.6$ MeV. This discontinuity in the $\mathcal{J}^{(2)}$ indicates that two transitions in B3 are slightly perturbed from their smoothly varying positions. Since there are many similarities between these two bands, it is expected that the bands have the same high-N intruder configuration and, consequently, it is suggested that this band is based on a proton excitation from the ^{150}Gd SD core [Bea93].

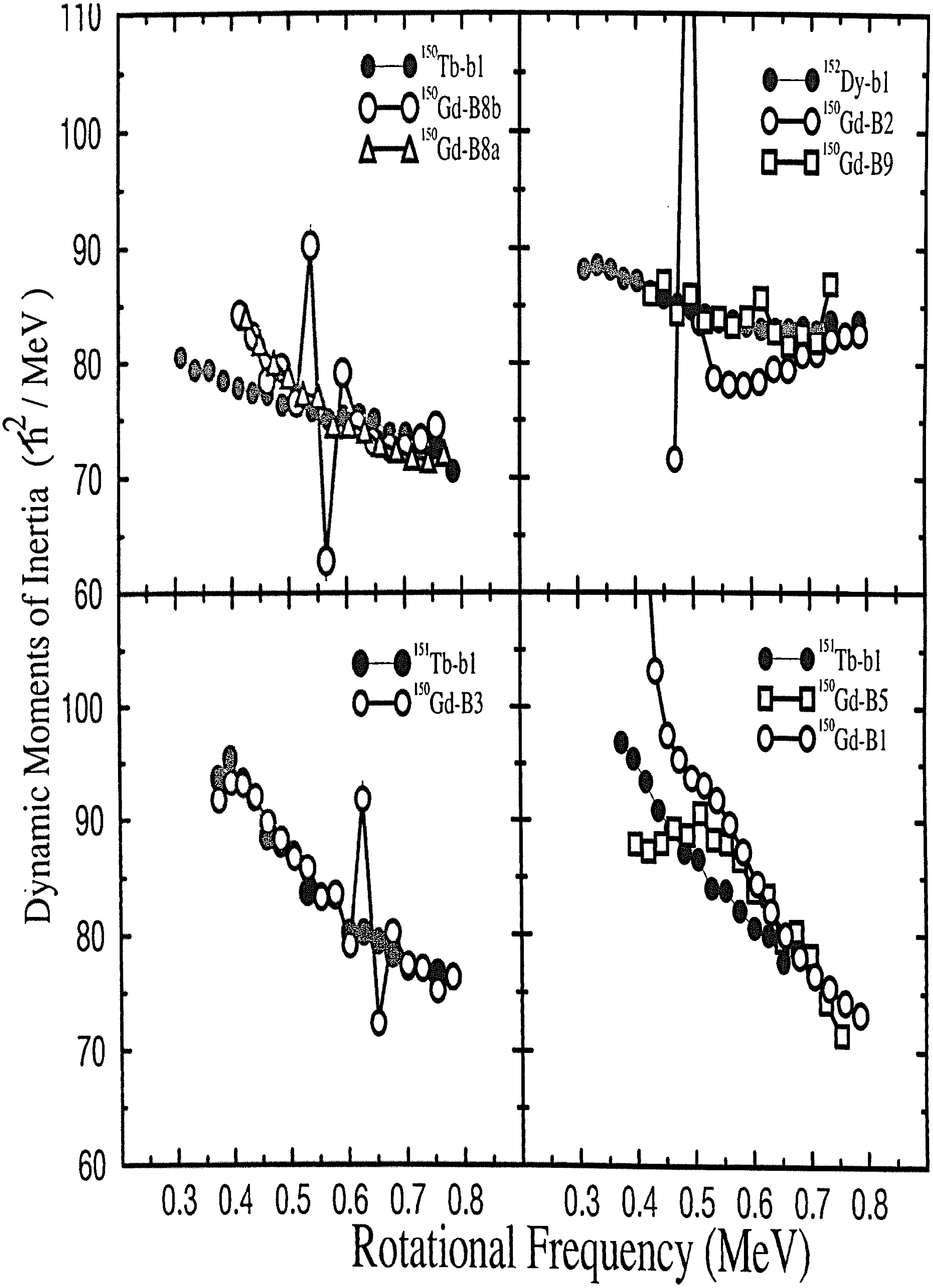

Figure 4.12: Dynamic Moments of Inertia for bands B2, B3, B5, B8a, B8b and B9 in ^{150}Gd compared with the yrast SD bands of neighbouring nuclei.

Band 4a (B4a) and Band 4b (B4b)

The transition energies for band 4a lie at the midpoints of transitions for band 4b, indicating that these bands are signature-partners based on an orbital which exhibits very little signature-splitting as a function of rotational frequency. Moreover, these bands have similar $\mathcal{J}^{(2)}$ moments of inertia (see Figure 4.13). The dynamic moments of inertia $\mathcal{J}^{(2)}$ appear to be very similar to those of the yrast SD band in ^{149}Gd, which has the configuration $\pi 6^2 \nu 7^1$. This indicates that B4a and B4b are based on a neutron particle-hole excitation from the second N = 7 intruder orbital into either signature of a relatively flat low-N natural parity orbital which exhibits little or no signature-splitting. A small discontinuity is also evident in B4a but is displaced in the opposite direction to that observed in B3. These discontinuities can be observed in the $\mathcal{J}^{(2)}$ of band 3 and of band 4a (see Figure 4.12 and Figure 4.13) at $\hbar\omega \approx 0.65$ MeV, evidence that both structures have perturbed transition energies [Bea93].

Band 5 (B5)

Previously it was suggested [Cl95] that this band was based on the configuration $\pi 6^3 \nu 7^2$; however, due to the improved energy measurements obtained in this work, the $\mathcal{J}^{(2)}$ of band 5 lies closer to that of the yrast SD band in ^{150}Gd rather than the yrast SD band in ^{151}Tb (see Figure 4.12), suggesting a configuration based on $\pi 6^2 \nu 7^2$. The $\mathcal{J}^{(2)}$ of band 5 is similar to that of the yrast SD band of ^{150}Gd over the frequency range $0.5 \leq \hbar\omega \leq 0.8$ MeV. At the $\hbar\omega \approx 0.5$ MeV, the $\mathcal{J}^{(2)}$ of band 5 suddenly flattens out while that for band 1 rising continiuosly. This difference will be discussed in Section 4.2.2 in terms of the effect of a single-neutron excitation.

Band 6a (B6a) and Band 6b (B6b)

Due to the relationship between the transition energies (that lie halfway between each other) of band 6a and of band 6b, these bands are believed to be signature-partners based on an orbital which exhibits little or no signature splitting as a function of rotational frequency. The $\mathcal{J}^{(2)}$ of B6a and B6b (see Figure 4.13) is very similar to and closely follows that of the ^{149}Gd yrast SD band, which has a $\pi6^2\nu7^1$ high-N configuration. Due to this similarity, it is suggested that these bands are based on the excitation of a neutron from a high-N intruder into a low-N natural parity orbital which exhibits little or no signature-splitting.

Band 7 (B7)

B7 has a $\mathcal{J}^{(2)}$ that decreases constantly from $\mathcal{J}^{(2)} = 80$ to 68 $\hbar^2 MeV^{-1}$ over the frequency range $0.4 \leq \hbar\omega \leq 0.8$ MeV (see Figure 4.13). The dynamic moment of inertia $\mathcal{J}^{(2)}$ of B7 in ^{150}Gd is similar to the yrast SD of ^{149}Gd, but with a lower magnitude. The $\mathcal{J}^{(2)}$ of B7 actually follows closely the $\mathcal{J}^{(2)}$ of the yrast SD band in ^{148}Gd, which suggests that this band has the same high-N intruder configuration ($\pi6^2\nu7^1$) as ^{148}Gd (see Ref. [Af96]). This would indicate that band 7 is based on a neutron particle-hole excitation.

Band 8a (B8a) and Band 8b (B8b)

The transition energies for band 8a lie at the midpoints of transitions for band 8b, indicating that these bands are signature-partners. They have very similar moments of inertia (see Figure 4.12) that smoothly decreases in magnitude from 84 to 74 $\hbar^2 MeV^{-1}$ over the frequency range $0.4 \leq \hbar\omega \leq 0.75$ MeV, with the exception of a small discontinuity just above $\hbar\omega \approx 0.5$ MeV in band 8b, showing that there is an interaction. This indicates that one or more transitions in B8b are slightly perturbed from their smoothly-varying positions. The $\mathcal{J}^{(2)}$ of these bands are similar to that of the yrast SD band in ^{150}Tb, and, therefore, should have the same high-N configuration ($\pi6^3\nu7^1$). Accordingly, band 8a and band 8b have been assigned as a neutron excitation from high-N intruder to a low-N natural parity state and a proton excitation from low-N natural parity orbital into an N = 6 intruder.

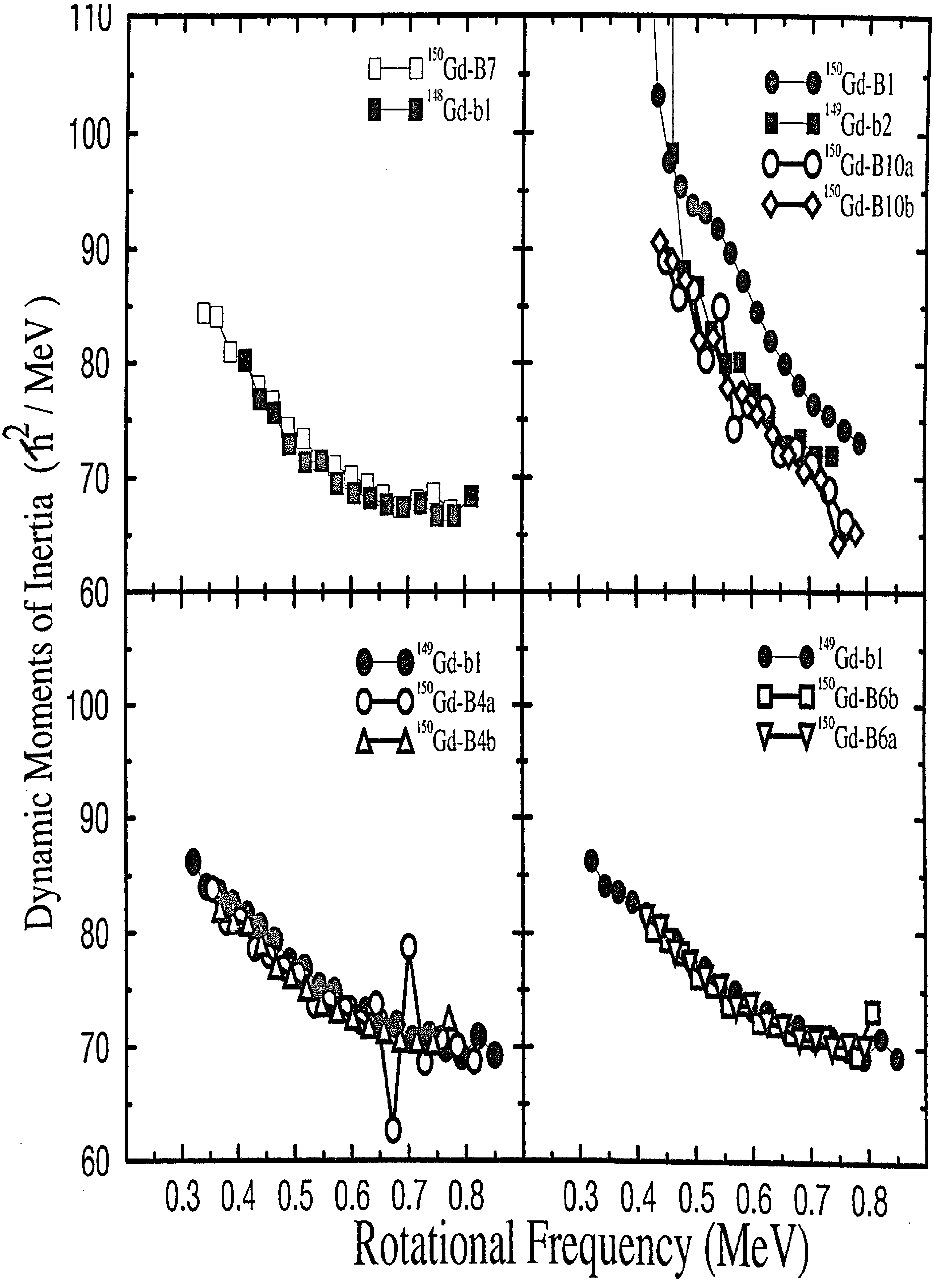

Figure 4.13: Dynamic Moments of Inertia for B1, B4a, B4b, B6a, B6b, B7, B10a and B10b in ^{150}Gd compared with the yrast SD bands of neighbouring nuclei.

Band 9 (B9)

Figure 4.12 shows a comparison between the $\mathcal{J}^{(2)}$ of B9 and the yrast SD band of ^{152}Dy. Over the entire frequency range, the transition energies of B9 are very similar and almost identical to the yrast SD band in ^{152}Dy, which has a $\pi 6^4 \nu 7^2$ configuration. It follows, therefore, that the $\mathcal{J}^{(2)}$ of B9 is almost constant as a function of rotational frequency and closely follows the $\mathcal{J}^{(2)}$ of the yrast SD band in ^{152}Dy. This suggests that this band has the same high-N intruder configuration ($\pi 6^4 \nu 7^2$) as ^{152}Dy, indicative of a 2p-2h excitation.

Band 10a (B10a) and Band 10b (B10b)

The transition energies of band 10a lie at the midpoints of transitions in band 10b, indicating that these bands are signature-partners based on an orbital which exhibits very little signature-splitting as a function of rotational frequency. Consequently, they have very similar moments of inertia (see Figure 4.13). The dynamic moment of inertia $\mathcal{J}^{(2)}$ of these two bands is similar to the yrast SD band in ^{150}Gd, but the magnitude of $\mathcal{J}^{(2)}$ is smaller. The $\mathcal{J}^{(2)}$ of B10a and B10b closely follow the $\mathcal{J}^{(2)}$ of a first excited SD band (band 2) in ^{149}Gd, implying that these bands have the same high-N intruder configuration ($\pi 6^2 \nu 7^2$) as the yrast SD band in ^{150}Gd and suggesting that this band is based on a neutron excitation.

4.2.2 Configurations of the Superdeformed Bands in ^{150}Gd

The calculated single-particle Routhians for protons and neutrons in ^{150}Gd are shown in Figures 4.14, 4.15, 4.16. The structure of SD bands will be described by employing this figure as well as using the relative alignment plots for proton orbitals(see Figure 4.17) and neutron orbitals (see Figure 4.18).

Structure of Yrast SD Band 1 (B1)

The filled black circles in Figure 4.14.(a,b) represent nucleons occupying orbitals at the Fermi surface of ^{150}Gd. In the single-particle Routhian diagram for protons (see Figure 4.14.(b)), the 61^{st} and the 62^{nd} nucleons occupy both signatures of the N = 6 $[660]1/2^+$ orbital, with the 63^{rd} and the 64^{th} protons occupying both signatures of the low-N $[301]1/2^-$ orbital. Figure 4.14.(a) shows the single-particle Routhians diagram for the neutrons of band 1: the 85^{th} and 86^{th} neutrons occupy both signatures of the first N = 7 $[770]1/2^-$ orbital. This ground-state ($\pi 6^2 \nu 7^2$) configuration results in the yrast superdeformed band having levels of even spin and even parity $(\pi, \alpha) = (+\ ,\ 0)$.

Structure of Band 2 (B2)

At high frequency, the configuration of band 2 is considered to be a 2p-2h excitation relative to the ^{150}Gd SD core. This requires that two protons be promoted from a flat, low-N orbital, such as the $\pi[301]1/2^-$, into the $\pi 6^3$ and $\pi 6^4$ levels (see Figure 4.14.(c)). Consequently, the configuration of B2 is designated as $\pi 6^4 \otimes ([301]1/2^-)^{-2} \nu 7^2$. The assigned parity and signature of B2 are deduced from the above configuration and, hence, the levels have positive parity and even spin $(\pi, \alpha) = (+, 0)$.

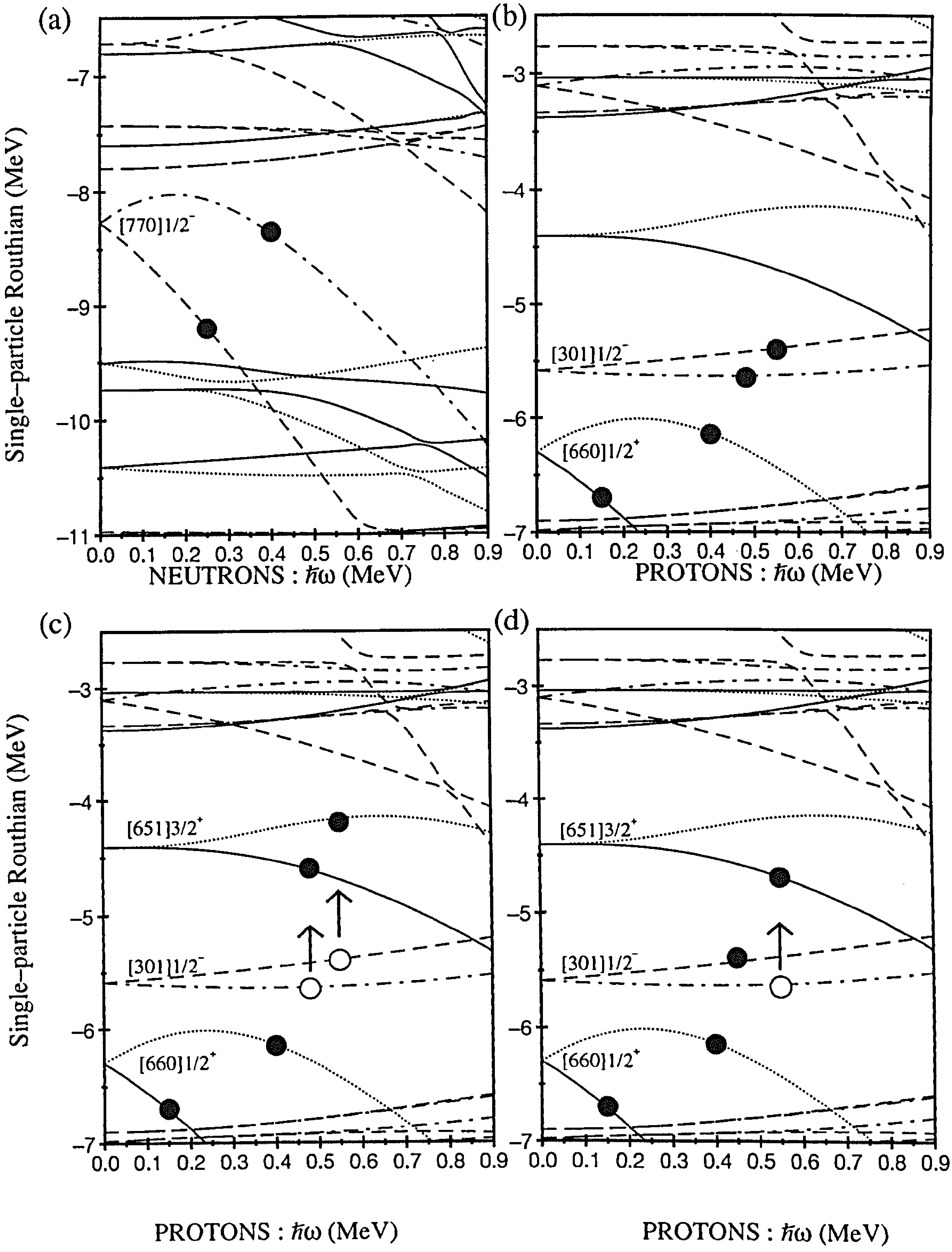

Figure 4.14: Single-particle Routhians for neutrons (a),(c) and protons (b),(d) calculated with the deformation parameters $\beta_2 = 0.58$, $\beta_4 = 0.1$ and $\gamma = 0°$ as a function of rotational frequency for ^{150}Gd; (a) and (b) for band 1, (c) for band 2 (d) for band 3. The parity (π) and signature (α) of the levels are indicated in the following way: (π, α) : solid=(+,+1/2), dotted=(+,-1/2), dot-dash=(-,+1/2), dashed=(-,-1/2).

Structure of Band 3 (B3)

A comparison of $\mathcal{J}^{(2)}$ with the calculated proton single-particle Routhians (see Figure 4.14.(d)) suggests that the most likely band assignment arises from a particle excitation at the $\alpha = +1/2$ signature of the $[301]1/2^{-}$ orbital into the $\alpha = +1/2$ signature of the $[651]3/2^{+}$ orbital. The calculated single-particle Routhians predict that the proton $[301]1/2^{-}$ orbital exhibits very little signature-splitting over the frequency range $0.2 \leq \hbar \leq 0.8$ MeV; this has also been confirmed experimentally [Cl95]. Hence, it is expected that band 3 should have a signature-partner band based on the excitation of a proton from the $\alpha = -1/2$ signature of the $[301]1/2^{-}$ orbital. Previously, it was suggested [Cl95] that band 5 was the signature-partner of band 3 but the statistics obtained with this data set have allowed the observation of more transitions in band 5, hence showing that this band has a different structure to that of band 3. The relative alignment of band 3 (see Figure 4.17) using ^{151}Tb as a reference is nearly constant with rotational frequency. This lends further confirmation of a correlation between band 3 and the ^{151}Tb yrast band. The band is assigned $\pi 6^3([301]1/2^{-})^{-1}\nu 7^2$ configuration, and, hence, the parity and signature of B3 are $(\pi, \alpha) = (-, 0)$.

Structure of Band 4a (B4a) and Band 4b (B4b)

These bands, built on neutron excitations, have the same high-N configuration as the yrast SD band in ^{149}Gd which has one neutron fewer than ^{150}Gd and may be described by a configuration that couples a hole in the $[770]1/2^{-}$ ($\alpha = +1/2$) orbital to the ^{150}Gd core (see Figure 4.15.(a)). The apparent similarities in $\mathcal{J}^{(2)}$ (see Figure 4.13) between B4a and B4b and the yrast band in ^{149}Gd indicate that these bands have identical intruder configurations. A neutron is excited from the $\nu[770]1/2^{-}$ orbital into both signatures of the $\nu[402]5/2^{+}$ orbital, and Figure 4.18 shows almost constant alignment with rotational frequency for B4a and B4b relative to the yrast SD band in ^{149}Gd. This established that B4a and B4b have a similar configuration as the yrast SD band in ^{149}Gd and, therefore, that the configuration of the two bands is $\pi 6^2 \nu 7^1 \otimes [402]5/2^{+}$. The parity and signatures are $(\pi, \alpha) = (-, 1)$ for B4a, and $(\pi, \alpha) = (-, 0)$ for B4b.

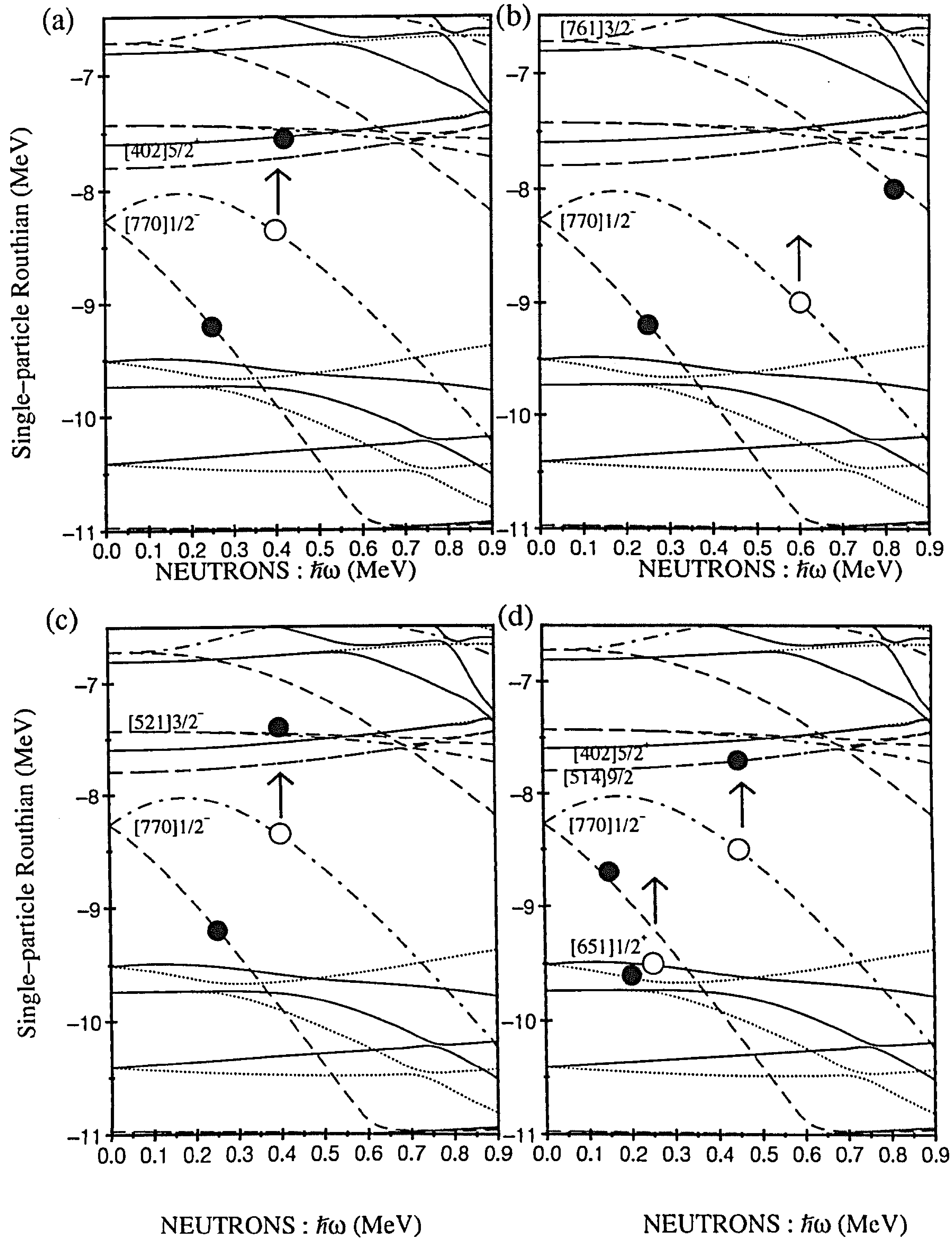

Figure 4.15: Single-particle Routhians for neutrons (a),(c) and protons (b),(d) calculated with the deformation parameters $\beta_2 = 0.58$, $\beta_4 = 0.1$ and $\gamma = 0°$ as a function of rotational frequency for ^{150}Gd; (a) for bands 4a and 4b, (b) for band 5, (c) for bands 6a and 6b and (d) for band 7.

Structure of Band 5 (B5)

As indicated in Section 4.2.1, the high-N configuration for band 5 is expected to be the same as that for band 1. However, at low frequency, the $\mathcal{J}^{(2)}$ for bands 1 and 5 diverge: one becomes flat, the other increasing in magnitude with decreasing spin. This high moment of inertia at low frequency for band 1 has been understood in terms of a paired N = 7 neutron crossing, while the "bump" at $\hbar\omega \approx 0.5$ MeV has been understood in terms of N = 6 proton crossing. It is, consequently, suggested that band 5 undergoes the same paired-proton crossing as band 1, but not the neutron crossing, indicating that band 5 is based on a neutron excitation from the 7^2 into 7^3 (see Figure 4.15. (b)). The reasons behind this are as follows:

1. The $\mathcal{J}^{(2)}$ similar to ^{150}Gd band 1 suggests the high-N configuration is $\pi 6^2 \nu 7^2$, but the measured Q_o for band 5 is 15.4 ± 0.8 eb is somewhat lower than band 1 (17.0 ± 0.5) [Bea98]. The proposed excitation gives the high-N configuration to be $\pi 6^2 \nu 7^2$ while lowering the Q_o as the 7^3 orbital is not as deformation-driving as 7^2.

2. Nazarewicz *et al.,* calculated the contribution to the $\mathcal{J}^{(2)}$ of the yrast band in ^{150}Gd for both protons and neutrons (figure 12 in Ref. [Na89]). From this calculation, the flattening of the $\mathcal{J}^{(2)}$ for band 5 can be understood as paired-proton crossing.

3. No evidence is observed for the paired N = 7 neutron crossing, which is expected to occur if both the 7^1 and 7^2 are occupied, suggesting that this crossing is blocked. The blocking can be interpreted as taking a neutron from 7^2 orbital into $[521]3/2^-$, $[402]5/2^+$, $[514]9/2^-$ or $[761]3/2^-$ orbitals; however, the first two have bands based upon them (B6a,B6b, and B4a,B4b) while the third $[514]9/2^-$ would require a signature-partner band. Thus, the only remaining possibility is the $[761]3/2^-$ orbital. Since band 5 has 32% intensity a signature-partner band should have been observed, so it must be concluded that it does not exist.

Therefore, band 5 has a configuration $\pi 6^2 \nu 7^2([770]1/2^-)^{-1}([761]3/2^-)^1$. Accordingly, the parity and signatures are $(\pi, \alpha) = (-, 0)$.

Structure of Band 6a (B6a) and Band 6b (B6b)

These bands, built on neutron excitations, have the same high-N configuration as the yrast SD band in ^{149}Gd. As shown in Figure 4.15.(c), the 86^{th} neutron is excited from the $[770]1/2^-$ level into both the signatures of the $[521]3/2^-$ orbitals. In Figure 4.17, the relative alignment of B6a and B6b has been plotted relative to the yrast SD band in ^{149}Gd, demonstrating that the relative alignment is constant with rotational frequency, and has a magnitude of $\Delta i = 0.5\ \hbar$. The relative alignment plots confirm that B6a and B6b have a configuration that is related to that of the yrast SD band in ^{149}Gd. Consequently, the parity and signatures are $(\pi, \alpha) = (+, 0)$ for B6a, and $(\pi, \alpha) = (+, 1)$ for B6b.

Structure of Band 7 (B7)

The $\mathcal{J}^{(2)}$ moment of inertia of B7 (see Figure 4.13) indicates that B7 has the same high-N configuration as that of the yrast SD band in ^{148}Gd, in which case the 86^{th} neutron (see Figure 4.16.(d)) has to be excited out of the $[770]1/2^-$ orbital into either the $[402]5/2^+$ orbital or the $[514]9/2^-$ orbital. In addition, the 85^{th} neutron needs to be promoted out of the $[651]1/2^+$ orbital into either the $[402]5/2^+$ orbital or the $[514]9/2^-$ orbital. The alignment of B7 (see Figure 4.18) relative to the yrast SD band in ^{148}Gd is $\Delta i = -0.5\ \hbar$ at high frequencies but is close to zero at low frequencies. This confirms that B7 has a configuration related to that of the yrast SD band in ^{148}Gd and is, hence, based on either $\pi 6^2 \nu 7^1 \otimes ([402]5/2)^{+2}([651]1/2^+)^{-1}([770]1/2^-)^{-1}$ or the $\pi 6^2 \nu 7^1 \otimes ([514]9/2)^{+2}([651]1/2^+)^{-1}([770]1/2^-)^{-1}$ configuration. The parity and signatures derived from the above configuration are $(\pi, \alpha) = (-, 1)$.

Structure of Band 8a (B8a) and Band 8b (B8b)

These bands are assigned both a proton and a neutron excitation since its $\mathcal{J}^{(2)}$ is similar to that of the yrast SD band in ^{150}Tb ($\pi6^3\nu7^1$). The configuration is based on a proton excitation from the [301]1/2$^-$ orbital into both signatures of the [651]3/2$^+$ orbitals (see Figure 4.16.(b)), and a neutron excitation from the [770]1/2$^-$ orbital into both signatures of either the low-N orbitals [402]5/2$^+$ or [521]3/2$^-$ (see Figure 4.16.(a)). The alignment of B8a and B8b (see Figure 4.17) relative to the yrast SD band in ^{150}Tb is almost zero over the entire frequency range, except at the crossing-point at $\hbar = 0.55$ MeV in B8b. This also indicates that B8a and B8b have the same configuration as the yrast SD band in ^{150}Tb. Therefore, it is assigned the configuration $\pi6^3 \otimes ([301]1/2^-)^{-1}\nu7^1 \otimes ([402]5/2^+)^{+1}$, with the parity and signatures being $(\pi, \alpha) = (+, 0)$ for B8a, and $(\pi, \alpha) = (+, 1)$ for B8b.

Structure of Band 9 (B9)

The $\mathcal{J}^{(2)}$ moment of inertia of B9 (see Figure 4.12) indicates that B9 has the same high-N configuration as that of the yrast SD band in ^{152}Dy ($\pi6^4\nu7^2$). In order to achieve this, the 63rd and 64th protons have to be promoted out of the [301]1/2$^-$ orbitals into [651]3/2$^+$ orbital (see Figure 4.16.(d)). The alignment of B9 (see Figure 4.17) relative to the yrast SD band in ^{152}Dy shows that the relative alignment of B9 is almost zero at all frequencies since its energies are identical to the yrast SD band of ^{152}Dy, thus supporting a configuration for B9 similar to that of the yrast SD band in ^{152}Dy. Consequently, the configuration of B9 is assigned as $\pi6^4 \otimes ([301]1/2^-)^{-2}\nu7^2$, and the parity and signatures are $(\pi, \alpha) = (+, 0)$.

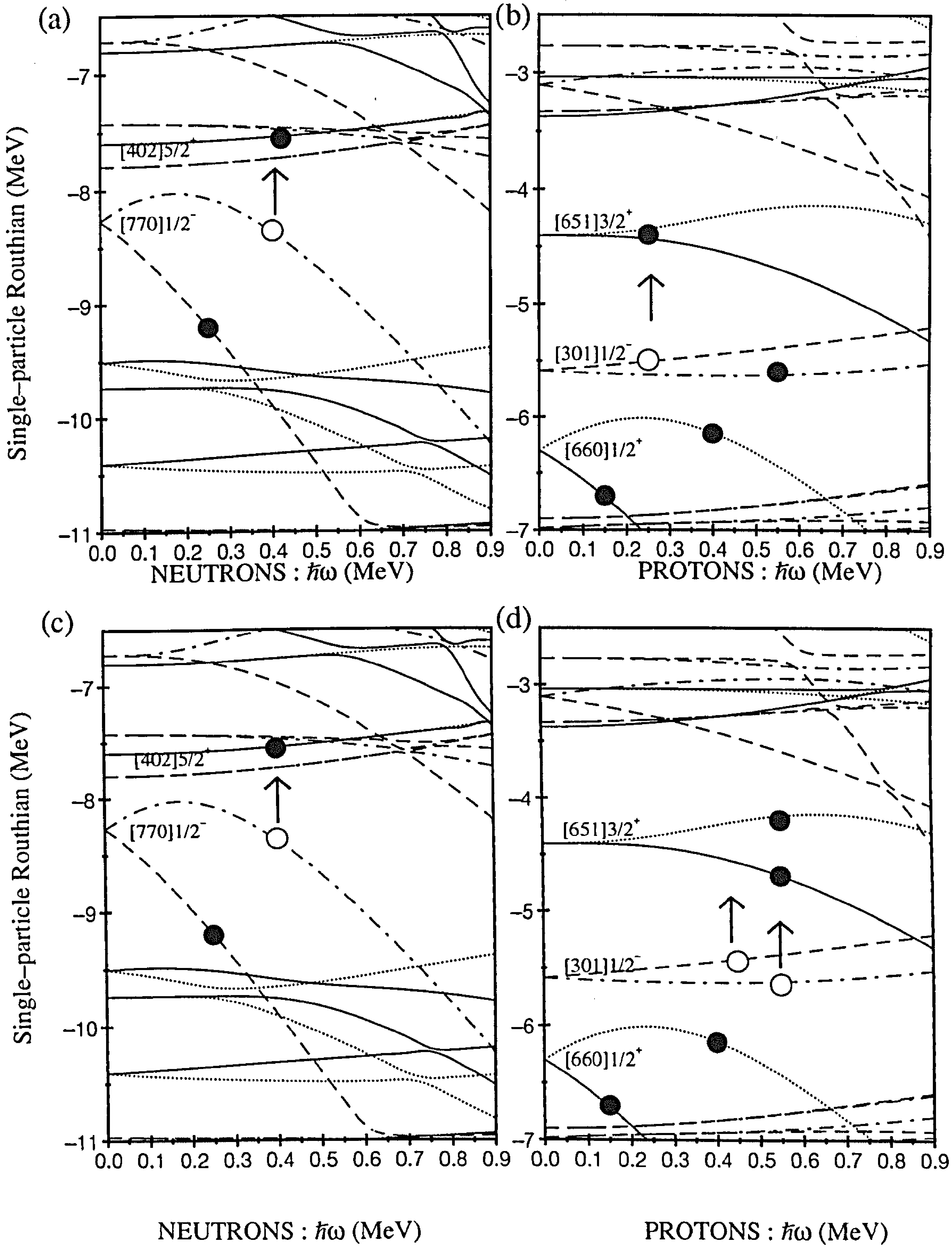

Figure 4.16: Single-particle Routhians for neutrons (a),(c),(d) and protons (b) calculated with the deformation parameters $\beta_2 = 0.58$, $\beta_4 = 0.1$ and $\gamma = 0°$ as a function of rotational frequency for ^{150}Gd; (a) and (b) for bands 8a, 8b (c) for bands 10a, 10b and (d) for band 9.

Structure of Band 10a (B10a) and Band 10b (B10b)

These bands are assigned as neutron excitations since they have the same high-N configuration as the ^{149}Gd band 2. In this case, the neutron is promoted from the positive signature of the $[651]1/2^-$ orbital across the N =86 shell-closure into either the negative signature of the $[402]5/2^+$ orbital (B10a) or into the positive signature of $[402]5/2^+$ orbital (B10b) (see Figure 4.16.(c)). The alignment of B10a and B10b (see Figure 4.18) relative to the first excited SD band in ^{149}Gd is virtually constant as a function of rotational frequency. The magnitude of the relative alignment of B10a and B10b is seen to be $\approx \Delta i = -0.3\ \hbar$ at high frequencies and $\Delta i = 0.5\ \hbar$ at low frequencies. This confirms that B10a and B10b have the same configurations as the first excited SD band of ^{149}Gd ($\pi 6^2 \nu 7^2$). The configurations of B10a and B10b are, therefore, $\pi 6^2 \nu 7^2([402]5/2^+)^{+1}([651]1/2^-)^{-1}$, thus denoting that the parity and signatures are $(\pi, \alpha) = (+, 0)$ for B10a, and $(\pi, \alpha) = (+, 1)$ for B10b.

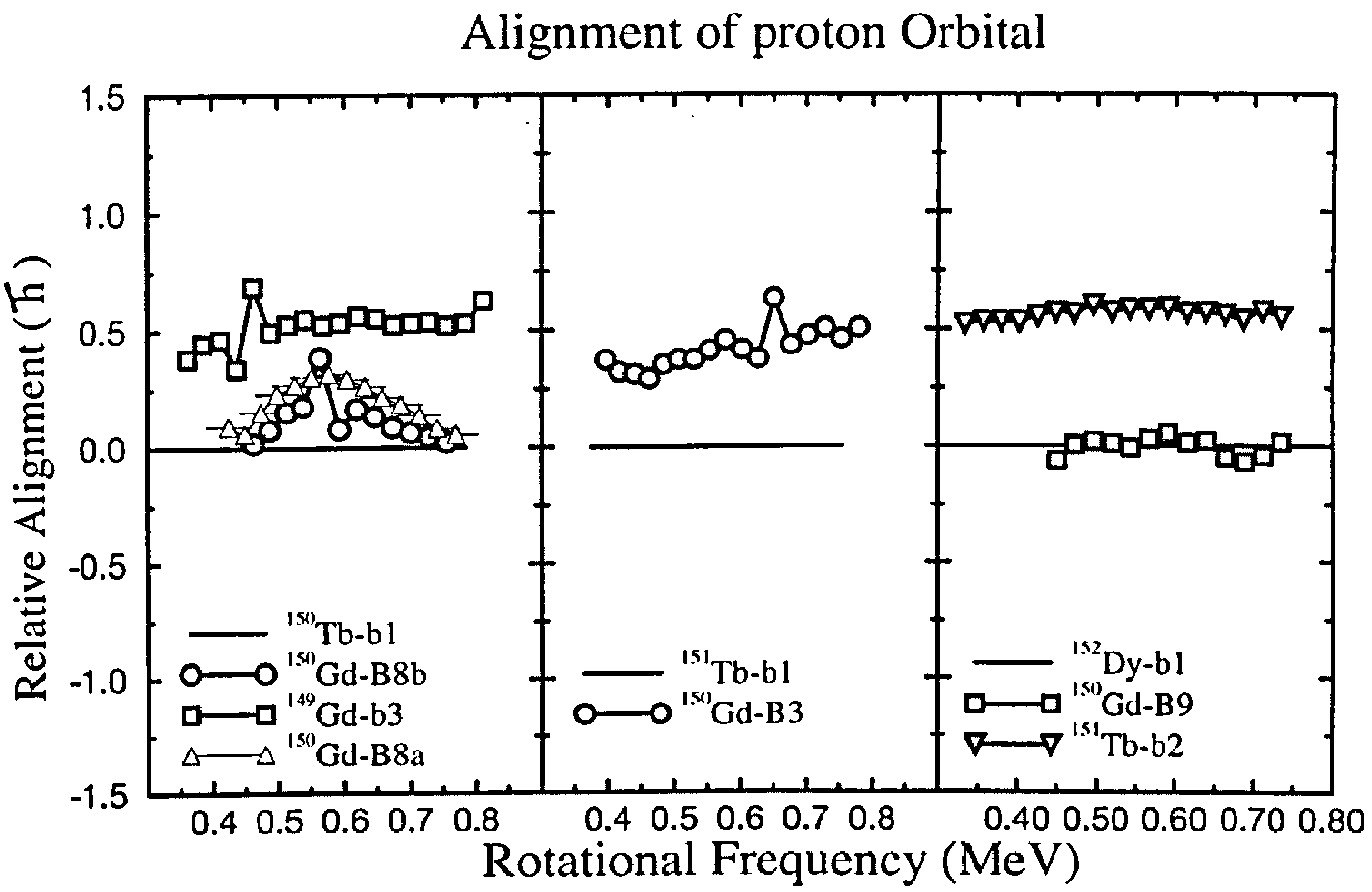

Figure 4.17: The relative alignment for bands 3, 5, 8a, 8b and 9 plotted relative to the reference band represented by the solid line.

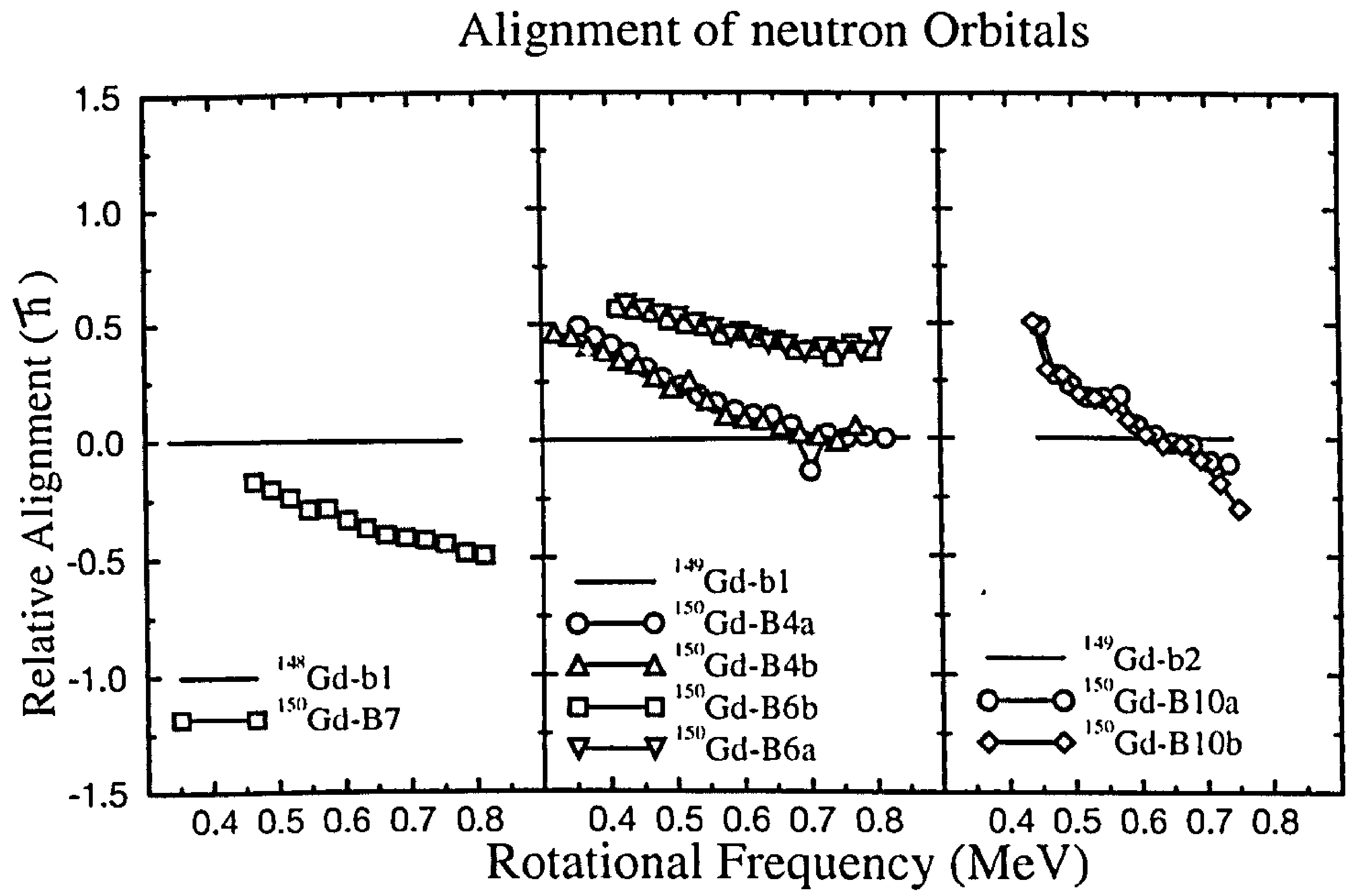

Figure 4.18: The relative alignment for bands 1, 4a, 4b, 6a, 6b, 7, 10a and 10b plotted relative to the reference band represented by the solid line.

The suggested proton and neutron configurations of all SD bands in ^{150}Gd are summarised in Table 4.6 with reference to their previously-known SD bands.

Bands	Configurations	(π, α)	Ref.
1	$\pi 6^2\ \nu 7^2$	(+,0)	[Fa89]
2	$\pi 6^4([301]1/2^-)^{-2}\ \nu 7^2$	(+,0)	[Fa94]
3	$\pi 6^4([301]1/2^-)^{-1}\ \nu 7^2$	(−,0)	[By90]
4a	$\pi 6^2\ \nu 7^1([770]1/2^-)^{-1}([402]5/2^+)^1$	(−,0)	[Bea93]
4b	$\pi 6^2\ \nu 7^1([770]1/2^-)^{-1}([402]5/2^+)^1$	(−,1)	[Bea93]
5	$\pi 6^3\ \nu 7^2([770]1/2^-)^{-1}([761]3/2^-)^1$	(−,0)	*
6a	$\pi 6^2\ \nu 7^1([770]1/2^-)^{-1}([521]3/2^-)^1$	(+,0)	*
6b	$\pi 6^2\ \nu 7^1([770]1/2^-)^{-1}([521]3/2^-)^1$	(+,1)	*
7	$\pi 6^2\ \nu 7^1([651]3/2^+)^{-1}([770]1/2^-)^{-1}([514]9/2^-)^2$	(−,1)	*
8a	$\pi 6^2([301]1/2^-)^{-1}\ \nu 7^2([770]1/2^-)^{-1}([402]5/2^+)^1$	(−,1)	*
8b	$\pi 6^3([301]1/2^-)^{-1}\ \nu 7^2([770]1/2^-)^{-1}([402]5/2^+)^1$	(+,1)	*
9	$\pi 6^4([301]1/2^-)^{-2}\ \nu 7^2$	(+,0)	*
10a	$\pi 6^2\ \nu 7^2([651]1/2^+)^{-1}([402]5/2^+)^1$	(+,0)	*
10b	$\pi 6^2\ \nu 7^2([651]1/2^+)^{-1}([402]5/2^+)^1$	(+,1)	*

Table 4.6: Suggested configurations of all SD bands in ^{150}Gd . * represents the assignments suggested by this present work.

4.3 Linking transitions between Bands 1 and 2

The properties of the backbend observed in SD band 2 of ^{150}Gd have been discussed previously in Refs. [Fa94, Tw94, Tw95] and [Cl95]. Figure 4.19 shows a spectrum of band 2 obtained by setting combinations of three gates on all the γ-ray transitions lying between 1047 keV and 1450 keV. (Note, the 1098 keV transition was not included in order to avoid contamination from band 1). This spectrum shows the region around the backbend γ-rays and the doublets 999 keV, 996 keV and 969 keV, 966 keV with others. There are other γ-rays marked with an asterisk (*), which may be associated with the decay-out of band into the ND states. However, no link between this band and the ND states has been observed. The γ-rays with energies 815 keV, 849 keV, 888 keV, 929 keV and 1014 keV are identical to γ-rays in band 1. This confirms the cross-talk between bands 1 and 2. The γ-rays with energies 856 keV, 901 keV and 949 keV are not observed in coincidence with the other SD bands in ^{150}Gd and neither are they associated with ND states. It is, thus, concluded that they are members of band 2.

Using identical conditions to those described above, with the addition of a gate on the 901 keV transition, it is observed that this γ-ray is in coincidence with the 999 keV members of the higher energy doublet but weakly so with the 966 keV member of the lower-energy doublet. The 901 keV transition is, however, not in coincidence with the two other members of those doublets. From this, it can be concluded that 901 keV transition is parallel to the 999 keV γ-ray (as is shown in Figure 4.20). Furthermore, the 901 keV transition is in coincidence with the 949 keV and 856 keV γ-rays and, therefore, these two transitions are placed with the 901 keV γ-ray as a continuation of band 2 below the band crossing. Beausang *et al.*, extracted the quadrupole moment for band 2 and confirmed the SD nature of these new transitions by measuring their Doppler shifts [Bea98]. This confirmation, along with the coincidence measurements described previously, indicates that these new transitions are a continuation of band 2 and are clearly not associated with the decay-out of the SD band into lower-lying ND states.

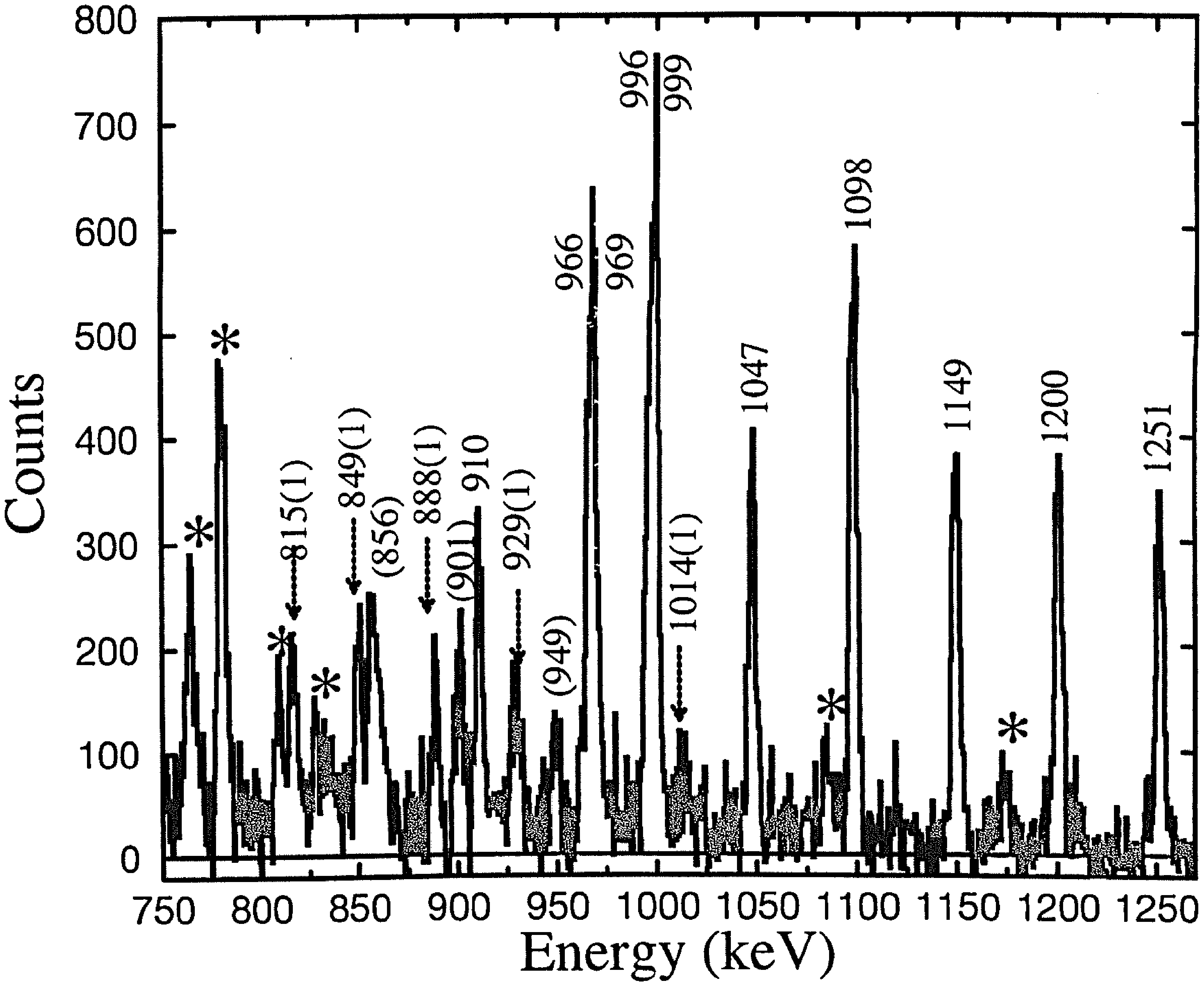

Figure 4.19: Spectrum of SD band 2 in ^{150}Gd obtained by setting three gates on γ-rays in the band from 1047 keV to 1450 keV. The γ-rays with energies of 815 keV, 850 keV, 889 keV, 930 keV and 1014 keV are identical to γ-rays in the yrast band (band 1) of ^{150}Gd. Gamma rays marked with an asterisk (*) are associated with the decay-out of the band into normally deformed states. The γ-rays (856 keV, 901 keV and 949 keV) are new transitions to the lower part of band 2.

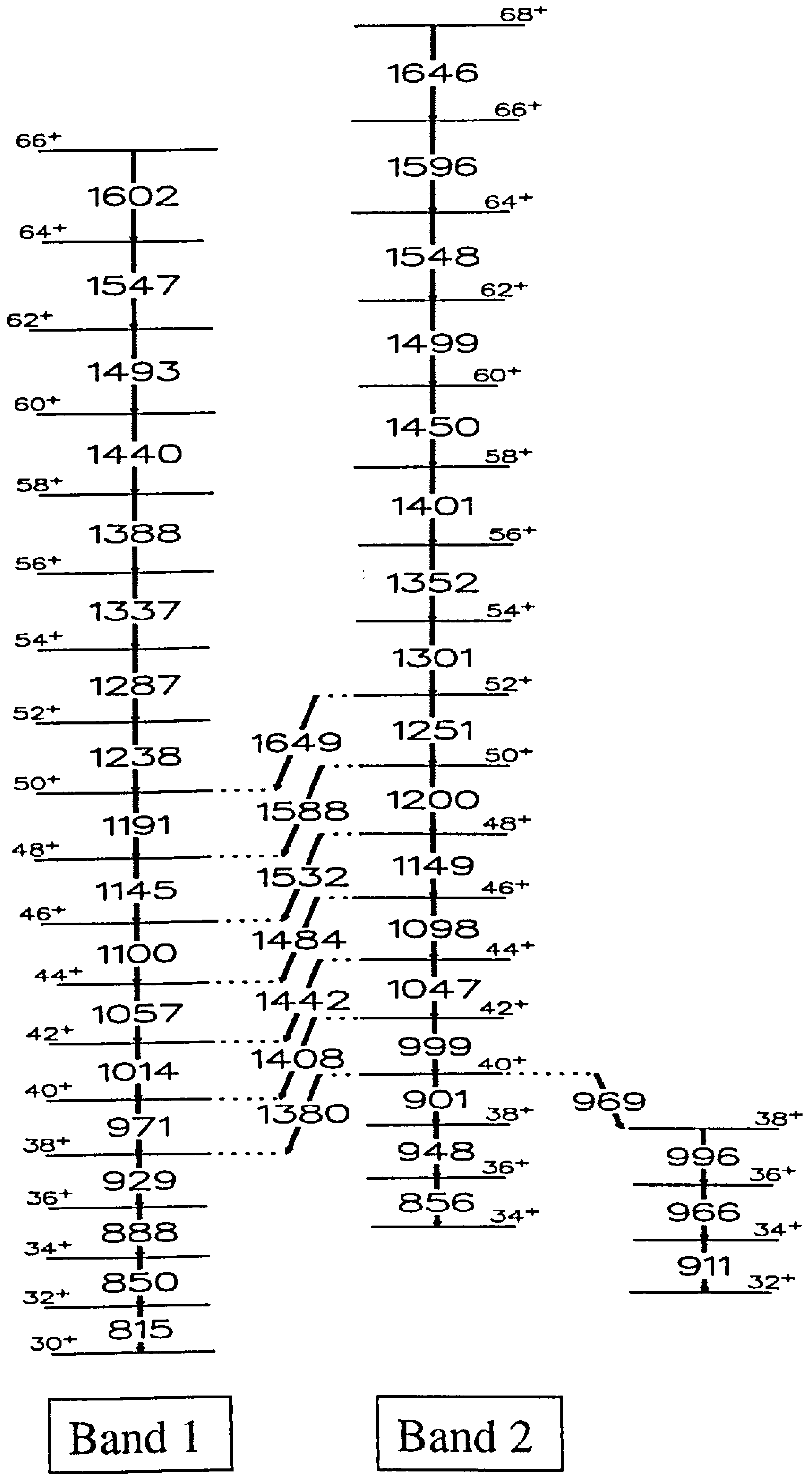

Figure 4.20: The partial decay scheme of SD band 2 in ^{150}Gd showing the proposed continuation of the band below the band-crossing and the linking transitions from SD band 2 to band 1.

The relative intensity of bands 1 and 2 (see Figure 4.21) shows that approximately 50 % of the intensity of band 2 is lost (in the backbend region) via the doublets at 999 keV, 996 keV and 969 keV, 966 keV, followed by the 910 keV transition. However, at the same time, there is a build-up of intensity in the SD band 1 that cannot be associated with gating conditions, because any possible contaminations, have been avoided. Furthermore, only the low energy members of band 1 are observed in the spectrum (see Figure 4.19). This suggests that band 2 decays primarily into band 1. Details of the decay-out of band 2 around the backbend have been established and the links between SD bands 1 and 2 have been identified (see Figure 4.20) [Tw96]. The intensities of the backbend doublets have been estimated from a series of spectra. From these measurements, it transpired that the intensities of the 996 keV, 969 keV and 966 keV transitions are approximately equal and that the difference ($\approx$ 25 %) between these intensities and that of the 999 keV is equal to that of the 901 keV transition (see Figure 4.21). This decay-out into band 1 and the continuation of band 2 below the backbend account for the loss of in-band intensity.

The quadrupole moment of band 2 ($Q_t = 16.8 \pm 1.2$ eb) [Bea98] is similar to that of band 1 ($Q_t = 17.0 \pm 0.5$ eb). This result is consistent with the interpretation of a collective vibrational character for band 2 [Fa94, Nak98]. The quadrupole moment measurement for band 2 provides evidence for the collective vibrational character of this band.

4.3.1 Investigation of Links

The γ-ray linking transitions between bands 1 and 2 were identified from spectra generated by setting two gates on band 2 and one gate on band 1. The two spectra shown in Figure 4.22.(a,b) were obtained by using different gate combinations. In Figure 4.22.(a), the spectrum has two gates from 999 keV to 1450 keV on band 2 and one gate from 850 keV to 929 keV on band 1. The spectrum in Figure 4.22.(b), has gates on band 2 restricted between 1149 keV and 1450 keV while the gates on band 1 have been extended up to 1057 keV. A series of seven γ-ray transitions from 1380 keV

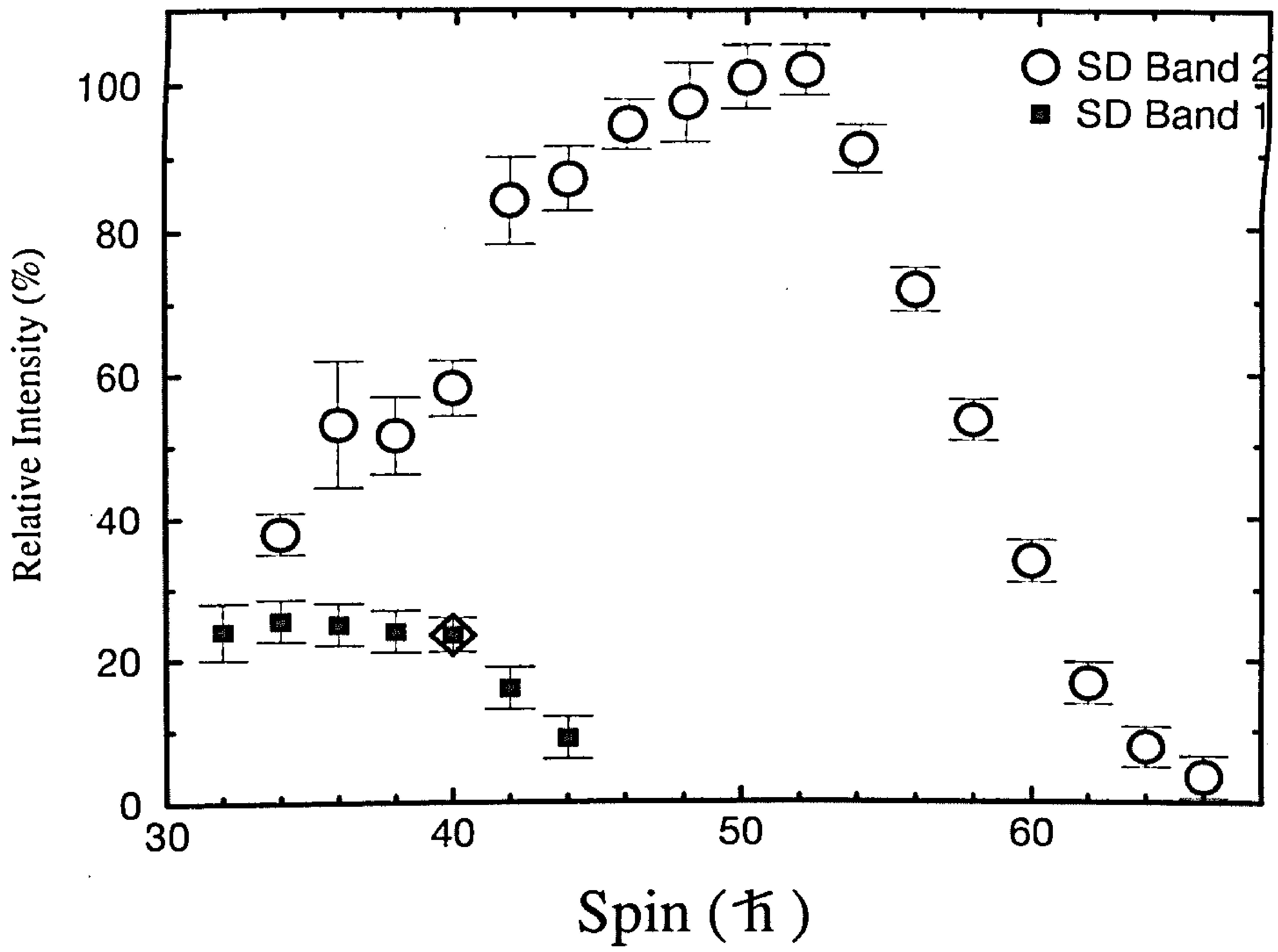

Figure 4.21: The relative intesity of bands 1 and 2. The intensity of band 1 transitions has been extracted from the spectrum obtained as described in the text, and has been normalised to the intensity of band 1. Empty circles represent the band 2, filled squares represent band 1. Diamond symbol represents one of the new 901 keV transitions in band 2.

up to 1649 keV have been observed in these spectra which are in coincidence with both bands 1 and 2 and have been accordingly assigned as linking transitions. In order to identify these linking transitions, a comparison was made between two spectra, it can be seen that the 1380 keV γ-ray is much stronger than other linking transitions (see Figure 4.22.(a)) which has gates extending down to 999 keV in band 2. However, the higher energy γ-ray linking transitions are stronger in Figure 4.22.(b) where the gates on band 1 are extended to the higher energies (up to 1057 keV). The observation and measurement of the γ-ray linking transitions indicates unambiguously that bands 1 and 2 are linked, as shown in the level scheme (see Figure 4.20). From this, it can be observed that the decay between the bands occurs at spins above the backbend.

This is in contrast to the previous suggestion by Fallon *et al.*, [Fa94] which proposed that the inter-band decays were initiated by the backbend.

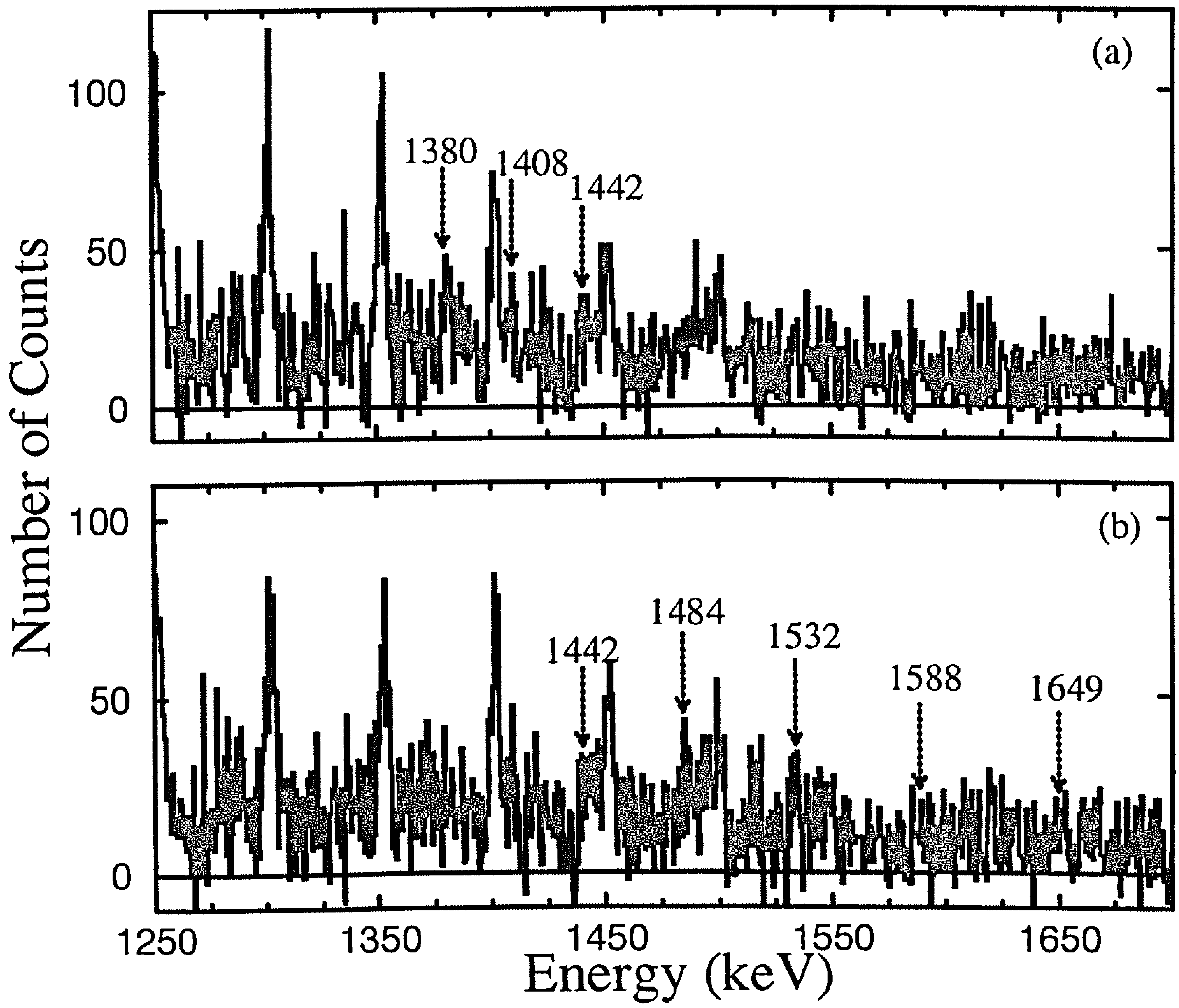

Figure 4.22: Spectra of SD band 2 in ^{150}Gd showing linking transitions to SD band 1. (a) Two gates are set on transitions in band 2 from 999 keV to 1450 keV (except 1098 keV) and two gates are set on transitions in band 1 from 850 keV to 929 keV. (b) Two gates are set on transitions in band 5 from 1149 keV to 1450 keV and one gate on transitions in band 1 from 849 keV to 1057 keV (except 972 keV).

A more-detailed investigation of these transitions was carried out to establish their intensities and to measure angular correlation information which would provide unambiguous information on the multipolarity of these transitions. In order to identify the multipolarity of the links, a series of spectra was produced and DCO analysis performed as described in Section 2.5.1. By using this method and different combinations of gates, a series of matrices was produced emphasising the lower and higher γ-ray linking transitions with better statistics. The advantage of different gating-conditions is shown in Figure 4.22.(a,b). As mentioned previously, the lower energy γ-ray linking transitions (e.g the 1380 keV) are stronger because gates on band 2 extended down to the 999 keV transition whilst the higher γ-ray links are strengthened when gates on band 1 were extended up to 1057 keV. Additionally, using the above method but with different numbers and combinations of gates, statistically-better links at 1484 keV and 1532 keV can be obtained (see Figure 4.24).

Gamma-rays from the known ND states and known SD states were used as a calibration for the multipolarity measurements. Stretched electric dipole transitions were found to have a DCO ratio of 0.7 and the ratio for known stretched quadrupole transitions was found to be 1.0.

The results for the measurements of the links are shown in Figure 4.23, where the filled circles represent the known stretched electric dipoles from the ND states, and the filled squares denote known stretched electric quadrupole transitions. The dotted lines are the averages of these values, which are intended only as guidelines representing where the ratios for each might be expected to lie. The diamonds represent the ratios for the inter-band γ-ray linking transitions. The ratios calculated for the inter-band transitions lie close to the values for known stretched electric quadrupole transitions, suggesting that they are electric quadrupole (E2) transitions. The ratios for inter-band transitions are subject to larger experimental uncertainties; however, they clearly correspond more closely to the values observed for known stretched electric quadrupole transitions.

The measurements confirm the relative spins and parity assignments for bands 1 and 2 in agreement with previous work.

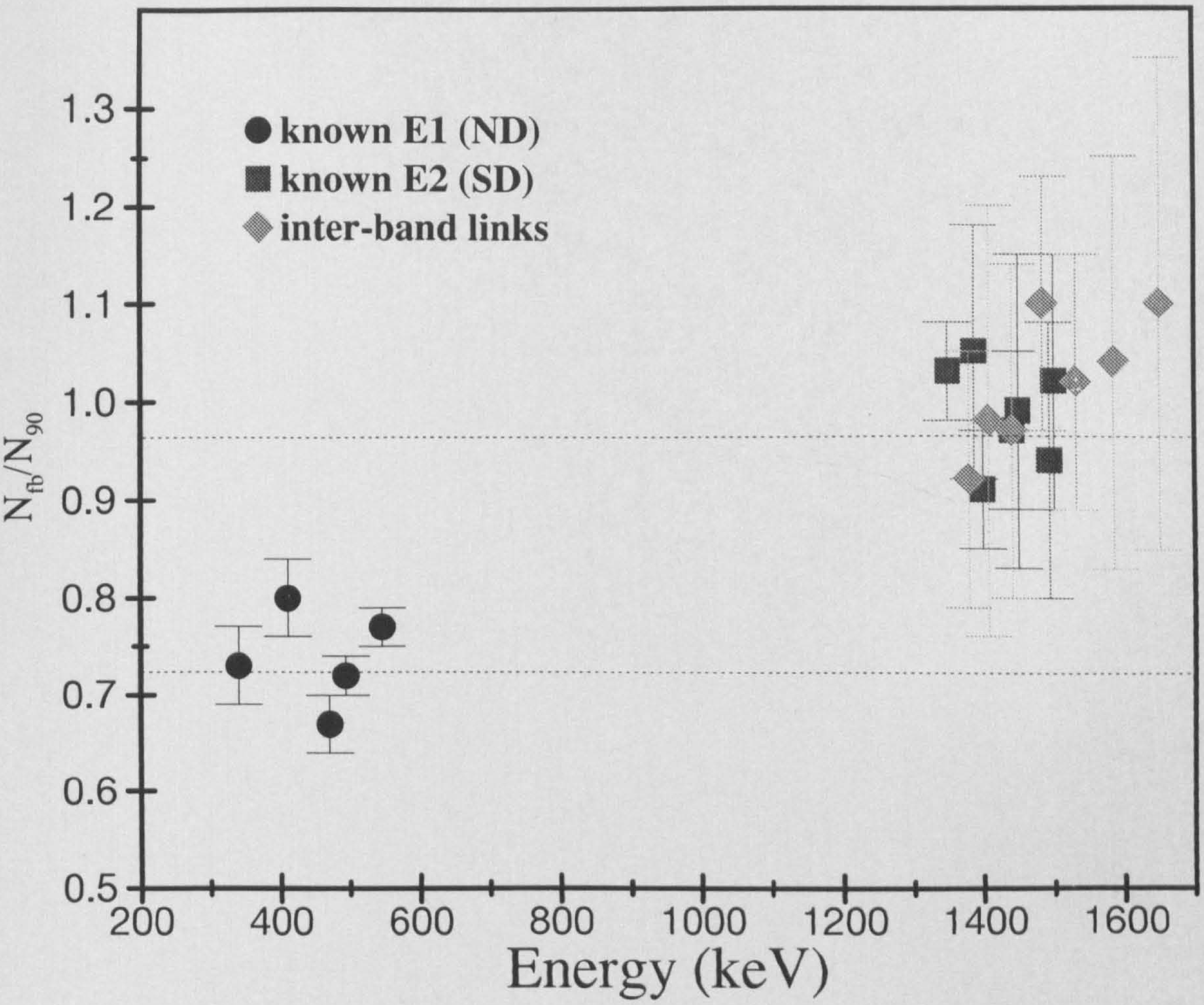

Figure 4.23: Ratios of intensities seen in detectors at forward and backward angles to the intensities seen in detectors close to 90° to the beam axis.

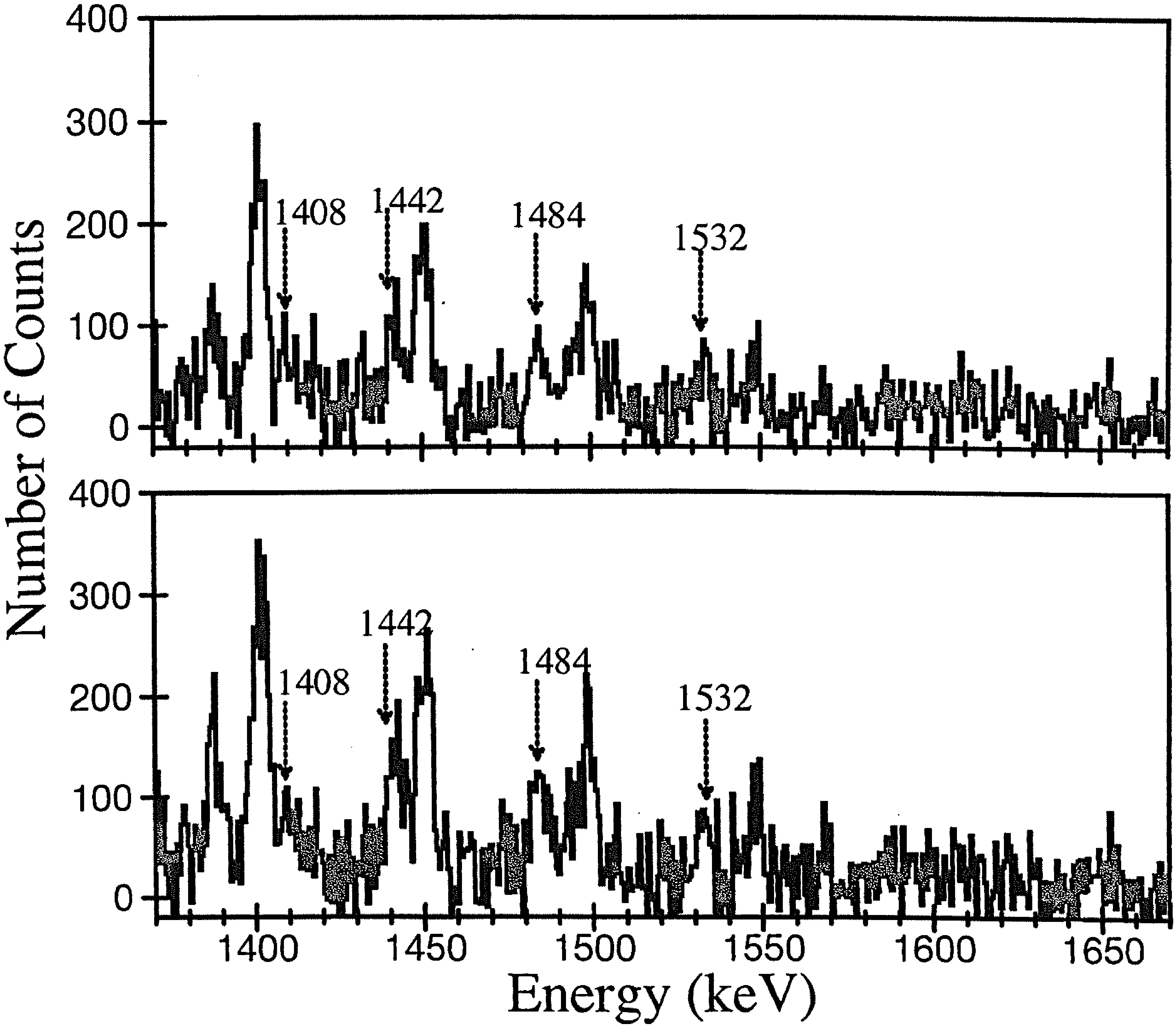

Figure 4.24: Spectra of SD band 2 in ^{150}Gd showing linking transitions to SD band 1. (top picture) Two gates are set on transitions in band 1 from 815 keV to 1014 keV (except 972 keV) and two gates are set on transitions in band 2 from 1200 keV to 1450 keV in the sorting process. (bottom picture) Two gates are set on transitions in band 1 from 815 keV to 1057 keV and two gates on transitions in band 5 from 1149 keV to 1450 keV.

4.3.2 Branching Ratio and Intensity Measurements

The multipolarity of the γ-ray linking transitions has been identified as E2. The inter-band E2 transitions are very fast compared to typical E2 transitions occurring between single particle (s.p) states in nuclei [Sz83]. The reduced transition probability B(E2) for an electric quadrupole transition is defined as

$$B(E2) = \frac{5}{16\pi} Q_o^2 \langle IK20|I-2K\rangle^2 \tag{4.2}$$

where Q_o is the quadrupole moment of the nucleus; the value of K can vary according to which levels near the Fermi surface are occupied.

After introducing the B(E2), the transition rate T of a γ-ray is defined as

$$T = 1.225 \times 10^9 E_\gamma^5 B(E2)$$

By using this information, the branching ratio of the reduced transition-probability B(E2) from a particular state can be expressed as

$$\frac{B(E2)_{int.b}}{B(E2)_{in.b}} = \frac{E^5_{\gamma(in.b)}}{E^5_{\gamma(int.b)}} \frac{I_{\gamma(int.b)}}{I_{\gamma(in.b)}} \tag{4.3}$$

where $B(E2)_{int.b}$ is for the inter-band transition and $B(E2)_{in.b}$ is for the in-band transition. $E_{\gamma(in.b)}$ and $I_{\gamma(in.b)}$ are the energy and the intensity for the in-band transition respectively. $E_{\gamma(int.b)}$ and $I_{\gamma(int.b)}$ are the energy and the intensity for the inter-band transition respectively. As illustrated in the above equation, the quadrupole moments and other coefficients cancel out because the quadrupole moment values of band 2 (16.8 eb) and band 1 (17.0 eb) [Bea98] are very close.

In order to use equation (4.3) and find the B(E2) value for the inter-band transition, the relative intensities of the E2 transitions were measured. To obtain accurate measurements for these, it was necessary to produce spectra in which the contamination was reduced as much as possible. Therefore, a series of three gated 1-D spectra was produced by setting gates at the top of band 2: for example, to measure the intensity ratio of I(1532)/I(1149), gates were set on band 2 from 1200 keV up to 1500 keV; to measure other intensity ratios, the number of gates was increased. In the case of I(1408)/I(999), gates were set from 1047 keV to 1500 keV on band 2. After obtaining the necessary spectra, intensity measurements were undertaken. The transition-probability of inter-band γ-ray linking transitions between bands 1 and 2 were deduced from the results of these measurements and are listed in Table 4.7.

Each linking transition carries $\approx$ 5 % intensity; hence, the total intensity lost via these links is $\approx$ 25-30 %, which is consistent with the relative intensity plot (see Figure 4.21) of bands 1 and 2, because band 1 builds up to $\approx$ 25-30 %, intensity.

Inter-band Energies (keV)	B(E2) W.u
1408	26.45 ± 5.5
1441	32.06 ± 5.5
1484	33.28 ± 5.6
1532	35.13 ± 5.6

Table 4.7: Transition probabilty of γ-ray linking transitions between bands 1 and 2.

After observation of the links between bands 1 and 2, the relative excitation energy of bands 1 and 2 can be established as seen in Figure 4.25.

It is also useful to plot aligned spin relative to the yrast SD band in ^{150}Gd (see Figure 4.26). This figure shows that there is a loss of $4\hbar$ at the backbend (0.5 MeV frequency), which is interpreted as an interaction with the band involving a pair of N = 6 quasi-particle protons with an interaction strength of $\approx$ 41 ± 1 keV in agreement with the previously-predicted value ($\approx$ 40) [Tw94]. This interpretation is supported by Cranked Shell Model calculations, which show the existence of pairing correlations due to the N = 3 and N = 6 proton levels, both lying together at the Fermi surface. There is another example of a two proton excitation involving the same N = 3 and N

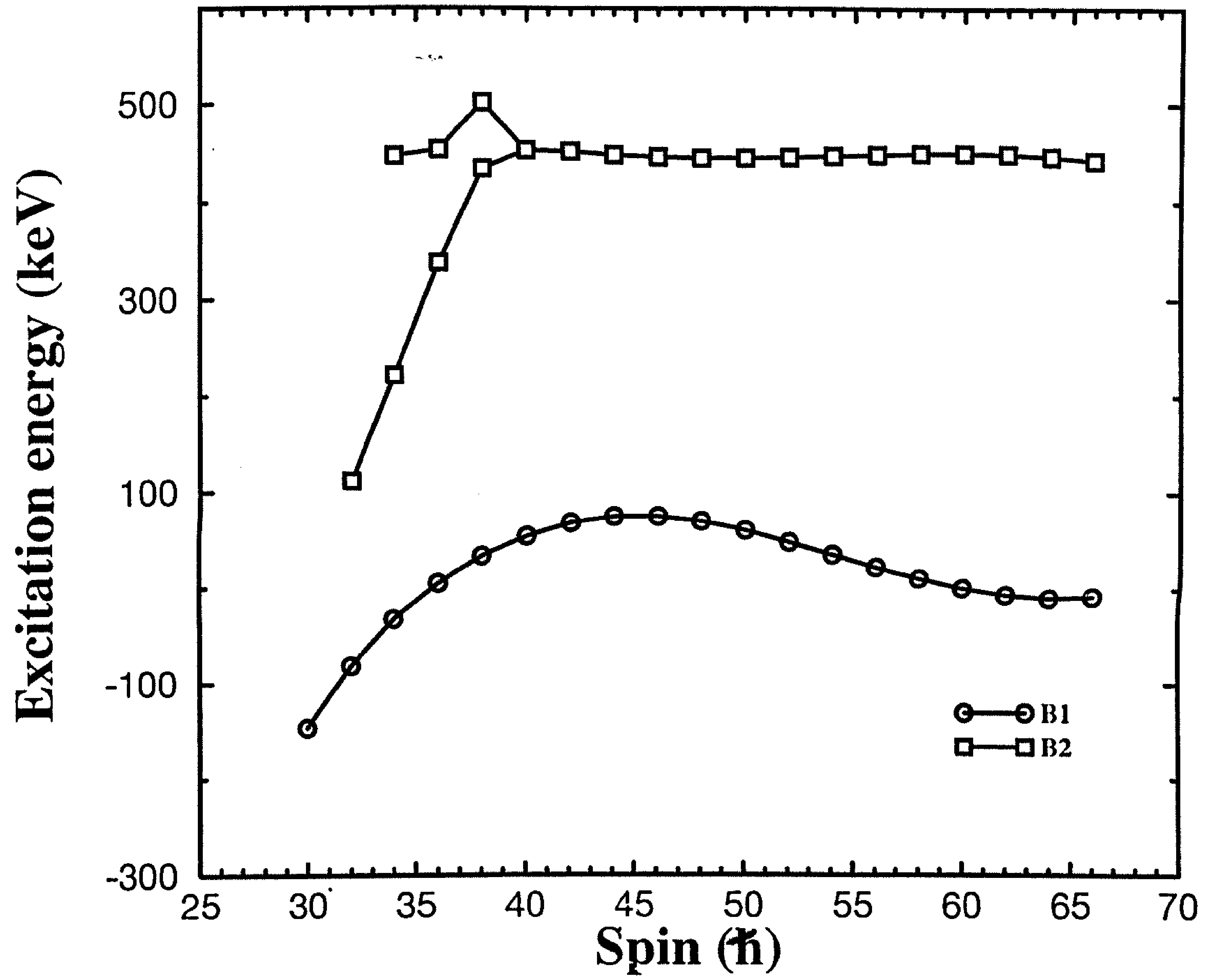

Figure 4.25: Relative excitation energy versus spins for band 2 and band 1 in ^{150}Gd.

– 6 orbitals in ^{149}Gd where band 5 has similar $\mathcal{J}^{(2)}$ to the yrast band in ^{152}Dy [Fl93]. Band 5 in ^{149}Gd also involves a neutron excitation from one of the [642]5/2, [651]1/2 or [411]1/2 orbitals into the (N = 7) [770]1/2 orbital. However, band 5 in ^{149}Gd does not show a backbend as band 2 in ^{150}Gd does.

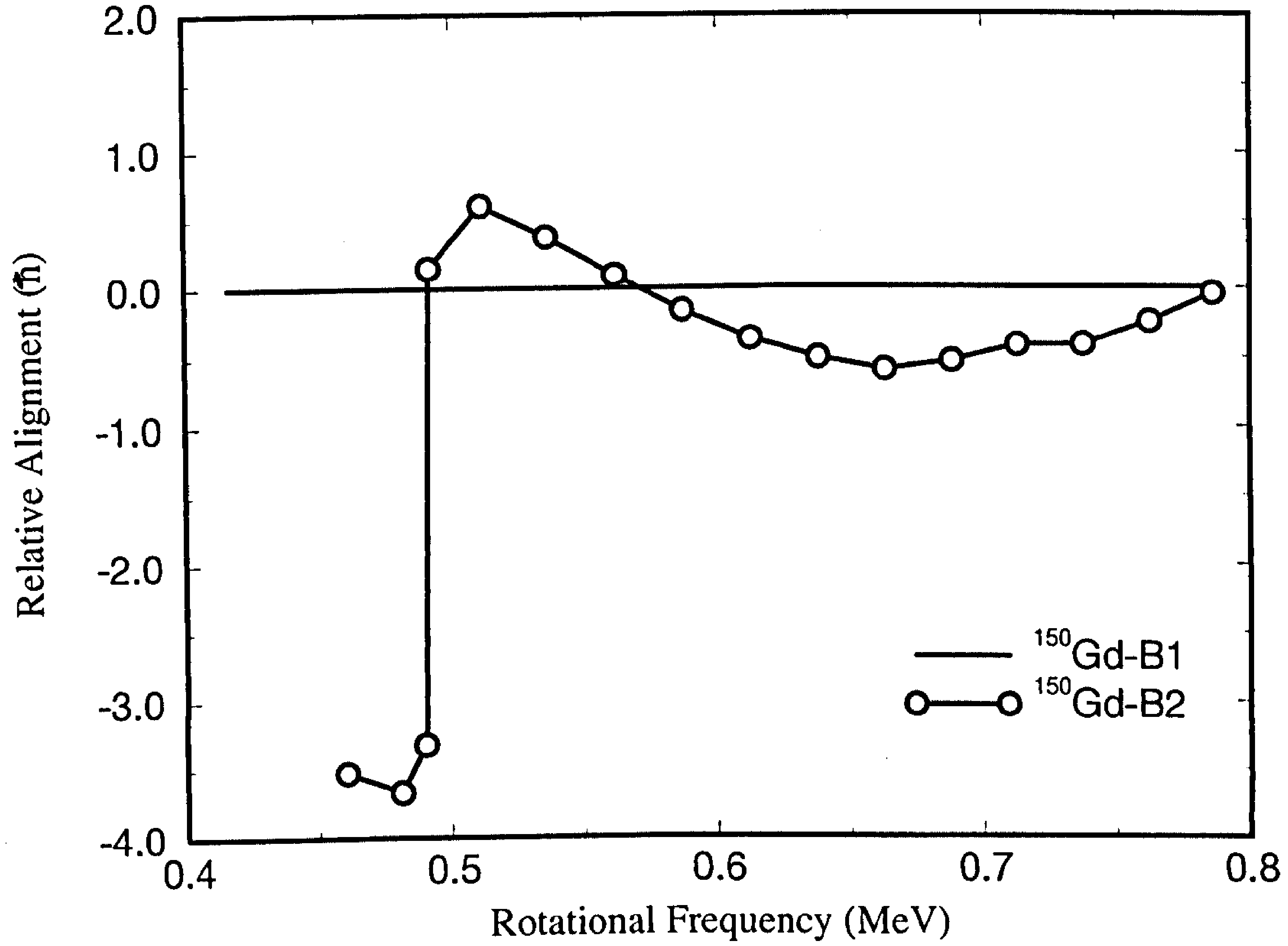

Figure 4.26: Relative alignment versus rotational frequency for band 2 and band 1 in ^{150}Gd.

4.4 Linking transitions between Bands 3 and 4a

A crossing may occur between bands in the same nuclei; if the interaction is sufficiently strong, bands with the same parity and signature will interact at such a crossing and may cause a disturbance in the energies of the former. The first identification of such an SD band interaction was observed by the simultaneous disturbance to the energies of two SD bands (bands 3 and 4a) in ^{150}Gd around 53 $\hbar$ and 55 $\hbar$ [Bea93]: this was the first observation of accidental degeneracy between SD states. A careful examination of the γ-rays of bands 3 and 4a shows that the γ-ray in band 3 of energy 1273.4 keV ($55^- \rightarrow 53^-$) is shifted down in energy by 4.8 keV from its expected position, while the transition in band 4a of energy 1377.3 keV ($55^- \rightarrow 53^-$) (see Figure 4.27) is correspondingly 4.6 keV higher in energy than expected from the average energy spacing in the bands. The adjacent transitions ($57^- \rightarrow 55^-$) and ($53^- \rightarrow 51^-$) in bands 2 and 4a are also shifted slightly from their expected positions by an average of 1 and 2 keV respectively. This observed shift in γ-ray energies can be explained by an interaction between levels of the same spin and parity in bands 3 and 4a.

Figure 4.27 shows a partial level scheme for bands 3 and 4a in the interaction region. The arrows indicate the direction in which a particular level has been perturbed. At high spin, the transition energies in band 3 are approximately 100 keV smaller than those in band 4a. It was proposed [Bea93] that the 55^- and 53^- states in band 3 lie between the 55^- and 53^- states in band 4a, and, as a result of this, levels are pushed closer together by the interaction, which gives a smaller transition energy than expected. On the other hand, the opposite occurs in band 4a where the levels are drawn further apart for the corresponding levels.

The interaction strength $|V|$ between two levels is given by the simple expression

$$|V| = \frac{1}{2}\sqrt{\Delta e^2 - \Delta e_\circ^2} \tag{4.4}$$

where Δe^2 and $\Delta e_\circ^2$ are the perturbed and unperturbed energy level separations, respectively.

The measured shifts in the transition energies for the 53^- and 55^- levels in band

3 and band 4a are 46.1 and 59.6 keV respectively. In band 3, levels 53^- and 55^- are separated by 46.1 and 50.8 keV; therefore, the interaction strength between these levels is $|V| = 11 \pm 1$ keV. In the case of band 4a, these levels are separated by 55.7 and 59.6 keV, so the interaction strength between these levels is $|V| = 11 \pm 1$ keV.

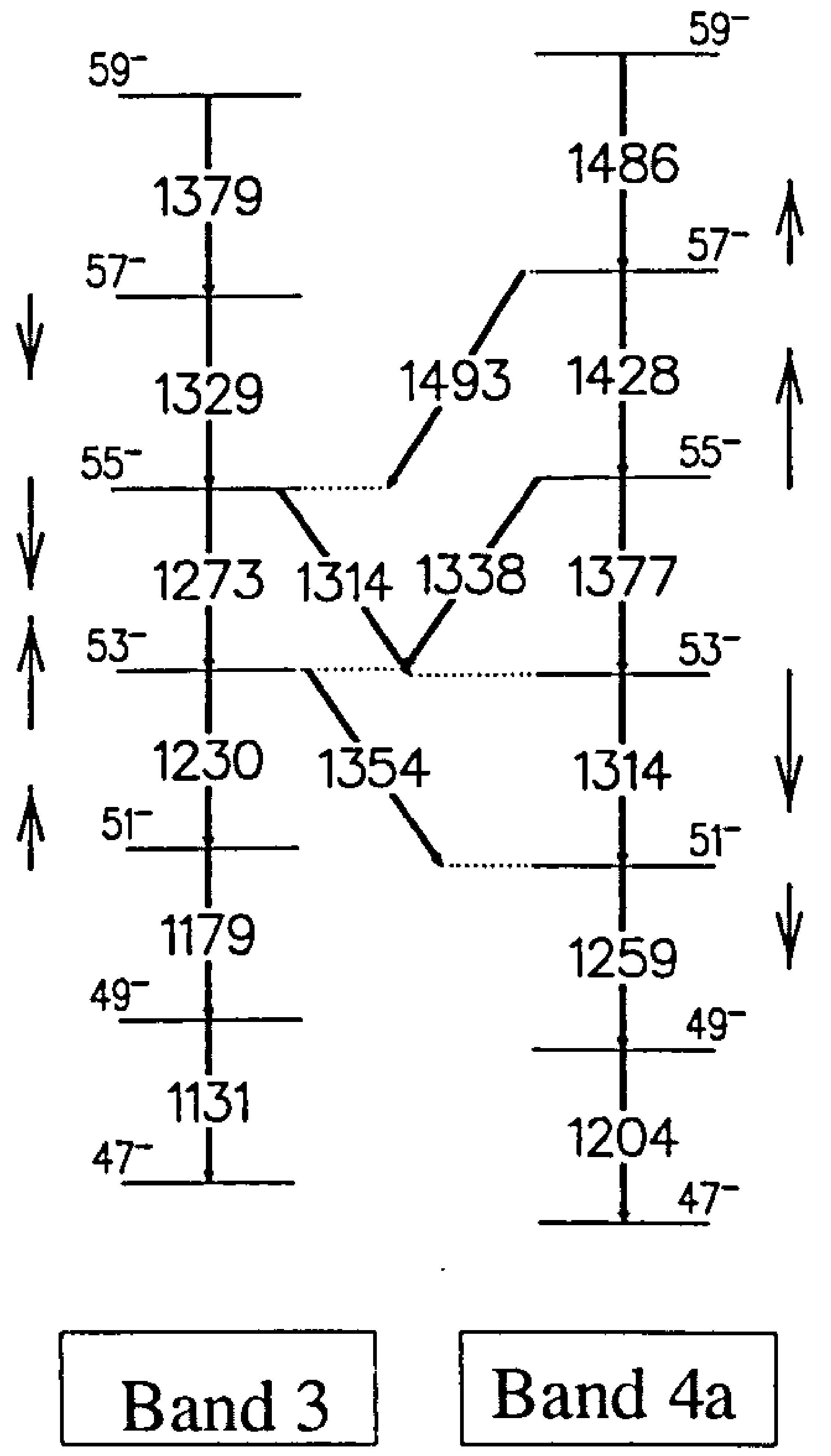

Figure 4.27: Partial level scheme of SD band 3 and band 4a in ^{150}Gd , showing the linking transitions between the bands in the region of the interaction. An arrow alongside a shifted level indicates the direction and magnitude by which it has been perturbed. Observed linking transitions are shown by solid lines with their energy value.

The wave-functions of the nuclear states are mixed by the interaction between bands 3 and 4a. The 55^- and 53^- levels undergo the highest degree of mixing for a constant interaction strength of ≈ 10.6 keV. The adjacent levels will exhibit much less mixing as they are an additional 100 keV further apart in energy. It was found that the amplitude of the admixture was ~ 26 % for the 53^- states and $\sim 17\%$ for the 55^- levels. As a result of level mixing in the interaction region, E2 cross-band linking transition between bands 3 and 4a are predicted [Bea93] to compete with the in-band E2 transitions. This prediction is confirmed by this present work and linking cross-band transitions have been observed (to be discussed in the next section); the predicted cross-band transitions are close to the observed transitions within 2-10 keV (see Figure 4.27). The cross-band transitions are expected to be stronger from band 3 to band 4a than vice versa due to the E_γ^5 dependence (the E2 strength is proportional to E_γ^5).

4.4.1 Investigation of Links

A cross-band transition between bands 3 and 4a has been identified from a spectrum generated by setting three gates on band 4a from 835 keV to 1042 keV transitions (with the exception of 991 keV to avoid possible contamination from band 3 since the 991 keV transition is identical to this γ-ray in band 3). The 1314 keV transition is a link from SD band 3 to SD band 4a and is also a member of SD band 4a. The spectrum of SD band 4a showing 1314 keV linking transitions is illustrated in Figure 4.28. The dotted line shows the normal intensity profile of band 4a. As can be seen from this spectrum, there is more intensity in the 1314 keV transition than in any other higher member of band 4a. This can be proven by putting a single gate on the 1314 keV transition: as seen in the inset picture in Figure 4.28, the 1314 keV is in coincidence with itself. The 1329 keV γ-ray belongs to band 3 and holds $\approx 20\%$ intensity while the linking transition 1314 keV carries $\approx 22\%$ intensity of that of the SD transitions in band 4a.

Further investigation was carried out in order to confirm the crosstalk between bands 3 and 4a and to find more linking transitions from band 3 to band 4a. The spectrum shown in Figure 4.29 was obtained by setting two gates on band 3 from 1379 keV to 1588 keV and two gates on band 4a from 835 keV to 1205 keV (except 989, 1096 and 1149 keV transitions in order to avoid contamination). By using this gate condition, one more link (1354 keV) was observed from band 3 to band 4a. Figure 4.29 shows this linking transition and also the members of bands 4a and 3.

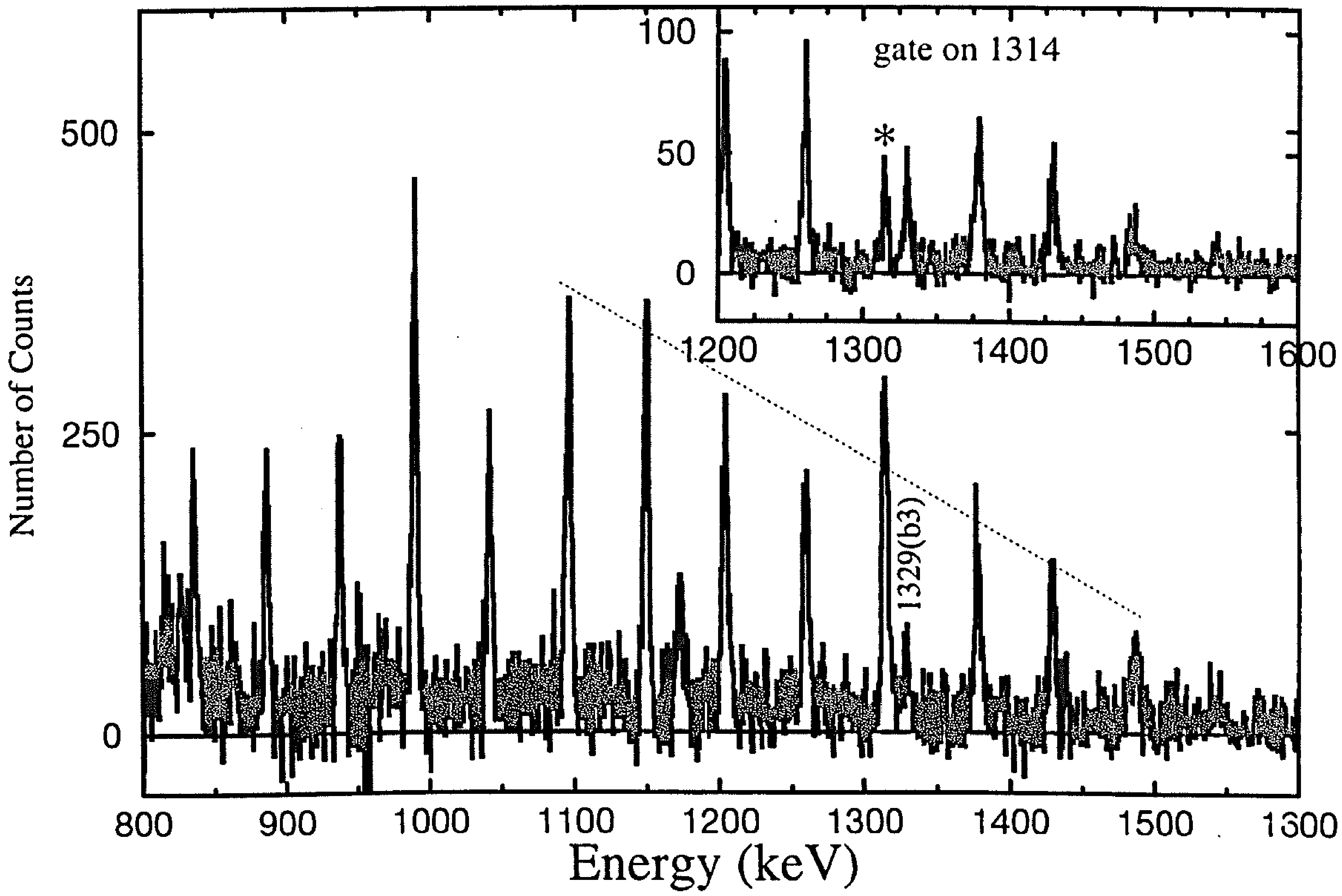

Figure 4.28: Spectrum of SD band 4a in ^{150}Gd showing the linking transition from SD band b3 to SD band 4a. Two gates are set on transitions in band 4 from 835 keV to 1042 keV (except 991 keV). The inset is the single gate on the 1314 keV transition, as seen, it is a doublet and a link from band 3 to band 4a. Note the anomalously-high intensity of the 1314 keV transition.

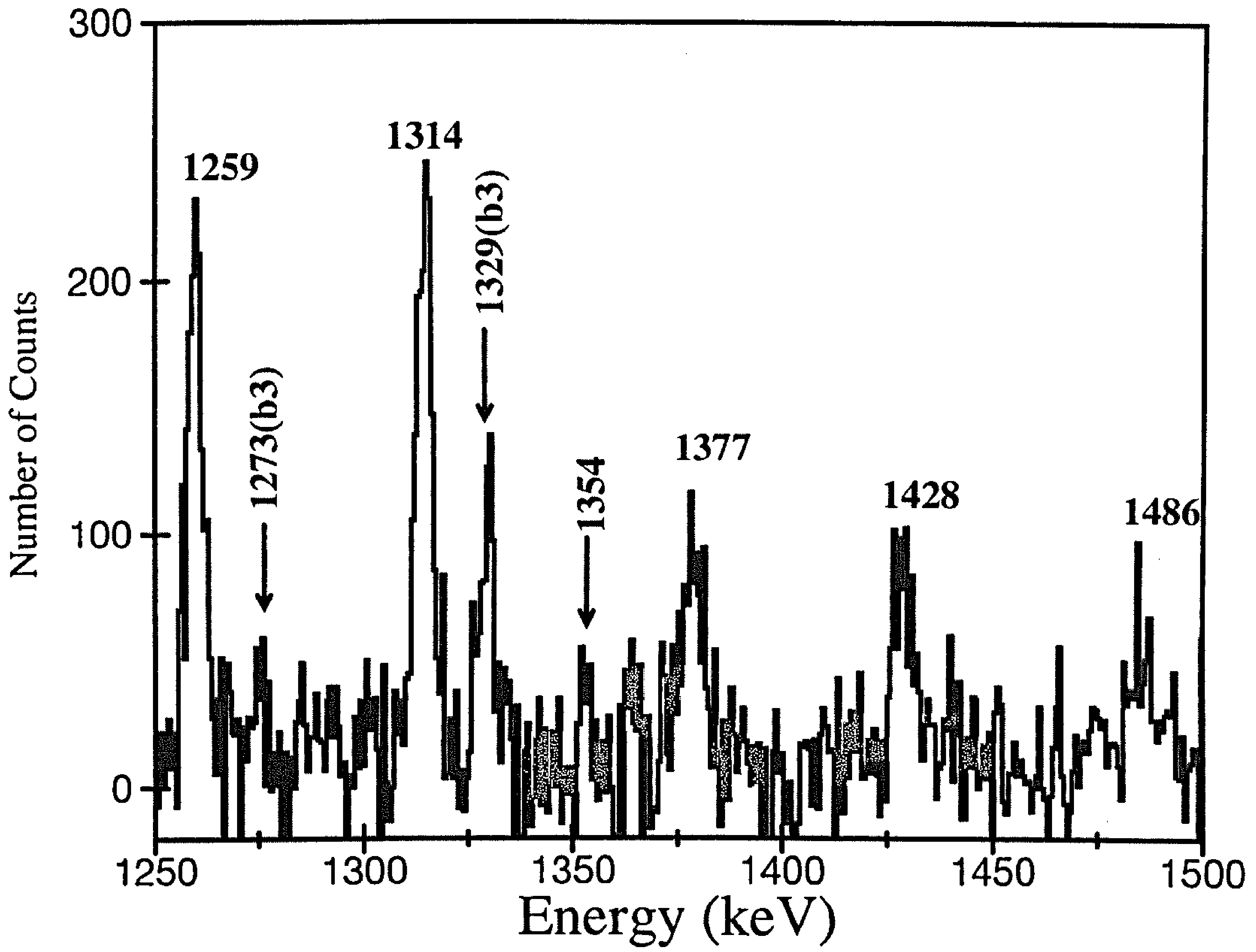

Figure 4.29: The spectrum of SD band 4a in ^{150}Gd showing the linking transition (1354 keV) from SD band 3 to SD band 4a. Two gates are set on transitions in band 4a from 835 keV to 1205 keV (except 989 keV,1096 keV,1150 keV transitions) and two gates on transitions in band 3 from 1379 keV to 1588 keV.

Using the same sorting method, more investigation was carried out to find links from band 4a to band 3. The spectrum was produced by setting two gates on band 3 from 858 keV to 1231 keV (excepting the 991 keV transition, for the same reason as stated above) and two gates on band 4a from 1486 keV to 1658 keV (shown in Figure 4.30). From this sorting, two cross-band transitions (1338 kev and 1493 keV) were observed. Figure 4.30 shows these links with band 3 transitions labelled.

The links from band 3 to band 4a and from band 4a to band 3 are shown in a partial level scheme of these two bands (see Figure 4.27).

In order to identify the multipolarity of the cross-band linking transitions, the

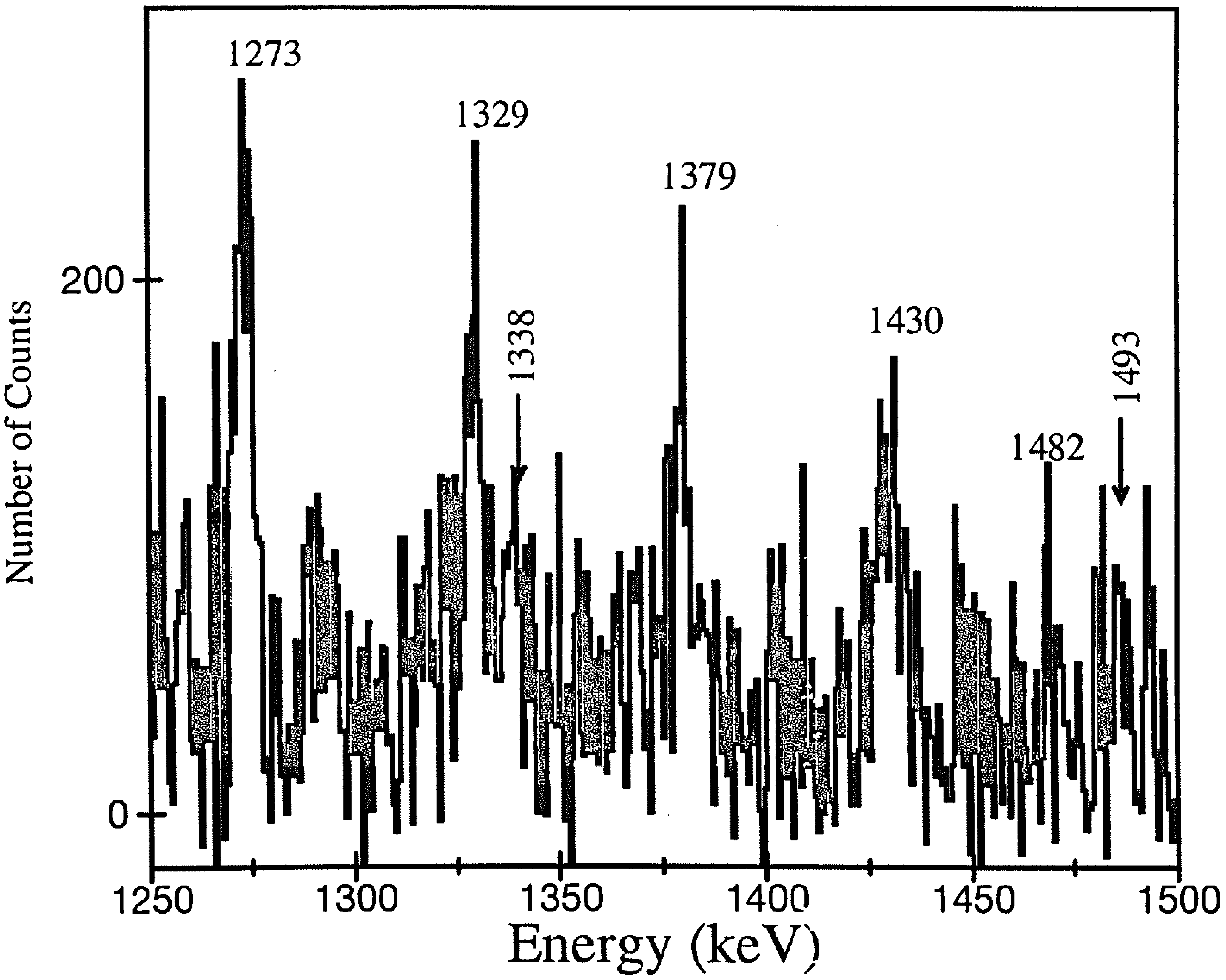

Figure 4.30: Spectrum of SD band 3 in ^{150}Gd showing linking transitions from SD band 4a to the SD band 3. A two-gate condition is set on transitions in band 3 from 858 keV to 1231 keV (except 991 keV) and another one on transitions in band 4a from 1486 keV to 1658 keV.

DCO method was used (as described in Section 2.5.1). The results of this procedure are shown in Figure 4.31: the filled circles represent the known stretched electric dipoles from the ND states and the filled squares represent known stretched electric quadrupole transitions. The diamonds represent ratios for the inter-band γ-ray linking transitions. The broken lines are the averages of these values, which are intended only as guidelines representing where the ratios for each are expected to lie. The ratios calculated for the cross-band transitions clearly lie close to the values for known stretched electric quadrupole transitions, suggesting that they are indeed electric quadrupole (E2) transitions. The ratios for cross-band transitions are subject to larger experimental uncertainties, but still correspond closely to the values observed for known stretched electric quadrupole transitions.

4.4.2 Branching Ratio and Intensity Measurements

The multipolarity of cross-band transitions was identified using the DCO method. Relative intensity measurements were performed in order to find the branching ratios. In order to obtain accurate measurements for these relative intensities, a series of spectra was produced. To measure the relative intensity of the 1314 keV γ-ray , a spectrum was obtained from the sum of double gates on transitions between the 1273 keV to 1588 keV. The intensity of band 3 was measured in this spectrum up to the 1274 keV transition, which is parallel to the 1314 keV cross-band transition. A second spectrum was produced as above but with gates from 1329 keV to 1588 keV and one gate on the 1314 keV transition; this spectrum gave a double intensity of the 1314 keV transition as this transition is also in band 4a. From these two measurements, the ratio $I_\gamma(1314)/I_\gamma(1273)$ was found to be (22 ± 3.8) %. This is in agreement with the other measurements which were obtained from the spectrum which is shown in Figure 4.28 (two gates were on band 4a from 835 keV to 1042 keV). In this case, the intensity of the higher energy transitions was measured in band 4a but the 1314 keV transition was left out of the intensity plot and the rest of them were fitted using a quadratic fit to find the true intensity of the 1314 keV in band transition. This real intensity of the 1314 keV in band transition was subtracted from the total measured intensity of the 1314 keV transitions; the left-over intensity (22.08 ± 2.3) % gives the intensity of the cross-band transition from band 3 to band 4a. The intensity of the other cross-band transition (the 1354 keV) was too weak to measure accurately, but it represents $\approx$ 3 %.

By using the same method but with a different spectrum, the intensity ratio of $I_\gamma(1338)/I_\gamma(1377)$ was measured and found to be (9.50 ± 0.6)%. The intensity of the other cross-band transition (1493 keV) was difficult to measure due to the weak nature of the transition.

After obtaining the intensity ratios, B(E2) values were calculated for cross-band trasitions and they are listed in Table 4.8.

Inter-band Energies (keV)	B(E2) W.u
1314	441 ± 9
1338	160 ± 8

Table 4.8: Transition probability of γ-ray linking transitions between bands 3 and 4a, and bands 4a and 3.

After this observation of the cross-band linking transitions between bands 3 and 4a, the relative excitation energy of bands 3 and 4a and also of band 4b can be established (see Figure 4.32). The crossing point of bands 3 and 4a was placed approximately 700 keV above the yrast band. This is not an absolute value; it was chosen to ensure that bands 4a and 4b did not become yrast at any spin. However, from this, band 3 would become yrast at 70 $\hbar$.

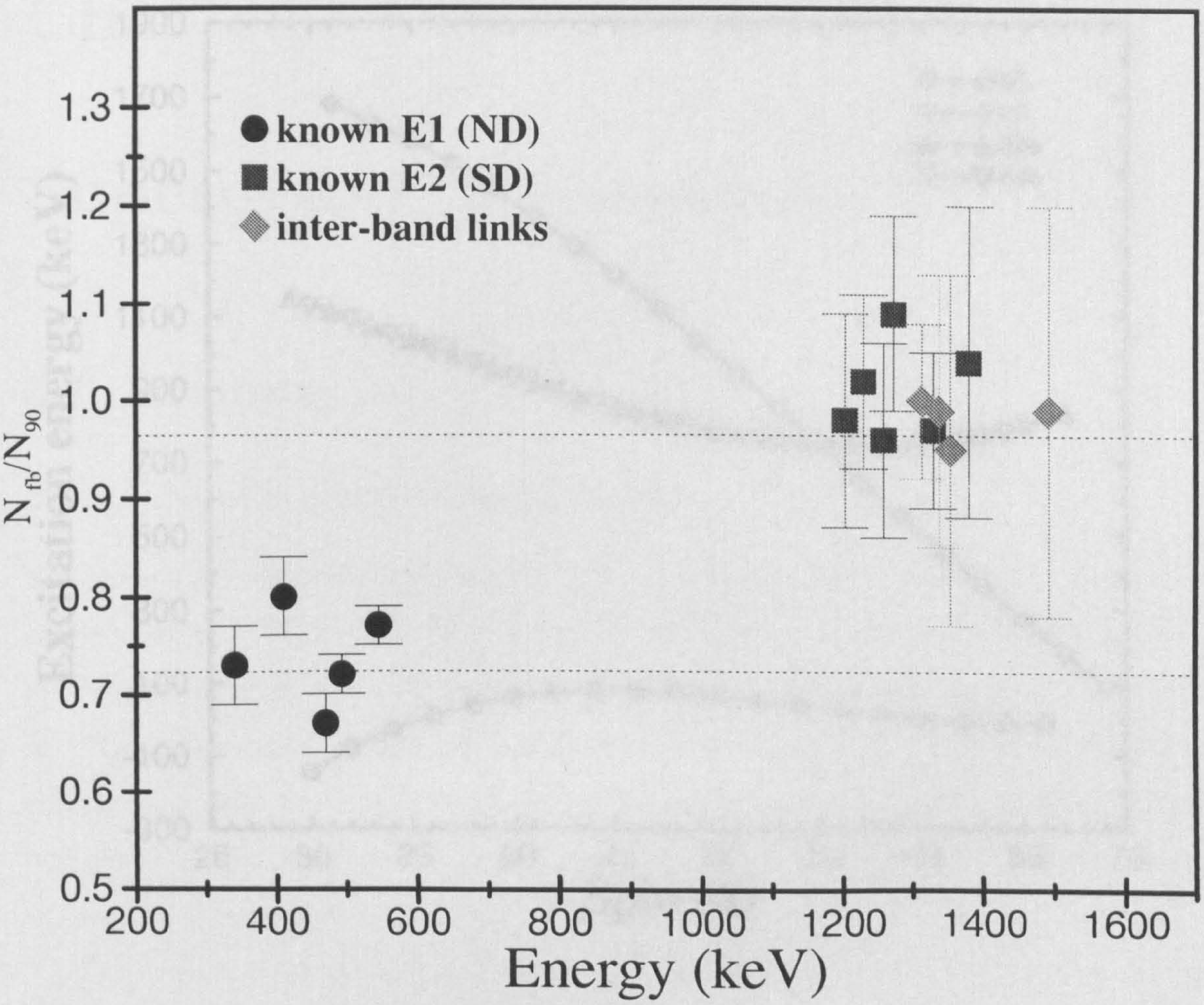

Figure 4.31: Ratios of intensities seen in detectors at forward and backward angles to the intensities seen in detectors close to 90° to the beam axis.

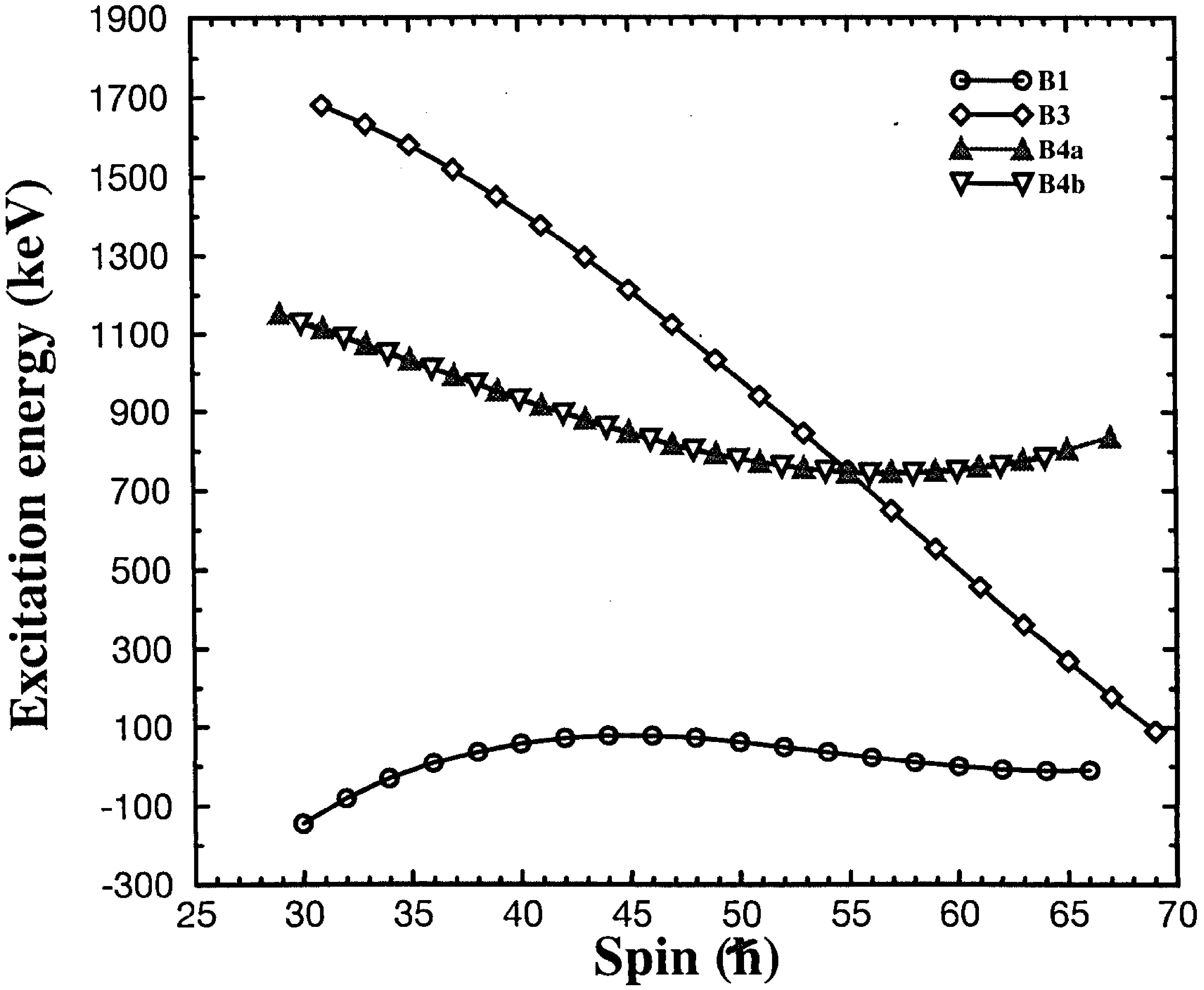

Figure 4.32: Relative excitation energy of bands 3, 4a, 4b and band 1 versus rotational frequency in ^{150}Gd.

Chapter 5

Superdeformed bands in ^{151}Gd

5.1 Results

5.1.1 New Superdeformed bands in ^{150}Gd

The same automatic SD bands search as that performed for ^{150}Gd (in Chapter 4) was carried out for ^{151}Gd. This resulted in the identification of six rotational cascades of γ-rays typical of SD structures. This is the first observation of such structures in ^{151}Gd. These newly-observed bands have been assigned to ^{151}Gd on the basis of coincidences with the low lying states in ^{151}Gd. The close relationship in transition energies between these bands and those in neighbouring nuclei has been used to suggest configurations.

The spectra of the six new SD bands in ^{151}Gd , observed in this work and presented in Figures 5.1 and 5.2, are generated in a similar way to that described in Chapter 4.

The transition energies and associated errors of the six SD bands in ^{151}Gd are given in Table 5.1, which also provides details of the transition energies and associated errors of the six SD bands in ^{151}Gd.

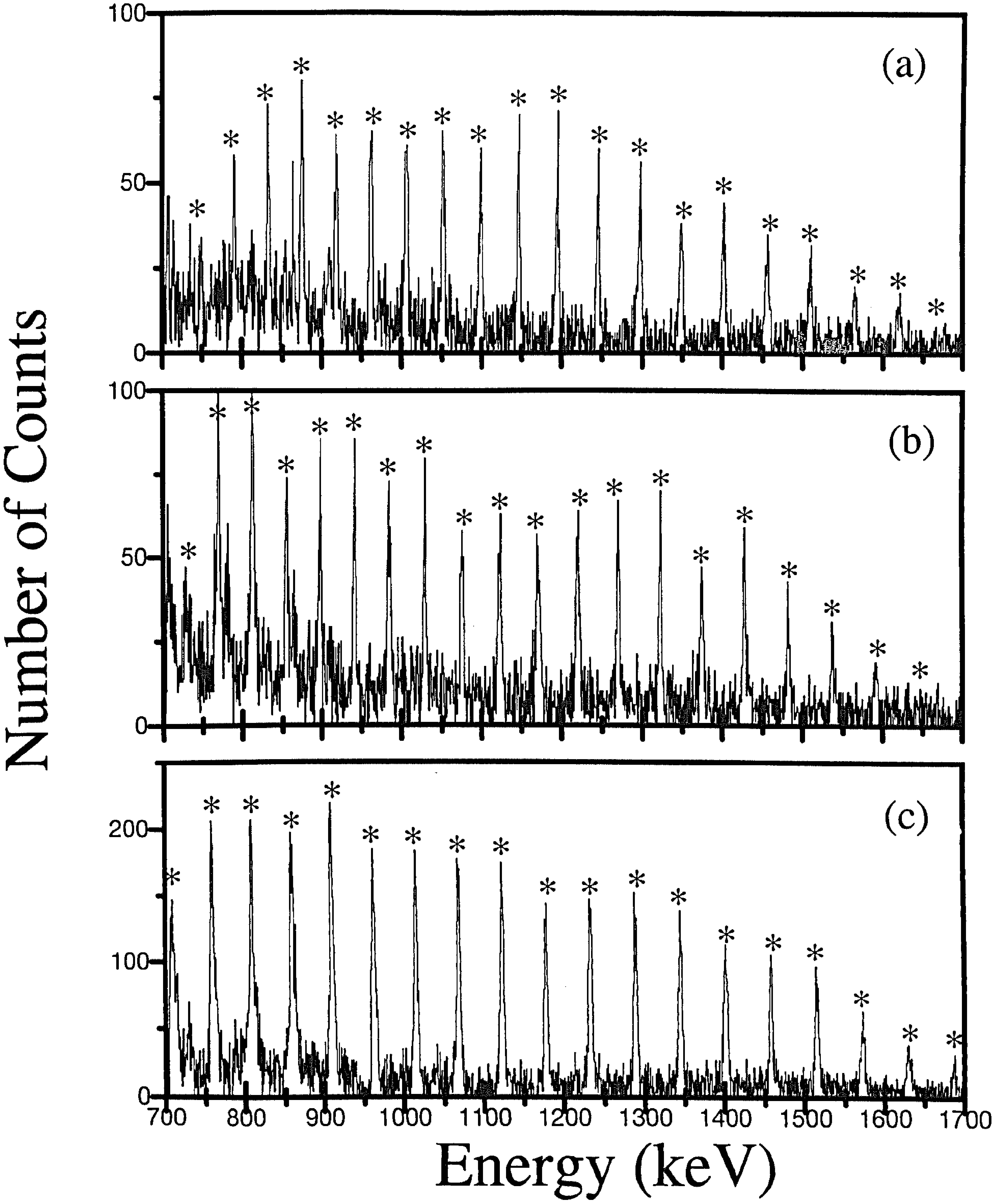

Figure 5.1: Background subtracted quadruple gated spectra of (a) band 1a, (b) band 1b, (c) band 2 in in ^{151}Gd.

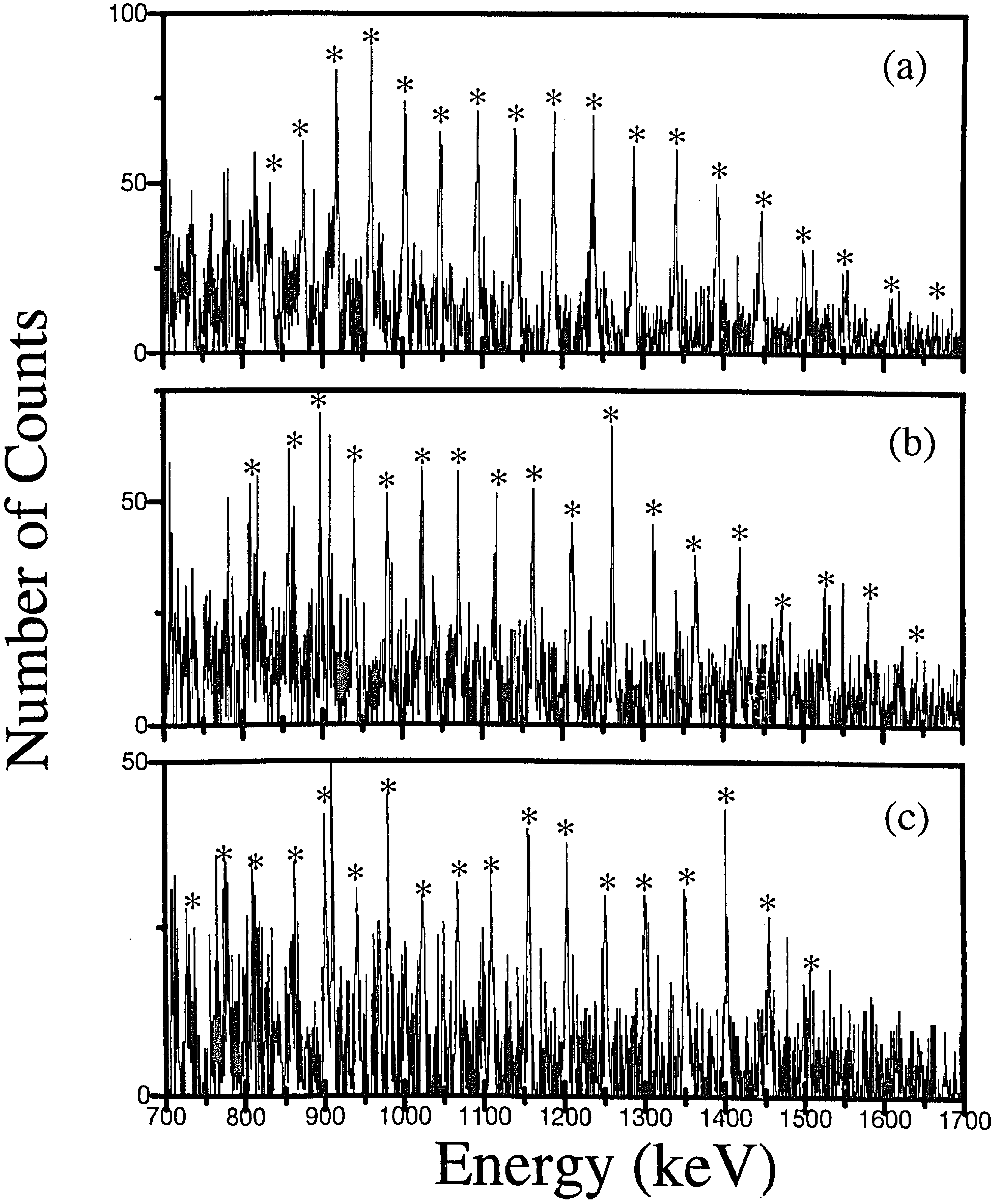

Figure 5.2: Background subtracted quadruple gated spectra of (a) band 3a, (b) band 3b, (c) band 4 in in ^{151}Gd.

Transition Energies (keV)					
B1a	B1b	B2	B3a	B3b	B4
746.4(8)	725.5(8)	755.7(4)	832.8(6)	808.6(4)	817.8(7)
788.9(4)	768.4(5)	805.6(4)	874.0(4)	854.2(4)	860.0(13)
831.3(4)	810.5(9)	855.9(9)	915.8(5)	895.3(6)	899.8(5)
873.5(3)	852.6(4)	906.8(8)	958.3(3)	937.5(3)	938.4(7)
916.3(3)	895.4(3)	958.7(7)	1000.9(4)	979.2(7)	978.5(4)
959.8(3)	938.7(3)	1012.0(5)	1045.9(3)	1023.9(4)	1021.2(6)
1004.2(6)	982.4(3)	1066.1(8)	1091.1(4)	1068.2(4)	1064.9(5)
1049.0(3)	1027.4(3)	1120.7(6)	1137.4(5)	1114.1(5)	1108.0(4)
1096.7(3)	1073.3(4)	1175.5(9)	1185.9(9)	1161.5(4)	1154.4(7)
1144.2(3)	1120.1(4)	1230.4(4)	1236.1(5)	1209.8(8)	1200.7(5)
1193.0(3)	1169.3(4)	1286.7(4)	1286.1(4)	1261.3(5)	1249.3(5)
1243.1(4)	1218.0(4)	1342.7(4)	1337.5(4)	1312.5(5)	1299.2(8)
1294.6(6)	1268.6(4)	1399.4(4)	1388.7(4)	1363.2(6)	1349.8(9)
1346.4(4)	1320.4(4)	1456.3(5)	1443.4(6)	1416.7(6)	1400.7(12)
1399.1(4)	1372.6(4)	1513.4(5)	1497.8(12)	1469.6(15)	1451.8(16)
1452.6(5)	1426.0(5)	1570.0(5)	1551.5(15)	1524.0(15)	1505.0(15)
1507.2(4)	1479.7(5)	1627.7(6)	1606.2(17)	1580.5(17)	1555.3(18)
1562.0(5)	1534.4(7)	1685.6(9)		1635.2(18)	
1617.0(7)	1589.5(10)	1742.9(11)			
1674.8(9)	1645.3(11)				
	1700.8(13)				

Table 5.1: Transition energies of SD bands 1-4 in ^{151}Gd obtained from the present work.

Relative Intensity Measurements

The same method which was used to measure the relative intensity of the SD bands in ^{150}Gd (as described in Chapter 4) was used to measure the relative intensities of the new SD bands in ^{151}Gd. Figure 5.3 shows the relative intensity of SD bands in ^{151}Gd. Again, plots are normalised to the plateau region, which is defined as 100%.

The absolute intensities of the SD bands in ^{151}Gd relative to band 1 in ^{150}Gd were measured using six gates on the plateau region of each SD band, thus allowing a direct comparison of the intensity of a 100% transition in each SD band in ^{151}Gd with that of band 1 in ^{150}Gd. It was found that the strongest SD band in ^{151}Gd has 13 % intensity relative to SD band 1 in ^{150}Gd. The results are listed for SD bands in ^{151}Gd in Table 5.2 as a percentage relative to band 1 in ^{151}Gd (normalised to 100%).

SD Bands	Intensity (%) Relative to Band 1
Band 1a	100 ± 2
Band 1b	92 ± 2
Band 2	85 ± 2
Band 3a	77 ± 2
Band 3b	54 ± 3
Band 4	38 ± 2

Table 5.2: The intensities of the SD bands (1-4) in ^{151}Gd relative to the yrast SD in ^{151}Gd .

5.1.2 Spin Assignments

Due to the similarities between the transition energies of the new bands in ^{151}Gd and neighbouring nuclei, the transition energy relationship method (as described in Section 5.1.2) was used to assign the spins of new SD bands in ^{151}Gd.

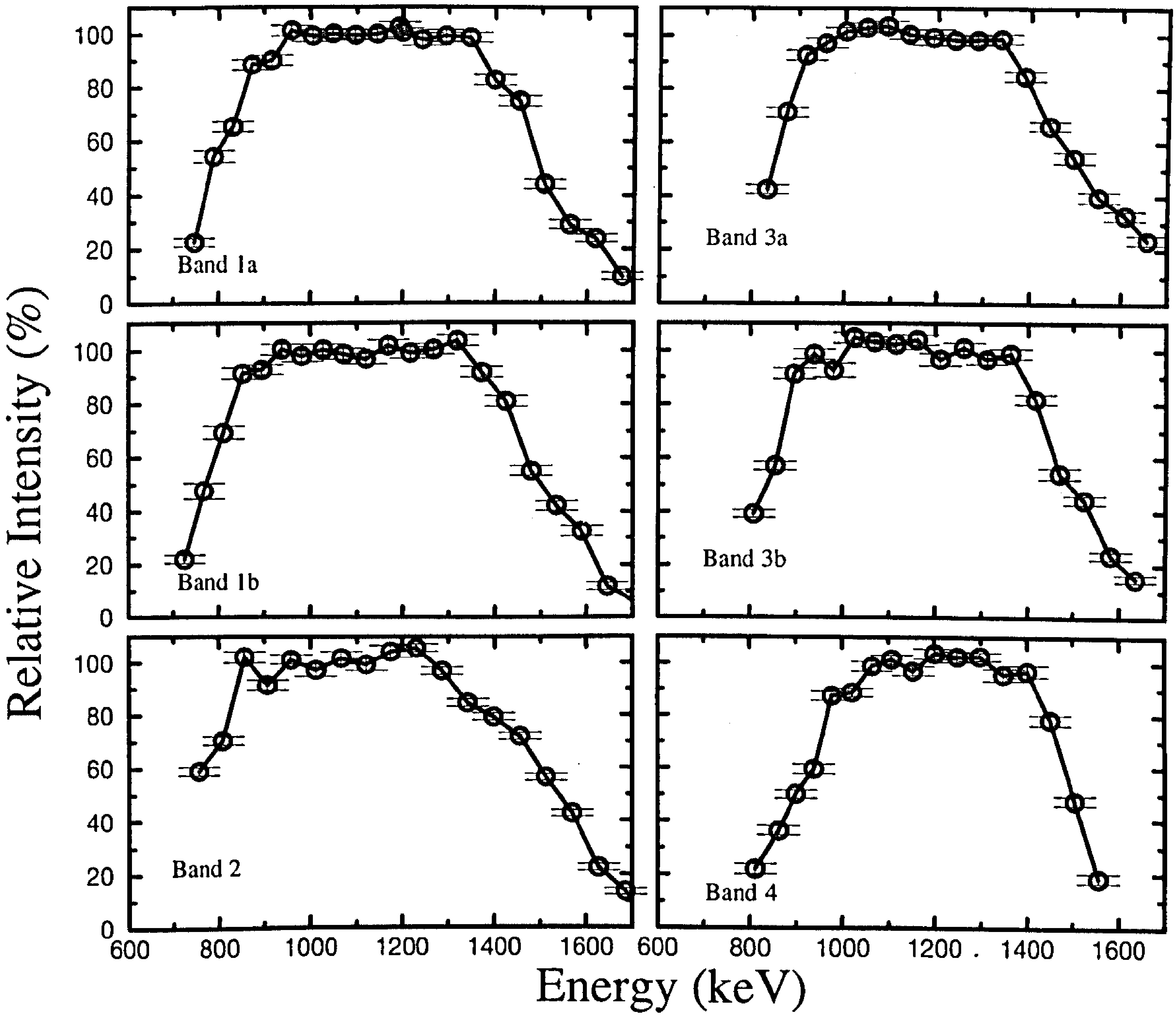

Figure 5.3: The relative intensity measurements for band 1a, band 1b, band 2, band 3a, band 3b and band 4 in ^{151}Gd. They have been normalised to the average intensity of the plateau region.

The level scheme's newly-observed SD bands in ^{151}Gd are shown in Figure 5.4.

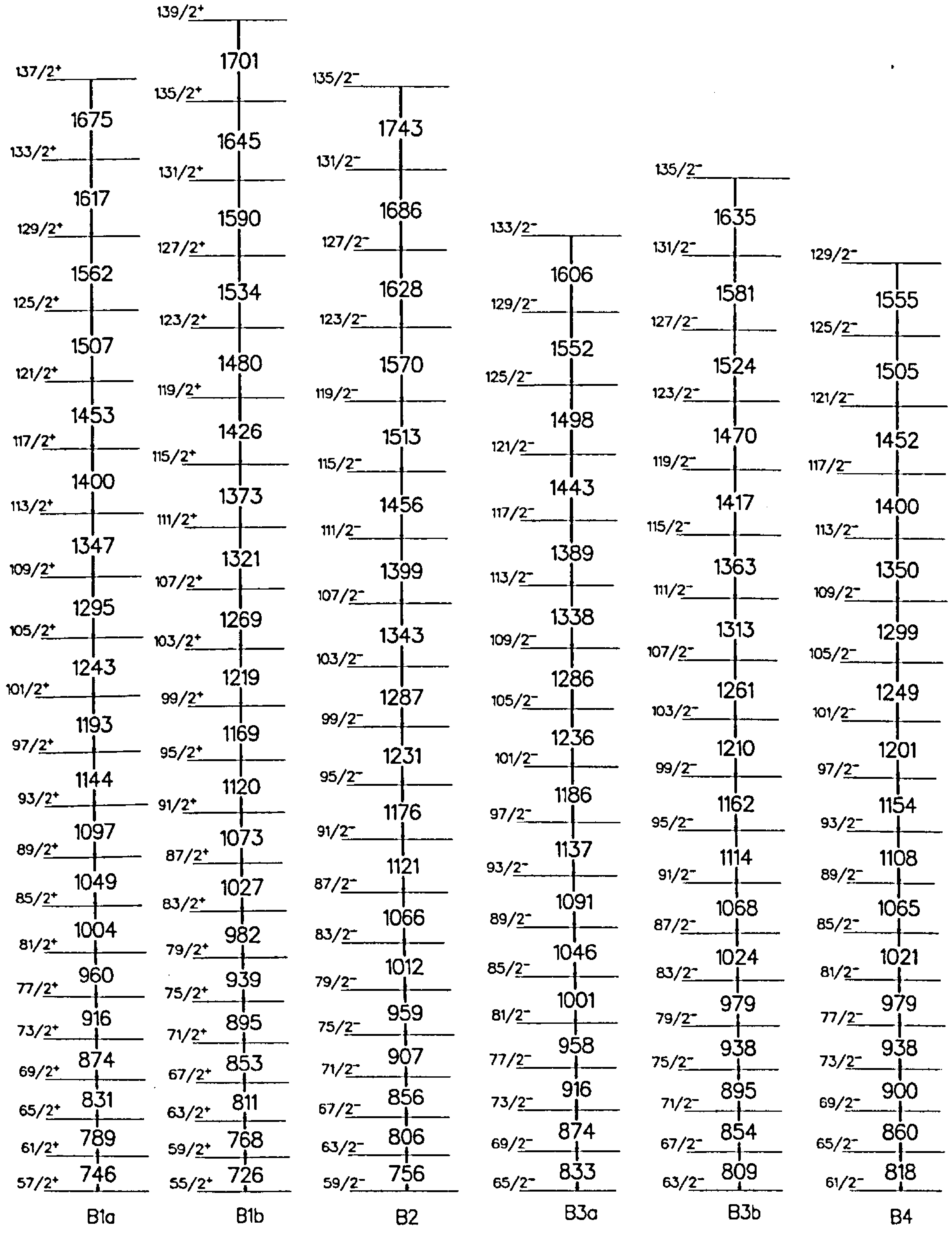

Figure 5.4: The partial level scheme of the six new SD bands observed in ^{151}Gd with their spin-values.

5.2 Discussion

5.2.1 Dynamic Moments of Inertia and high-N Configurations

Band 1a (B1a) and Band 1b (B1b)

The transition energies in band 1a appear to lie at the midpoints of transitions in band 1b, which indicates that these bands are signature partners based on an orbital which exhibits very little signature splitting as a function of rotational frequency. Furthermore, they have very similar moments of inertia: the dynamic moments of inertia $\mathcal{J}^{(2)}$ (see Figure 5.5) appear to be very similar to the $\mathcal{J}^{(2)}$ of the yrast SD band in ^{150}Gd , but the magnitude of $\mathcal{J}^{(2)}$ is smaller than that of the yrast SD band in ^{150}Gd. It also follows that the $\mathcal{J}^{(2)}$ of B1a and B1b in ^{151}Gd appear close to the $\mathcal{J}^{(2)}$ of the first excited SD band (band 2) in ^{149}Gd , suggesting that these bands have the same high-N intruder configuration ($\pi 6^2 \nu 7^2$) as ^{150}Gd.

Band 2 (B2) in ^{151}Gd

The dynamic moment of inertia $\mathcal{J}^{(2)}$ of B2 is similar to the $\mathcal{J}^{(2)}$ of the yrast SD band in ^{149}Gd (see Figure 5.5). Its $\mathcal{J}^{(2)}$ shows a smooth decrease from 80 to 70 $\hbar^2$ MeV^{-1} over the frequency range 0.35 to 0.85 MeV. This indicates that this band has the same high-N configuration as the yrast SD band ^{149}Gd ($\pi 6^2 \nu 7^1$).

Band 3a (B3a) and Band 3b (B3b)

The transition energies in band 3a appear to lie at the midpoints of transitions in band 3b, which could indicate that these bands are signature partners based on an orbital which exhibits very little signature splitting as a function of rotational frequency. Moreover, they have very similar moments of inertia. The dynamic moments of inertia $\mathcal{J}^{(2)}$ (see Figure 5.5) appear to be very similar to the $\mathcal{J}^{(2)}$ of the yrast SD band in ^{150}Gd , but the magnitude of $\mathcal{J}^{(2)}$ is slightly lower than that of the yrast

SD band in ^{150}Gd . This indicates that B3a and B3b in ^{151}Gd have the same high-N configuration as the yrast SD band in ^{150}Gd ($\pi 6^2 \nu 7^2$).

Band 4 (B4) in ^{151}Gd

The dynamic moment of inertia $\mathcal{J}^{(2)}$ of B4 in ^{151}Gd (see Figure 5.5) is also similar to the $\mathcal{J}^{(2)}$ of the yrast SD band in ^{150}Gd . Its $\mathcal{J}^{(2)}$ shows even regression from 105 to 85 $\hbar^2$ MeV^{-1} over the frequency range 0.4 to 0.75 MeV, thus establishing that this band has the same high-N configuration as the yrast SD band in ^{150}Gd ($\pi 6^2 \nu 7^2$).

5.2.2 Configurations of the Superdeformed Bands in ^{151}Gd

Structure of Band 1a (B1a) and Band 1b (B1b) in ^{151}Gd

These bands are assigned as neutron excitations and to have the same high-N configuration as the yrast SD band in ^{150}Gd . The 87th neutron occupies the high-K low-N [402]5/2 orbitals, giving a pair of signature partners (see Figure 5.5.(a)). In Figure 5.7, the alignment of band 1a and 1b in ^{151}Gd was plotted relative to the yrast SD band in ^{150}Gd. This demonstrates that the relative alignment is almost constant with rotational frequency, is almost zero at high frequency, and that $\Delta i = 1\ \hbar$ at lower frequency. This confirms that band 1a and 1b have the same high-N configuration related to that of the yrast SD band in ^{150}Gd and the former are assigned to be $\pi 6^2 \nu 7^2([402]5/2^+)^1$. The parity and signatures are $(\pi, \alpha) = (+, 1/2)$ for B1a, and $(\pi, \alpha) = (+, -1/2)$ for B1b.

Structure of Band 2 (B2) in ^{151}Gd

The $\mathcal{J}^{(2)}$ moment of inertia of B2 in ^{151}Gd (see Figure 5.5) signals that B2 has the same high-N configuration as that of the yrast SD band in ^{149}Gd, in which case the 86th and 87th neutrons (see Figure 5.6.(b)) are to occupy the [402]5/2 orbitals. The alignment of B2 (see Figure 5.7) relative to the yrast SD band in ^{149}Gd provides evidence that it is nearly constant as a function of rotational frequency. Furthermore,

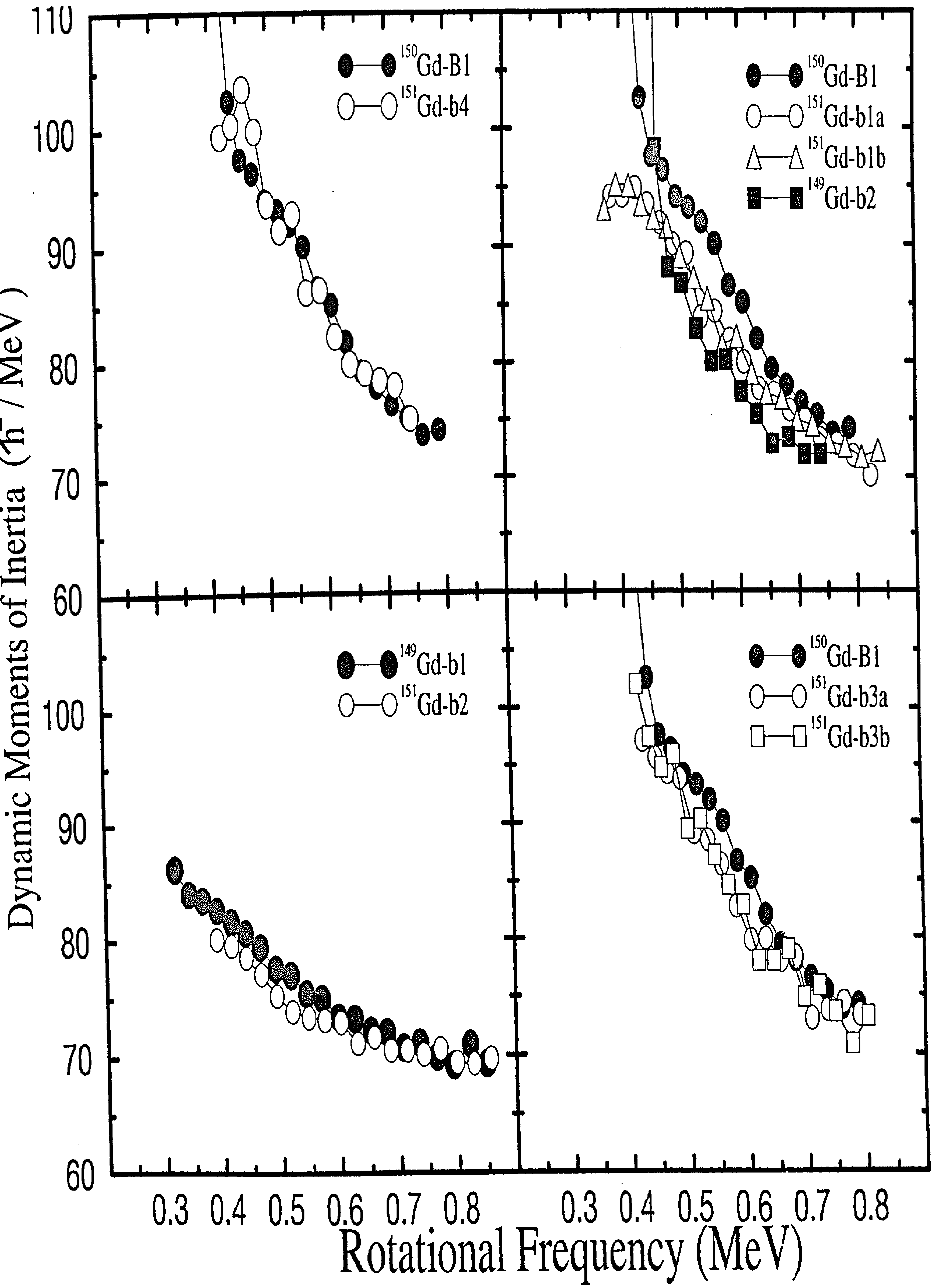

Figure 5.5: Dynamic Moments of Inertia for bands 1a, 1b, 2, 3a, 3b, 4 in ^{151}Gd compared with the yrast SD bands of neighbouring nuclei the magnitude of the alignment of B2 starts at $\Delta i = 0\ \hbar$ at low frequency but tends towards $\Delta i = -0.5\ \hbar$ at around -0.55 MeV. This provides evidence that B2 has a configuration related to that of yrast SD band of ^{149}Gd and it is assigned to be $\pi 6^2 \nu 7^1([402]5/2^+)^2$, the parity and signatures being $(\pi, \alpha) = (-, -1/2)$.

Structure of Band 3a (B3a) and Band 3b (B3b) in ^{151}Gd

These bands are assigned as neutron excitations and have the same high-N configuration as the yrast SD band in ^{150}Gd. In the single-particle Routhians diagram for neutron (see Figure 5.6.(c)), the 87^{th} neutron needs must occupy the [521]3/2 orbital, giving the signature partner for the same reason given in the structure of B1a and B1b. In Figure 5.7, the alignment of bands 3a and 3b in ^{151}Gd are plotted relative to the yrast SD band in ^{150}Gd . This establishes that the relative alignment is almost constant with rotational frequency, lies at around $\Delta i = 0.25\ \hbar$ at high frequency and has $\Delta i = 1\ \hbar$ at lower frequency. This provides evidence that bands 3a and 3b have the same high-N configuration related to that of the yrast SD band in ^{150}Gd. The parity and signatures are $(\pi, \alpha) = (-, -1/2)$ for B3a, and $(\pi, \alpha) = (-, 1/2)$ for B3b.

Structure of Band 4 (B4) in ^{151}Gd

The $\mathcal{J}^{(2)}$ moment of inertia of B4 in ^{151}Gd (see Figure 5.5) indicates that B4 has the same high-N configuration as that of the yrast SD band in ^{150}Gd, in which case the 87^{th} neutron (see Figure 5.6.(d)) occupies the [514]9/2 orbital. The alignment of B4 (see Figure 5.7) relative to the yrast SD band in ^{150}Gd shows that it is nearly constant as a function of rotational frequency. Moreover, the magnitude of the alignment of B4 is almost constant and $\Delta i = 1\ \hbar$ at all frequencies. This reveals that B4 has a configuration related to that of yrast SD band of ^{150}Gd and it is assigned to be $\pi 6^2 \nu 7^2([514]9/2^-)^1$; therefore, this band ought to have a signature partner but it has not yet been observed. The parity and signatures are $(\pi, \alpha) = (-, 1/2)$.

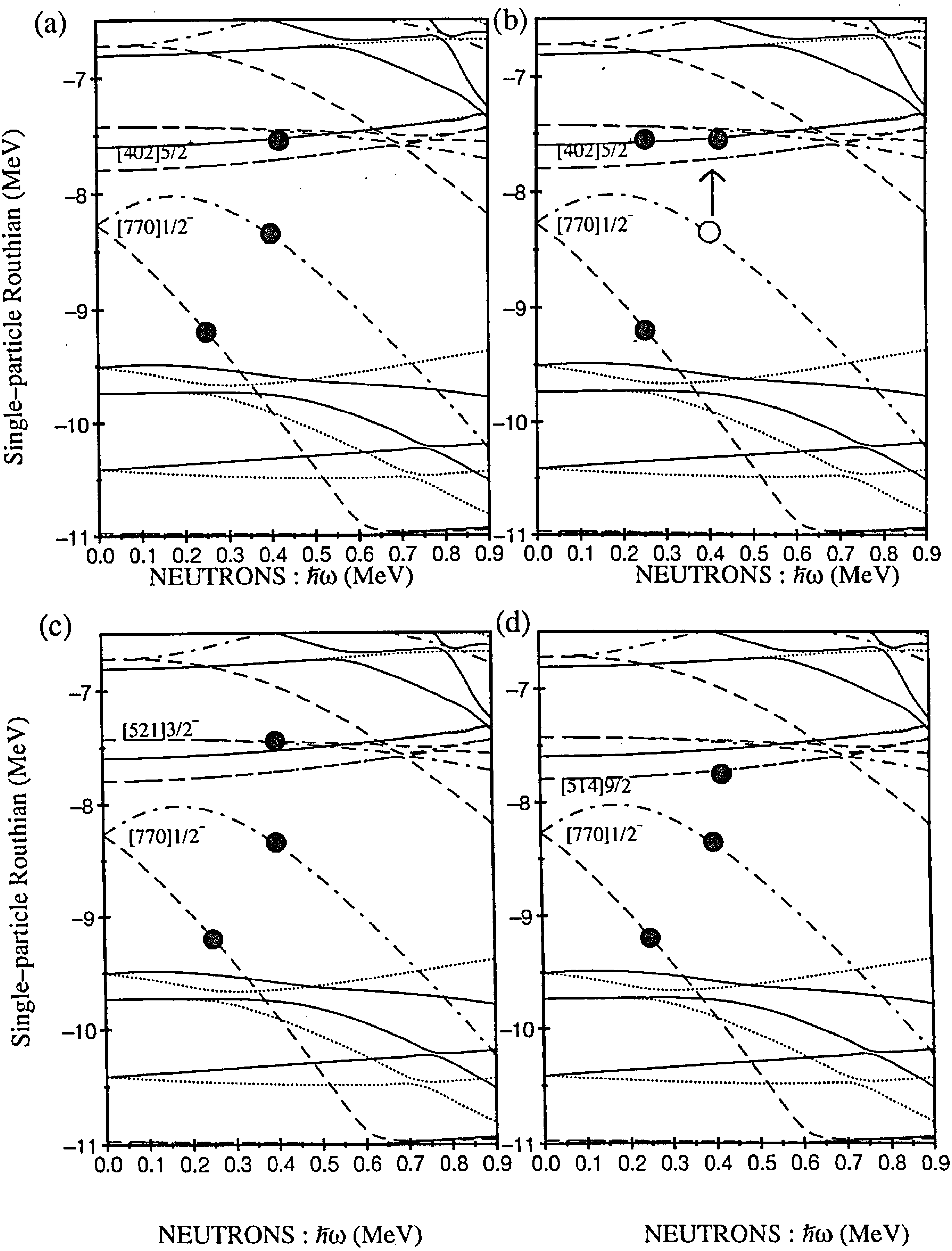

Figure 5.6: Single-particle Routhians for neutrons (a-d) calculated with the deformation parameters $\beta_2 = 0.58$, $\beta_4 = 0.1$ and $\gamma = 0$ as a function of rotational frequency for ^{150}Gd; (a) for bands 1a and 1b, (b) for band 2, (c) for bands 3a and 3b, (d) for band 4.

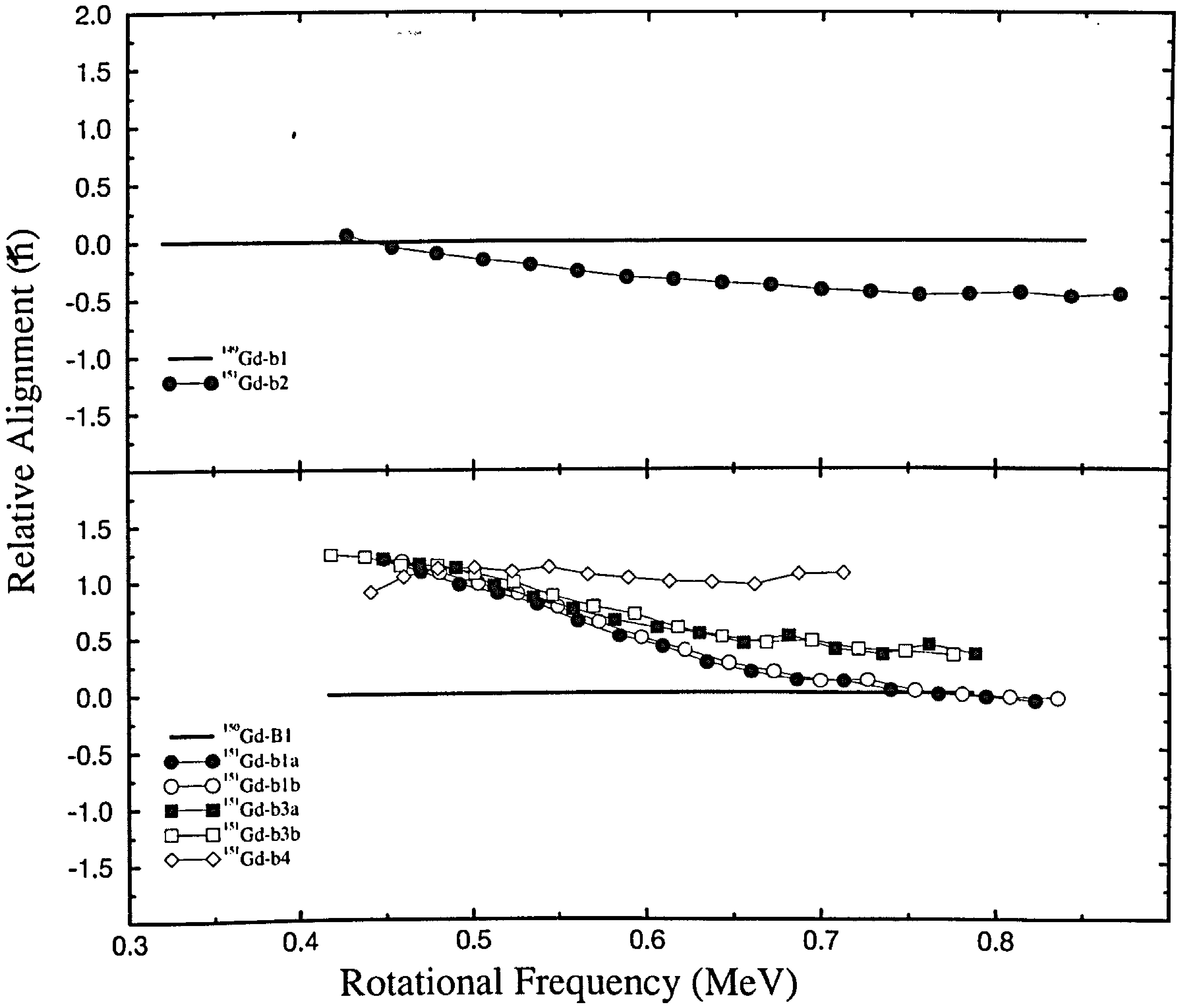

Figure 5.7: Relative alignment of B1a, B1b, B2, B3a, B3b, B4 plotted relative to the yrast SD bands of neighbouring nuclei.

The suggested proton and neutron configurations of all SD bands in ^{151}Gd are summarised in Table 5.3 with their reference for previously-known SD bands.

Bands	Configurations	(π, α)	Ref.
1a	$\pi6^2\nu7^2([402]5/2^+)^1$	$(+,\frac{1}{2})$	*
1b	$\pi6^2\nu7^2([402]5/2^+)^1$	$(+,-\frac{1}{2})$	*
2	$\pi6^2\nu7^2([770]1/2^-)^{-1}([402]5/2^+)^2$	$(-,-\frac{1}{2})$	*
3a	$\pi6^2\nu7^2([521]3/2^-)^1$	$(-,-\frac{1}{2})$	*
3b	$\pi6^2\nu7^2([521]3/2^-)^1$	$(-,\frac{1}{2})$	*
4	$\pi6^2\nu7^2([514]9/2^-)^1$	$(-,\frac{1}{2})$	*

Table 5.3: Suggested configurations of all SD bands in ^{151}Gd . " * " represents the suggested assignments from this work.

Chapter 6

General Conclusions and Future Prospects

An experiment was carried out to investigate and understand in more detail the decay mechanism of SD bands in the 150 mass region. Further aims were to search for SD linking transitions, to establish the spin and excitation energies of SD bands in ^{150}Gd and to discover further examples of excited SD structures. The present study of ^{150}Gd has led to the observation of fourteen SD structures, eight of which have been assigned to ^{150}Gd and six assigned to ^{151}Gd. Prior to this experiment, there was no evidence of SD structures in ^{151}Gd. These data show that the bands have systematic relationships with the other SD bands in the $A \approx 150$ mass region. They have been interpreted in a consistent manner within the high-N intruder scheme [Na89]. The specific orbital configurations of the SD bands have been assigned with the use of single-particle Routhian calculations. The structures of these bands have been proposed on the basis of the $\mathcal{J}^{(2)}$ moment of inertia and relative alignment measurements.

Previously-known SD bands 1, 2 and 4a in ^{150}Gd have been extended to higher rotational frequencies. Band 5 has been extended to lower and higher rotational frequencies, and also higher frequency transitions of band 5 indicate a backbend, suggesting that a neutron excitation is required for band 5. In contrast to the assignment of Clarke [Cl95], the two lowest frequency transitions in band 4b have been assigned as low-lying transitions of ^{149}Gd, and not as transitions in ^{150}Gd.

Bands 6a and 6b are signature partners and are identical to the yrast SD band in ^{149}Gd, indicating a neutron excitation. Band 7 is identical to the yrast SD band in ^{148}Gd, suggesting that band 7 is based on a neutron particle-hole excitation. Band 8a and band 8b are assigned to be a neutron and proton excitation band and band 8b also has a discontinuity, offering proof that there is another band (missing) which interacts with band 8b. Band 9 is identical to the yrast SD band in ^{152}Dy, indicating 2p-2h excitation. Bands 10a and 10b are signature partners and are identical to the yrast SD band in ^{149}Gd, indicating a neutron excitation. In addition, bands 10a and 10b show a discontinuity at lower γ-ray energies.

Details of the decay scheme around the backbend in band 2 in ^{150}Gd have been established and inter-band linking transitions have been identified. This is the very first observation of linking transitions in the mass 150 region. The spin and excitation energies of bands 1 and 2 have been established. The links have been identified as E2 and the transition probability of these linking transitions was found to be $B(E2) \approx 30$ W.u. A decay branch of band 2 has also been identified as a continuation of band 2 below the backbend.

Solid evidence for cross-talk between bands 3 and 4a has been presented in this work. Furthermore, previously-predicted [Bea93] cross-band transitions between these bands have been identified.

Six SD bands have been observed and assigned to ^{151}Gd. These are the first such observations in ^{151}Gd. As a result, bands 1a and 1b are signature partners and are identical to the yrast SD band in ^{150}Gd, demonstrating the same high-N configuration as ^{150}Gd. Band 2 in ^{151}Gd is identical to the yrast SD band in ^{149}Gd, indicating a neutron excitation and showing the same high-N configuration as ^{149}Gd. Bands 3a and 3b are signature partners and are identical to the yrast SD band in ^{150}Gd, identified as the same high-N configuration as ^{150}Gd. Band 4 is identical to the yrast SD band in ^{150}Gd, showing the same high-N configuration as the yrast SD band in ^{150}Gd.

This discovery of new SD bands in ^{150}Gd and ^{151}Gd has, naturally, left some questions unanswered and there remain some interesting problems that need to be addressed in future experiments. These include:

1. A measurement of the lifetimes of the excited states so as to confirm the properties of these new bands.
2. An investigation to search for the missing bands would provide important information for high-N orbitals, in the mass 150 region.
3. Further studies are required into the observed discontinuity in band 5 and in bands 10a and 10b at high and low frequencies respectively.

References

[Af96] A.V. Afanasjev et al., Nucl. Phys. **A606** 107 (1996).

[Al92] I. Ali, Ph.D Thesis, University of Liverpool, (1992).

[An76] G. Anderson et al., Nucl. Phys. **A268** 205 (1976).

[Ap97] D.E. Appelbe et al., Phys. Rev. **C56**, 2490 (1997).

[At93] A. Atac et al., Phys. Rev. Lett. **70**, 1069 (1993).

[Az95] F. Azaiez et al., Phys. Scr. **T56** 35 (1995).

[Ba92] A.M. Baxter et al., Nucl. Instrum. Meth **A317** 101 (1992).

[Bak95] C. Baktash, Ann. Rev. Nucl. Part. Sci. **45**, 485 (1995).

[Baz94] D. Bazzacco et al., Phys. Rev. **C49**, R2281 (1994).

[Bea93] C.W. Beausang et al., Phys. Rev. Lett. **71**, 1800 (1993).

[Bea98] C.W. Beausang et al., Phys. Lett. **B417**, 13 (1998).

[BCS57] J. Bardeen, L.N. Cooper and J.N. Schrieffer, Phys. Rev. **108** 1175 (1957).

[Be75] T. Bengtsson et al., Phys. Lett. **B57** 301 (1975).

[Be88] T. Bengtsson et al., Phys. Lett. **B208** 39 (1988).

[Be81] R. Bengtsson et al., Phys. Scr. **24** 200 (1981).

[Ben87] M.A. Bentley et al., Phys. Rev. Lett. **59**, 2141 (1987).

[Ber95] L.A. Bernstein et al., Phys. Rev. **C52**, R1171 (1995).

[BS96] C.W. Beausang and J. Simpson, J. Phys. **G 22** 527 (1996).

[BMP58] A. Bohr, B.R. Mottelson and D. Pines, Phys. Rev, **110** 936 (1958).

[BM75] A. Bohr and B.R. Mottelson, *Nuclear Sttructure II* Benjamin (1975).

[Bo36] N. Bohr, Nature **344** 137 (1936).

[By90] T. Byrski et al., Phys. Rev. Lett. **64**, 1650 (1990).

[Cl95] S. Clarke, Ph.D Thesis, University of Liverpool, (1995).

[Ch73] P.R. Christensen et al., Nucl. Phys. **A207** 33 (1973).

[De64] S. DeBenedetti, *Nuclear Interactions*, Wiley (1964).

[Del95] M.A. Deleplanque et al., Phys. Rev. **C52**, R2302 (1995).

[DN85] J. Dudek and W. Nazarewicz, Phys. Rev. **C31** 298 (1985).

[Dr90] M.W. Drigert et al., Nucl. Phys. **A515** 466 (1990).

[DW78] J. Dudek and T. Werner, J. Phys. **G4** 1543 (1978).

[Eh59] H.F. Ehrenberg et al., Phys. Rev. **113**, 666 (1959).

[Fa89] P. Fallon et al., Phys. Lett. **B218**, 137 (1989).

[Fa89a] P. Fallon, Ph.D Thesis, University of Liverpool, (1989).

[Fa91] P. Fallon et al., Phys. Lett. **B257**, 269 (1991).

[Fa94] P. Fallon et al., Phys. Rev. Lett. **73**, 782 (1994).

[Fi98] Ch. Finck et al., Private Communication. (1998).

[Fl93] S. Flibotte et al., Phys. Rev. Lett. **71**, 688 (1993).

[Gr73] E. Grosse et al., Phys. Rev. **31**, 840 (1973).

[Ha88] B. Haas et al., Phys. Rev. Lett. **60**, 503 (1988).

[Ha90] B. Haas et al., Phys. Rev. **C42**, R1817 (1990).

[He94] K. Heyde, *Basic Ideas and Concepts in Nuclear Physics*, Bookcraft (1994).

[HJS49] O. Haxel, D. Jensen, H.E. Suess, Phys. Rev. **75** 1766 (1949).

[HW53] D.L. Hill and J.A. Wheeler. Phys. Rev. **89**, 1102 (1953).

[In54] D.R. Inglis, Phys. Rev. **96**, 1059 (1954).

[Je90] N.A. Jelley, *Fundementals of Nuclear Physics*, Cambridge University Press (1990).

[JK91] R.V.F. Janssens and T.L. Khoo, Annu. Rev. Nucl. Part. Sci. **41** 321 (1991).

[Jo71] A. Johnson et al., Phys. Lett. **B**, 605 (1971).

[Joh89] J.K. Johnsson, Phys. Rev. Lett. **63**, 2200 (1989).

[Jos98] D.T. Joss, Ph.D Thesis, University of Liverpool, (1998).

[Kh96] Khoo et al., Phys. Rev. Lett. **76**, 1583 (1996).

[Kn89] G.F. Knoll, *Radiation Detection and Meassurement*, Second Edition, Wiley (1989).

[Kr88] K.S. Krane, *Introductory Nuclear Physics*, Second Edition, Wiley (1988).

[Le77] I.Y. Lee, Phys. Rev. Lett. **38**, 1454 (1977).

[Lee90] I.Y. Lee, Nucl. Phys. **A520**, p641c (1990).

[Lu95] S. Lunardi et al., Phys. Rev. **C52**, R6 (1995).

[Ma49] M.G. Mayer, Phys.-Rev. **75** 1969 (1949).

[Mac94] A.O. Macchiavelli et al., Proc. Conf. on Phys. from Large γ-ray Detector Arrays. p149 (Berkeley, 1994).

[Mac97] A.O. Macchiavelli, Invited Talk, Exotic Nuclear Shapes Symposium, (Debrecen 1997).

[MV60] B.R. Mottelson and J.G. Valatin, Phys. Rev. Lett. **5** 511 (1960).

[Na89] W. Nazarewicz et al., Nucl. Phys. **A503**, 3127 (1989).

[Nak98] T. Nakatsukasa et al., private communication, (1989).

[No85] P.J. Nolan et al., J. Phys. G. **11**, L17 (1985).

[No93] P.J. Nolan et al., Nucl. Phys. **A533**, 107c (1993).

[No94] P.J. Nolan et al., Ann. Rev. Nucl. Part. Sci. **45**, p561 (1994).

[Ni55] S.G. Nilsson, Mat. Fys. Medd. Dan. Vid. Selsk. **29** 68 (1955).

[Ny84] B.M. Nyako, Phys. Lett. **52** 507 (1984).

[Pe96] C.M. Petrache et al., Phys. Rev. Lett. **77**, 239 (1996).

[Po62] S.M. Polikanov et al., Sov. Phys. JETP**15** 1016 (1962).

[Ra80] I. Ragnarsson et al., Nucl. Phys. **A347** 287 (1980).

[Ra93] I. Ragnarsson, Nucl. Phys. **A557** 167c (1993).

[Rad95] D.C. Radford, Nucl. Instr. Meth. **A361** 297 (1995).

[Sa96] W. Satula et al., Phys. Rev. Lett. **77**, 5182 (1996).

[Si96] B. Singh et al., Table of SD Nuclear Bands in Fission Isomers. Nucl. Inst. Meth. **78**, 1 (1996).

[Sm95] A.G. Smith, Phys. Lett. **B355** 187 (1995).

[Ste75] F.S. Stephens, Rev. Mod. Phys. **47** 43 (1975).

[Ste90] F.S. Stephens, Nucl. Phys. **A520** 91c (1900).

[St66] V.M. Strutinsky, Sov. J. Nucl. Phys. **3** 449 (1966).

[St67] V.M. Strutinsky, Nucl. Phys. **A95** 420 (1967).

[Sz83] Z. Szymański, *Fast Nuclear Rotation*, Clarendon Press, Oxford (1983).

[Th73] P. Thieberger, Phys. Lett. **45B**, 417 (1973).

[Tu79] R.M. Turnbull, *The Structure of Matter*, First Edition, Thomson Litho Ltd. (1979).

[Tw86] P.J. Twin et al., Phys. Rev. Lett. **57**, 811 (1986).

[Tw90] P.J. Twin et al., Nucl. Phys. **A520**, 17c (1990).

[Tw94] P.J. Twin, Nucl. Phys. **A574**, 51c (1994).

[Tw95] P.J. Twin, Nucl. Phys. **A583**, 199c (1995).

[Tw96] P.J. Twin et al., in: Proceedings of the Conference on Nuclear Structure at the Limits, Argonne National Laboratory, July 22-26, (1996)

[Ur92] W. Urban, Program : Scana, University of Manchester, (1992).

[We35] C. F Weizacker et al., Zeitschrift fur Physik **A96** (1935) 431.

[WS54] R. D Woods and D. Saxon, Phys. Rev. **95** (1954) 577, 40.

[VH73] R. Vandenbosh and J.R. Huizenga, *Nuclear Fission*, Academic Press (1973).